UNIVERSITY OF SAO PAULO

GEOSCIENCES INSTITUTE

Ar bulk diffusivity experiments in microgabbros with implications for the Venusian geodynamics

PEDRO DE ALMEIDA SEMEDO

Master Dissertation submitted to the Geosciences Institute of the University of Sao Paulo to obtain a Master of Science degree. Concentration Area: Mineralogy and Petrology

Advisor: Prof. Dr. Silvio Roberto Farias Vlach

SAO PAULO

2022

Autorizo a reprodução e divulgação total ou parcial deste trabalho, por qualquer meio convencional ou eletrônico, para fins de estudo e pesquisa, desde que citada a fonte.

UNIVERSIDADE DE SÃO PAULO
INSTITUTO DE GEOCIÊNCIAS

AR BULK DIFFUSIVITY EXPERIMENTS IN MICROGABBROS WITH IMPLICATIONS FOR THE VENUSIAN GEODYNAMICS

PEDRO DE ALMEIDA SEMÊDO

Orientador: Prof. Dr. Silvio Roberto Farias Vlach

Dissertação de Mestrado

Nº 884

COMISSÃO JULGADORA

Dr. Silvio Roberto Farias Vlach

Dr. Diego González-García

Drª. Celia Dalou

SÃO PAULO
2022

To Cleomar (*in memoriam*)

ACKNOWLEDGEMENTS

"The greatest teacher, failure is".

Master Yoda

RESUMO

O sistema geoquímico do argônio é uma importante ferramenta para as ciências planetárias. O ^{40}Ar é radiogênico e produzido através do decaimento radioativo de ^{40}K (meia-vida ~ 1.25 Ga) em minerais na crosta e manto de planetas rochosos, enquanto os isótopos ^{36}Ar e ^{38}Ar são primordiais. As atmosferas da Terra e de Vênus possuem razões ^{36}Ar/^{38}Ar semelhantes (5.3 e 5.5, respectivamente) mas contrastantes razões ^{40}Ar/^{36}Ar (~ 300 *vs*. 1, respectivamente), indicando que a Terra é mais eficiente na degaseificação de ^{40}Ar. Como vulcanismo é um importante mecanismo de degaseifação de ^{40}Ar, esses dados sugerem uma maior atividade vulcânica na Terra em relação a Vênus durante a evolução destes planetas. Entretanto, difusão é um outro possível transportador de ^{40}Ar de geosferas para atmosferas e a temperatura superficial média em Vênus (460 ºC) é maior que a temperatura de fechamento do gás na maioria dos sistemas silicáticos. Como não há dados acerca da difusão de Ar em rochas basálticas, neste trabalho foram feitos experimentos de difusão efetiva utilizando microgabros sintéticos (similares a "basaltos" venusianos) a 460 ºC (1 atm) para investigar a eficiência da difusão em mobilizar Ar na crosta de Vênus. Foi utilizada uma fornalha vertical tubular (VTF) para fundir e cristalizar o pó de um basalto toleiítico em condições de saturação de Ar, gerando um total de 10 "pérolas" de microgabro saturadas em Ar. Oito dessas pérolas foram reintroduzidas na VTF (composição atmosférica controloada de 100% CO_2) e em uma mufla (MF, composição do ar) simultaneamente (4 em cada forno) a 460 ºC. As duas fornalhas foram utilizadas para checar se a composição atmosférica afetaria os resultados. Alíquotas foram então removidas depois de 2, 4, 8 e 16 dias. Coeficientes de difusão efetiva (D_{bulk}) foram obtidos através da análise da variação de concentração de Ar nas pérolas após os experimentos. Experimentos realizados na VTF e MF tiveram resultados semelhantes. Duas soluções da equação de difusão foram utilizadas, com os melhores resultados indicando D_{bulk} de 3.5 x 10^{-13} m²/s. Os resultados indicam que difusão é um processo muito lento nas condições analisadas e que menos de 1% do Ar total teria sido removido da crosta venusiana se difusão fosse o único mecanismo de degaseificação. Portanto, os dados suportam a ideia de que vulcanismo é a principal fonte de ^{40}Ar para a atmosfera em planetas com crostas anidras e que, de fato, deve ter havido maior atividade vulcânica na Terra que em Vênus durante as evoluções dos planetas. Finalmente, eu sugiro que a crosta de Vênus possui excesso de ^{40}Ar e que a razão ^{40}Ar/^{36}Ar na atmosfera venusiana deve se tornar mais semelhante com a da Terra após o próximo evento global de produção crustal, quando magma estaria em contato direto com a atmosfera, favorecendo a degaseificação de ^{40}Ar.

Palavras-chave: Petrologia experimental, geoquímica experimental, difusão, geodinâmica, Vênus.

ABSTRACT

The argon geochemical system is an important tool for the planetary sciences. ^{40}Ar is radiogenic and produced by the radioactive decay of ^{40}K (half-life ~ 1.25 Ga) in minerals in the crust and mantle of rocky planets, while ^{36}Ar and ^{38}Ar are primordial. The atmospheres of Earth and Venus share similar ^{36}Ar/^{38}Ar ratios (5.3 and 5.5, respectively) but contrasting ^{40}Ar/^{36}Ar ratios (~300 *vs.* 1, respectively), indicating that Earth is more effective in degassing ^{40}Ar. Because volcanism is a major ^{40}Ar degassing agent, these data suggest higher volcanic activity through Earth's evolution relative to Venus'. However, diffusion is another possible ^{40}Ar transporter from geospheres to atmospheres and the average surface temperature on Venus (460 ºC) is above the closure temperature of the gas in most silicate systems. Because there is no data concerning the diffusion of Ar in basaltic rocks, here, bulk diffusion experiments were made using synthetic microgabbros (similar to Venusian 'basalts') under 460 ºC (1 atm) to investigate the effectiveness of diffusion in mobilizing Ar in the crust of Venus. A vertical tubular furnace (VTF) was used to melt and crystallize a tholeiitic basalt powder under Ar saturation conditions to dope the aliquots with the gas, generating a total of ten Ar-saturated microgabbro beads. Eight of these beads were reintroduced into the VTF (100% CO_2 atmosphere) and muffle furnace (MF, air composition) simultaneously (4 in each furnace) at 460ºC. The two furnace apparatuses were used to check if the atmospheric composition would alter the results. Aliquots were then removed after 2, 4, 8, and 16 days. Bulk diffusion coefficients (D_{bulk}) were obtained by analyzing the variation of Ar concentration in the beads after the experiments. Experiments held in the VTF and MF had similar results. Two different solutions for the diffusion equation were used, with the best results showing D_{bulk} values of ~ 3.5 x 10^{-13} m²/s. The results indicate that diffusion is very slow in the analyzed conditions and that less than 1 % of the total Ar would have been removed from the Venusian crust if diffusion was the only degassing agent. Thus, the data support the idea that volcanism is the main source ^{40}Ar to the atmosphere in anhydrous crusts and that, indeed, Earth must have had higher volcanic activity in its history in comparison to Venus. Finally, I suggest that the crust of Venus has an excess of ^{40}Ar and that the planet's atmospheric ^{40}Ar/^{36}Ar ratio should become more similar to Earth's after the next global resurfacing event, when magma should be in direct contact with the atmosphere, favoring the degassing of ^{40}Ar.

Keywords: Experimental petrology, experimental geochemistry, diffusion, geodynamics, Venus.

SUMMARY

LIST OF FIGURES

LISTA DE SIGLAS

BDT	Brittle-ductile transition zone
BSE	Backscattered electrons
CMB	Core-mantle boundary
CPX	Clinopyroxene
DHS	Diffusion from a homogeneous sphere into an infinite reservoir
EMP	Electron microprobe
HSD	Half-space diffusion problem
IGC	Institute of Geosciences
IP	Ionic porosity
MF	Muffle furnace
MORB	Mid ocean ridge basalt
MPR	Mean planetary radius
NBO	Non-bridging oxygen
OPX	Orthopyroxene
USP	University of São Paulo
VTF	Vertical tubular furnace
WDS	Wavelength-dispersive x-ray spectroscopy

CHAPTER I – INTRODUCTION

Venus is one of the four terrestrial planets in the solar system (besides Mercury, Earth, and Mars) and is the second closest to the Sun. Being one of the brightest lights in both night and early day sky, Venus has been observed by humans and incorporated into their cultures since pre-telescopic times in mythology and astrology. The planet's brightness is related to its thick and dense atmosphere, which was identified in the 1700s by Lomonosov (soviet scientist) and interpreted as being composed of vapor water (Basilevsky and Head, 2003). This interpretation, together with measurements of Venusian diameter, suggested that the planet was Earth's twin.

There are many similarities between Earth and Venus. According to Basilevsky and Head (2003), the Venusian radius is 6,051.8 Km (95% of Earth's), mass is 4.87×10^{24} kg (81.4% of Earth's), bulk density is 5.24 g/cm^3 (95% of Earth's), and surface gravity is 8.87 m/s^2 (90.7% of Earth's). These data, together with surficial K/U ratios and major elements abundances suggest that both planets have similar bulk compositions. Also, Venus orbits the Sun at a mean distance of 108×10^6 km, 72% of the Earth-Sun distance. The closer distance to the Sun causes Venus to receive almost two times more solar energy than Earth does. However, part of this energy is reflected due to Venusian high albedo caused by its bright clouds, making both planets relatively similar when it comes to solar energy input.

With the advance of science and the increasing knowledge on Venusian geological processes, it became clear that the planet is not Earth's twin – at least not an identical one. Several striking differences make them two worlds apart. For example: (1) Earth has an excess in surface water of about 1.2×10^{21} Kg when compared to Venus (Donahue, 1999; Lécuyer et al., 2000); (2) It is believed that Venus is in a stagnant lid regime, with a sole tectonic plate, whereas Earth is in an active tectonic regime with multiple tectonic plates (Wilson, 2009; Ghail, 2015); (3) Venusian atmosphere is CO_2 dominated (~90%) and exerts a surface pressure of ~9 MPa, while the terrestrial atmosphere is N_2 dominated (~78%) with a surface pressure of ~0.1 MPa; (4) the intense greenhouse effect on Venus makes it the planet with the hottest surface in the solar system (average of 460ºC on Venus *vs* 4ºC on Earth).

Another difference, central to this work, is the atmospheric Ar geochemistry of both planets. Data from the Pioneer and Venera missions obtained in the late 70s/early 80s show that Earth has a significant higher relative concentration of radiogenic Ar (^{40}Ar) in comparison to

Venus (Hoffman et al., 1980; Istomin et al., 1980). This discrepancy may be connected to the different geodynamic styles of both planets because ^{40}Ar is transferred to the atmosphere mainly through volcanic and diffusive processes.

Here, we investigate the bulk diffusivity of Ar in tholeiitic rocks (similar to Venusian crust) under Venusian surface conditions. To do so, we determine the bulk diffusion coefficient (D_{bulk}) of Ar through sorption/desorption experiments in microgabbros using a Vertical Tubular Furnace (VTF) and a Muffle Furnace (MF).

I.1 Justification

Atmospheres are primarily formed during planetary accretion and are later fuelled by the degassing of volatiles from planets' interiors. Thus, the chemistry of atmospheres holds important information about the formation, structure and evolution of planets, including geodynamic processes (e.g. Namiki and Solomon, 1998; Kaula, 1999; Zahnle et al., 2010; Chassefière et al., 2012). Noble gases have two particularities that make them ideal tracers to these phenomena. First, they are chemically inert, *i.e.* they do not create chemical bonds with other molecules in natural conditions, and thus, once degassed, they are not transported back into the surface via weathering or deposition. Second, they are scarce in a planetary sense because during the accretion of terrestrial planets most of the volatile elements are lost to space, especially the inert ones (Ozima and Podosek, 2009). This scarceness allows the identification of the volatile sources, which would go unnoticed with other abundant elements (Namiki and Solomon, 1998; Chassefière et al., 2012).

The atmospheric make-up of Earth and Venus are key factors for why one is the crucible of life, and the other is a hellish wasteland. As more Earth-sized exoplanets are discovered, studying the processes that led to these two contrasting scenarios is crucial in our understanding of planetary/atmospheric evolution in rocky planets; in the search for life in the universe; and, more broadly, in our understanding of the cosmos.

Here we focus on the differences in Ar geochemistry on the atmospheres of Earth and Venus (see Figure 1). Ar has three stable isotopes: ^{36}Ar, ^{38}Ar, and ^{40}Ar. The lighter isotopes are primordial, while ^{40}Ar is radiogenic and produced in K-bearing minerals through the decay of ^{40}K by electron capture and positron emission (half-life ~ 1.25 Ga; e.g. Faure, 1986). Since ^{40}Ar and ^{40}K are highly incompatible, they quickly incorporate ascending liquids in the crust or mantle

(e.g. Brooker et al., 2003). When these fluids reach the surface, ^{40}K remains stored in the crust (producing more ^{40}Ar), and part of the ^{40}Ar is degassed to the atmosphere via diffusion or volcanism (e.g. Namiki and Solomon, 1998; Kaula, 1999; Pujol et al., 2013)). Once in the atmosphere, the leading process that fractionate stable isotopes is hydrodynamic escape (driven by low-temperature atmospheric loss), which preferentially removes the lighter over the heavier isotopes. Thus, as a planet evolves, it is expected that the atmospheric $^{40}Ar/^{36}Ar$ ratio increase because the lighter isotopes are lost to space and ^{40}Ar is added to the atmosphere through the degassing of mantelic and crustal material.

Mars' smaller mass and size enhance Ar fractionation due to the hydrodynamic escape of ^{36}Ar to outer space, which explains the high $^{40}Ar/^{36}Ar$ and low $^{36}Ar/^{38}Ar$ ratios for the planet in comparison with the other two (e.g. Jakosky et al., 2017; see Figure 1). The ratios of the primordial isotopes $^{36}Ar/^{38}Ar$ for Venus and Earth are very similar, indicating a common source of volatile elements (Istomin et al., 1980). However, the $^{40}Ar/^{36}Ar$ ratios are 1.03 ± 0.04 and 298.56, respectively for Venus and Earth (Istomin et al., 1980; Hoffman et al., 1980). Because volcanism is a major ^{40}Ar transporter from the geosphere to the atmosphere, these differences are likely attributed to the volcanic history of these two planets (Namiki and Solomon, 1998; Mather, 2008; Cassata et al., 2011).

However, diffusion is another important transport mechanism for ^{40}Ar through silicate rocks, and the entire Venusian crust resides above the closure temperature for Ar in most silicate systems (Kelley and Wartho, 2000). There are theoretical models that argue for limited diffusion through dehydrated basalt (Venusian crust), which implies that all atmospheric ^{40}Ar is volcanic in origin and that Venus is less degassed in comparison to Earth (e.g. Mikhail and Heap, 2017). The lack of experimental support for these theories makes them questionable.

The justification of this work is to fill in this gap and better constrain Ar diffusion in basaltic rocks, aiding in the interpretation of atmospheric Ar in rocky planets using Venus as a case study.
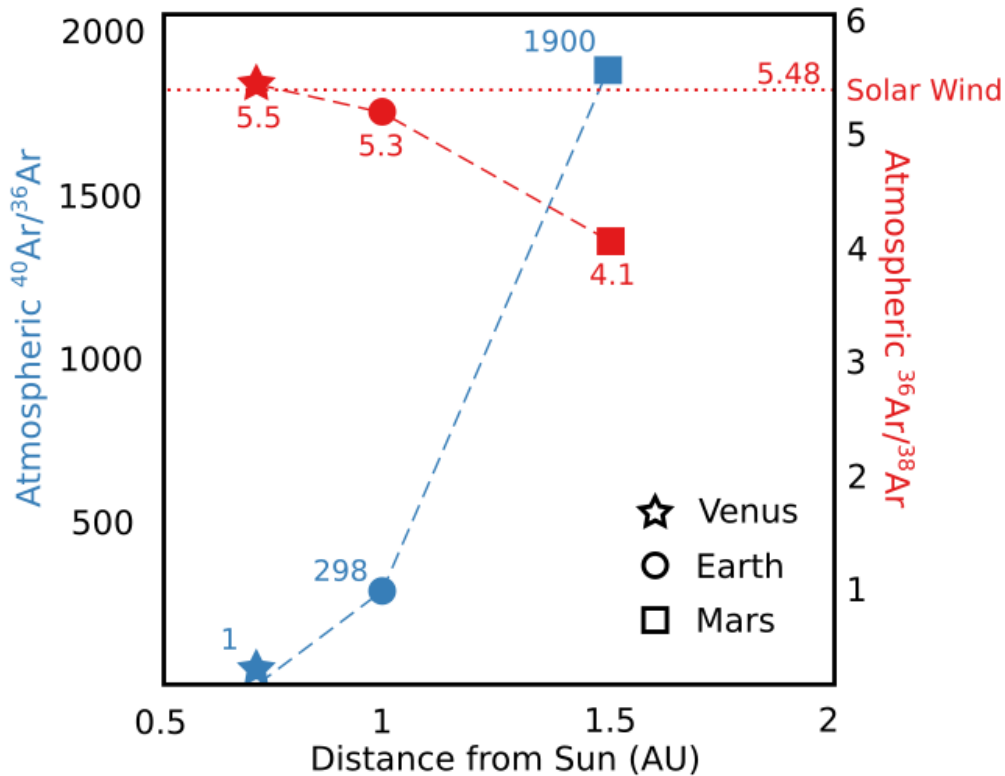
Figure 1 – Relative abundance of atmospheric Ar isotopes on the atmospheres of Mars, Venus, and Earth modified from Mikhail and Heap (2017), see references therein for sources. AU = Astronomical units. Blue (values on the left side) represents the ^{40}Ar/^{36}Ar data. Red (values on the right side) represents the ^{36}Ar/^{38}Ar data.

I.2 Objectives

The primary objective of this work is to empirically determine the bulk diffusion coefficient of Ar in a microgabbro at 460 °C (mean surface temperature of Venus) through sorption/desorption experiments using a GERO vertical tubular furnace (VTF) and a muffle furnace (MF) at the Institute of Geosciences – University of Sao Paulo. By doing so, we can calculate the characteristic diffusion distance of Ar in these conditions and investigate the relative lack of ^{40}Ar in the atmosphere of Venus.

In these experiments we can also explore the resulting differences in diffusion coefficients from running experiments at local atmospheric composition (MF) or 100% CO_2 atmosphere (VTF); the differences in Ar diffusion (and solubility) in a basaltic melt *vs.* microgabbro; and Ar bubble nucleation and growth in the aliquots (glass and microgabbro).

CHAPTER II – LITERATURE REVIEW

This chapter presents a literature review of the main topics of this dissertation, covering general geological aspects of Venus and diffusion.

II.1 Venusian Internal and Atmospheric Structure

Venus' similarities with Earth in terms of density, size, and locality in the Solar System indicate the planets share similar chemical content, with a silicate crust, a magnesium silicate mantle, and an iron-rich core. Zharkov (1992) proposed a model for the Venusian interior structure by resizing Earth's internal structure in accordance with Venus' mass. The author proposed a crust depth of 70 km and the mantle-core boundary at 2840 km (about half the planet's diameter).

Our knowledge of Earth's interior is based mainly on seismological measurements (Mocquet et al., 2011). In Venus, this kind of observation is complicated by the planet's dense and hot atmosphere, which quickly makes present-day seismometers inoperative. Humans have never obtained seismological measurements from Venus, even though the Venera-D mission intends to do so by the end of this decade. Hence, the planet's interior is inferred by theoretical models which encompass internal structure, densities, and temperatures. Aitta (2012) shows that Venus is likely to have a colder, less dense interior (Figure 2) with a central pressure of 274.47 GPa, 25% less than Earth's 363.85 GPa. These differences are mainly related to the planets' contrasted radius and mass.
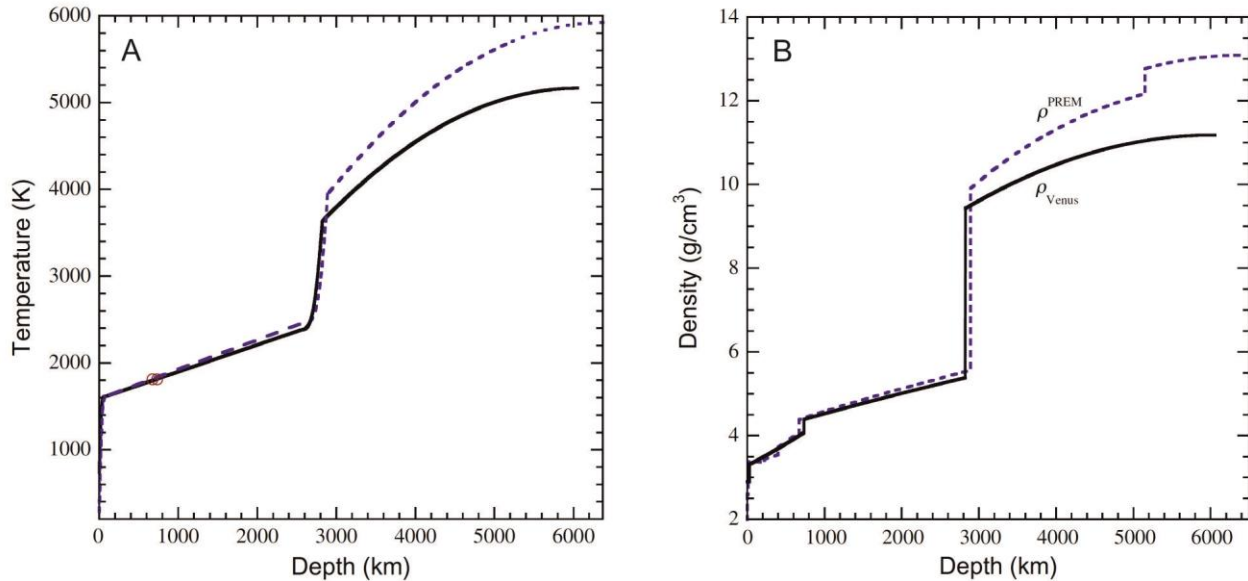
Figure 2 – Theoretical variations of temperature *vs*. depth (A) density *vs*. depth (B) for Earth (blue dashed lines) and Venus (bold solid lines) from Aitta (2012).

II.1.1 Core

The true nature of the Venusian core is very important to constrain the planet's most inner heat budget, influencing the whole planet's geodynamics. The existence of an iron-rich core is well accepted, deduced from the planet's tidal response. However, core size, temperature, and phase are unknown and commonly related to Earth's structure scaled to Venus' mass and radius (Mocquet et al., 2011; Aitta, 2012).

According to Aitta (2012), Venus' core is too hot for Fe to solidify under estimated pressures, being therefore in a liquid state, in agreement with prevailing ideas on the core state. Furthermore, the temperature at the center of Venus would be 5160 K, 220 K higher than the temperature needed to solidify an inner core. The author concludes that the Venusian core would be composed of an iron-rich fluid with $MgO + MgSiO_3$ impurities.

However Dumoulin et al. (2017) performed a computation of tidal viscoelastic deformation of Venus using six different formation scenarios for the planet. Using data from the Magellan mission (Love number, k_2), the authors conclude that a solid inner core could not be ruled out, even though a liquid core is more probable.

Another matter concerning the Venusian core is the lack of an intrinsic magnetic field. Earth's is believed to be generated due to the crystallization in the transition between the

inner/outer (solid/liquid) cores, which enhances chemically driven convection (Stevenson, 1983, 2003). Therefore, the absence of an intrinsic magnetic field on Venus indicates that the core is entirely liquid or solid, and not sufficiently cooling to sustain a chemically driven dynamo (Stevenson, 2003).

II.1.2 Mantle

Zharkov (1992) correlates Venusian mantellic structure with the Earth's, suggesting that the mantle-crust boundary would reside at a 70 km depth, whereas the mantle-core boundary would be at the depth of 2840 Km. The author divides the planet's mantle into four mineral zones based on pressure and temperature-dependent phase transformations. From 70 to 480 km depth, the major mineral would be olivine. From 480 to 760 km depth, major minerals would have a spinel-like structure. From 760 to 1,000 km, mantle material would be structured in a similar way to ilmenite and perovskite. In the lower mantle (1000 to 2840 km depth) the perovskite-like phase dominates.

With numerical calculations (triclinical phenomena, see article and references therein for details), Aitta (2012) estimates a core-mantle boundary (CMB) radius of 3228 km. Considering a planet's mean radius of 6052 km, the CMB would be at a 2824 km depth, similar to the values inferred by Zharkov (1992). The author suggests a CMB pressure of 114 GPa (in comparison to Earth's 136 GPa). This pressure difference indicates that the perovskite to the post-perovskite phase transition that takes place near Earth's CMB might not happen on Venus' mantle due to the lower pressure. The lower mantle would start at a depth of 732 km with a 23.8 GPa pressure, again similar to the value proposed by Zharkov (1992).

Importantly, the Venusian temperature at CMB is estimated to be ~3,630 K in contrast with surface ~740 K. This difference implies a temperature gradient between surface and CMB of 1.02 ºC/km, in comparison with Earth's 1.26ºC/km. This difference causes discrepancies in mantle convection and dynamics, with consequent disparities in surficial features between both planets, which is discussed in section II.2.

II.1.3 Crust

Images provided by the Magellan mission and altimetry data show that about 80% of the Venusian surface is dominated by volcanic plains which lie close to the mean planetary radius

(MPR = 6051.5 km above the planet's center of mass; Basilevsky and Head, 2003). There is a broad variety of volcanic landforms on Venus, ranging from kilometric volcanic constructs to hundreds of kilometers of homogeneous volcanic plains (Ivanov and Head, 2013).

Among the plains there are low ridges extending for thousands of kilometers which suggest folding and shortening (Figure 3a); highland 'islands' and 'continents' of highly deformed terrains (tesserae; Figure 3b); isolated gently sloping shield volcanoes (Figure 3c); hundreds of concentric ringed features (coronae) some of which exceed a thousand kilometers in diameter, possibly associated with rift valleys (Figure 3d); and many other structures which have been detailed by (Ivanov and Head, 2013).
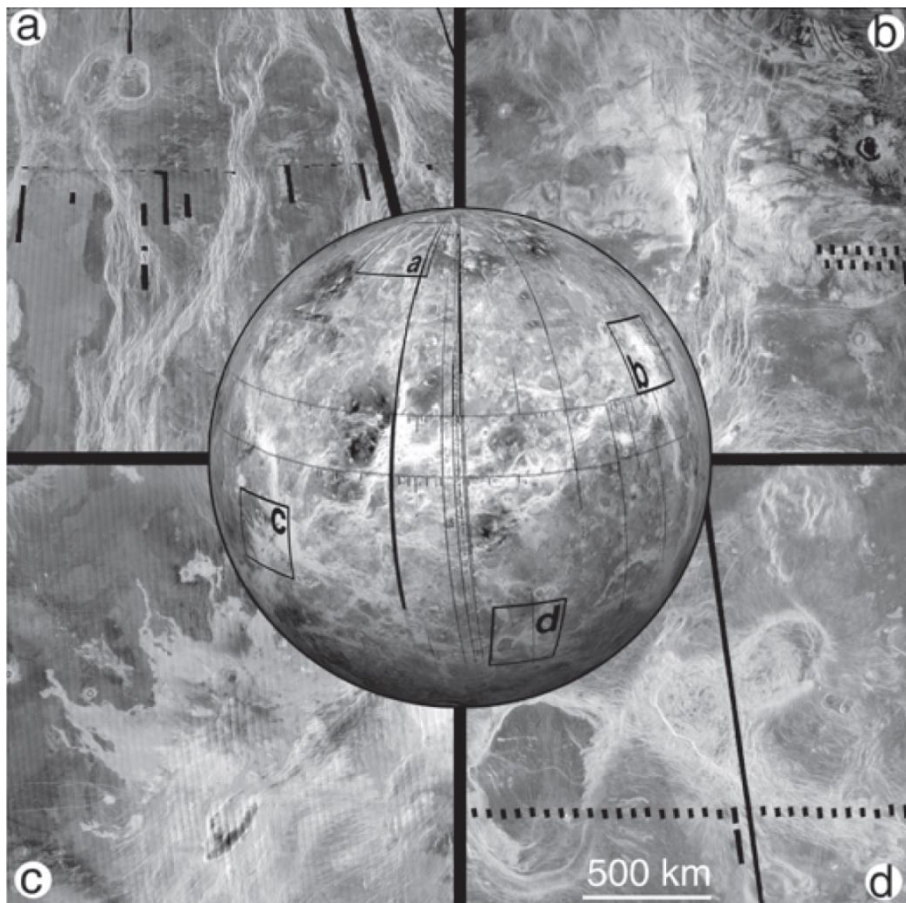
Figure 3 – Examples of main terrain types of Venus from Magellan mission images. a- belts of low ridges (bright) and neighboring regional plains (dark); b- tesserae terrain (brighter) of Beta Regio cut by a rift zone; c- Maat Mons volcano and its lava flows superposed by regional plains; d- coronae of the Parga Chasmata rift zone. Extracted from Basilevsky and Head (2003).

Due to uncertainties in thermal gradients and crustal layering, it is hard to determine the crustal thickness on Venus (Smrekar et al., 2018). In recent studies, James et al. (2013) estimate values from 8 to 45 km. Jiménez-Díaz et al. (2015) suggest the crustal thickness to be 20-25 km, exclusive of highlands. Anderson and Smrekar (2006) reported a wide range of values (up to 100 km), with most values above 50 km.

The planetary surface composition can be acquired via remote sensing, *in-situ* measurements, or by the analysis of returned samples (Gilmore et al., 2017). The thick and hot CO_2-dominated atmosphere is an expressive obstacle to obtaining data through any of these methods, so that gathering such data is a very challenging task. The only *in-situ* geochemical data from Venus are those shown in Table 1. The major element composition of surface rocks was obtained by gamma-ray and X-ray fluorescence spectrometry, indicating tholeiitic basaltic compositions similar to those found in mid-ocean ridge basalts (MORB) on Earth (Bougher et al., 1997). Additionally, Fe/Mg, Mg/Mn, K/U, and U/Th ratios suggest that Venusian basalts are the product of similar degrees of partial mantle melting as those on Earth (e.g. Hess and Head, 1990; Treiman, 2007).

Table 1 – Compositions of surface rocks from Venus, obtained by in situ gamma-ray and X-ray fluorescence spectroscopies. Oxides values are given in wt.%; K, U, and Th in ppm. Updated data extracted from Treiman (2007), see references therein for original sources.

	Venera 8	Venera 9	Venera 10	Venera 13	Venera 14	Vega 1	Vega 2
SiO_2	x	x	x	45.1 ± 6	48.7 ± 7.2	x	45.6 ± 6.4
MgO	x	x	x	11.4 ± 12.4	8.1 ± 6.6	x	11.5 ± 7.4
FeO	x	x	x	9.3 ± 4.4	8.8 ± 3.6	x	7.7 ± 2.2
CaO	x	x	x	7.1 ± 2	10.3 ± 2.4	x	7.5 ± 1.4
Al_2O_3	x	x	x	15.8 ± 6	17.9 ± 5.2	x	16 ± 3.6
TiO_2	x	x	x	1.6 ± 0.9	1.25 ± 0.8	x	0.2 ± 0.2
MnO	x	x	x	0.2 ± 0.2	0.16 ± 0.16	x	0.14 ± 0.24
K_2O	x	x	x	4 ± 1.2	0.2 ± 0.14	x	0.1 ± 0.16
Na_2O	x	x	x	n.d.	n.d.	n.d.	n.d.
K	40000 ± 24000	4700 ± 1600	3000 ± 3200	x	x	4500 ± 4400	4000 ± 4000
U	2.2 ± 2.4	0.60 ± 0.32	0.46 ± 0.52	x	x	0.64 ± 0.94	0.68 ± 0.76
Th	6.5 ± 0.4	3.65 ± 0.48	0.70 ± 0.74	x	x	1.5 ± 2.4	2 ± 2

Shellnutt (2013) shows through thermodynamic modeling that silicic rocks can originate through differentiation and partial melting of rocks with the compositions analyzed. In fact,

certain features of the Venusian surface seem to indicate siliceous material, such as the pancake domes, tesserae, and festoon flows. The generation of such rocks would require a fractionation on the order of 90% from the mantle. Also, the generation of granitic rocks requires water. For this reason, the abundance of silicic rocks is not expected because of the planet's apparent lack of water (Gilmore et al., 2017).

II.1.3.1 Surface Morphology and Hypsometry

Hypsometric data show that >80% of the surface of Venus ranges from -1.0 to +2.5 km above the MPR and only 2% lies above the median radius (Figure 4, Mikhail and Heap, 2017 and references therein). In contrast, the surfaces of Earth and Mars have pronounced bimodal hypsometry. The stagnant-lid tectonics on Venus does not explain this discrepancy, since Mars is believed to be under the same tectonic regime.
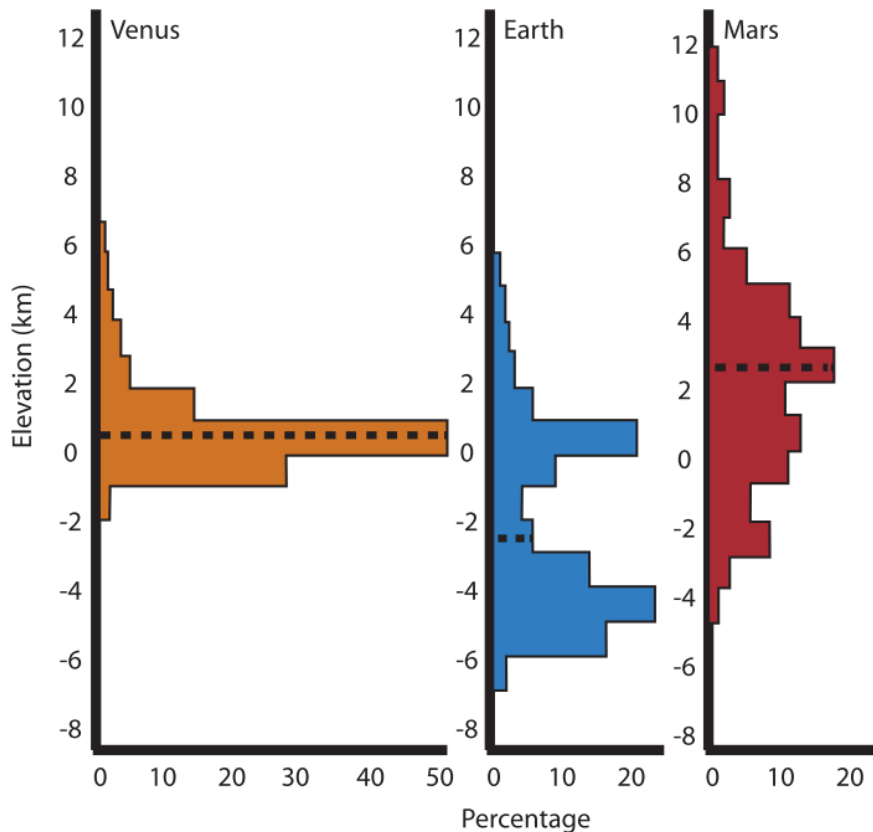
Figure 4 – Hypsography of Venus, Earth, and Mars. Dashed lines mark the MPR. Extracted from Mikhail and Heap (2017). See references therein for sources.

On Earth, plate tectonics, isostatic equilibrium, and erosion produce the observed bimodal hypsometry. The lowest values correspond to subduction trenches and the highest to the pile-up of continental crust during processes of collision (Smrekar et al., 2018).

On Mars, the bimodal hypsometry is driven by the hemispheric dichotomy attributed to giant impacts or Martian particular convection processes in the mantle which build up tall volcanoes (Smrekar et al., 2018).

According to Smrekar et al. (2018), Venusian tessera plateaus can be related to terrestrial continents in terms of topography due to their lower density, however, they cover only ~8% of Venusian surface *vs*. 30% continental crust on Earth. The basaltic crust is not depressed as expressively as on Earth by oceans, and surface water does not erode the topography. Lorenz et al. (2011) suggests that the lack of water erosion on Venus leads to a greater variation in the magnitude of higher elevation topography on the planet in comparison to Earth. These attributes configure a unimodal hypsometry on Venus.

II.1.3.2 Special Crustal Features

Venus has two intriguing crustal features that are constantly addressed in the literature: the coronae and tesserae terrains.

Coronae (Figure 5) are oval to circular volcano-tectonic features typically 100-300 km in diameter unique to Venus. There are hundreds of coronae on Venus, which host tectonically deformed annulus usually standing hundreds of meters above the surrounding plains. The center of these features is commonly lower than the surrounding plains and flooded with plain-forming volcanoes (Basilevsky and Head, 2003). Lobate volcanic flows are habitually seen radiating from coronae. One of the most acceptable models for the corona formation involves mantle plume upwellings causing the cold, dense lower lithosphere to delaminate, sinking into the mantle and deforming the surface (Smrekar and Stofan, 1997).

Mikhail and Heap (2017) present a model for coronae formation (Figure 6). The authors gathered data from deformation experiments with basalts to understand the effects of high surface temperatures on Venus to crustal rheology. The model can be applied to the formation of coronae and also to explain the scarcity of ^{40}Ar in the Venusian atmosphere.
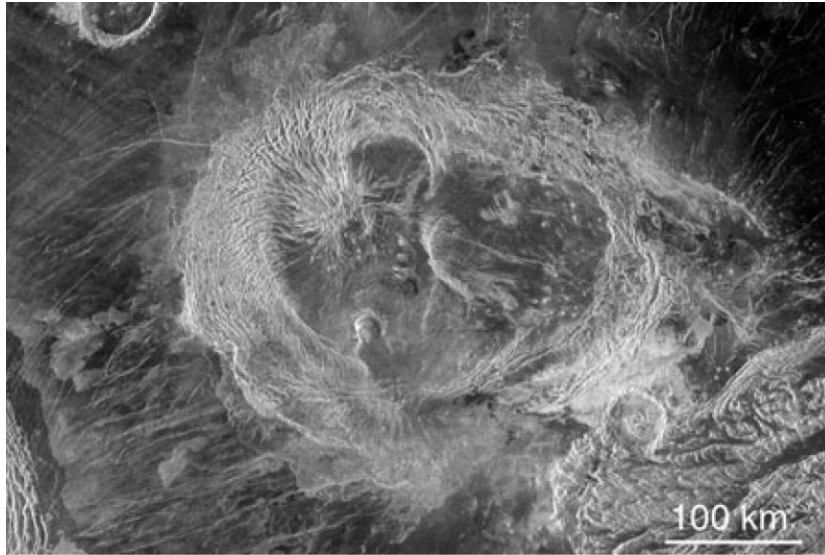
Figure 5 – Pomona Corona, a typical corona structure extracted from Basilevsky and Head (2003). The tectonized annulus of the corona is mostly embayed by the regional plains. Lobate flows emanating from the corona annulus can be seen to the NNW and SW of the corona.
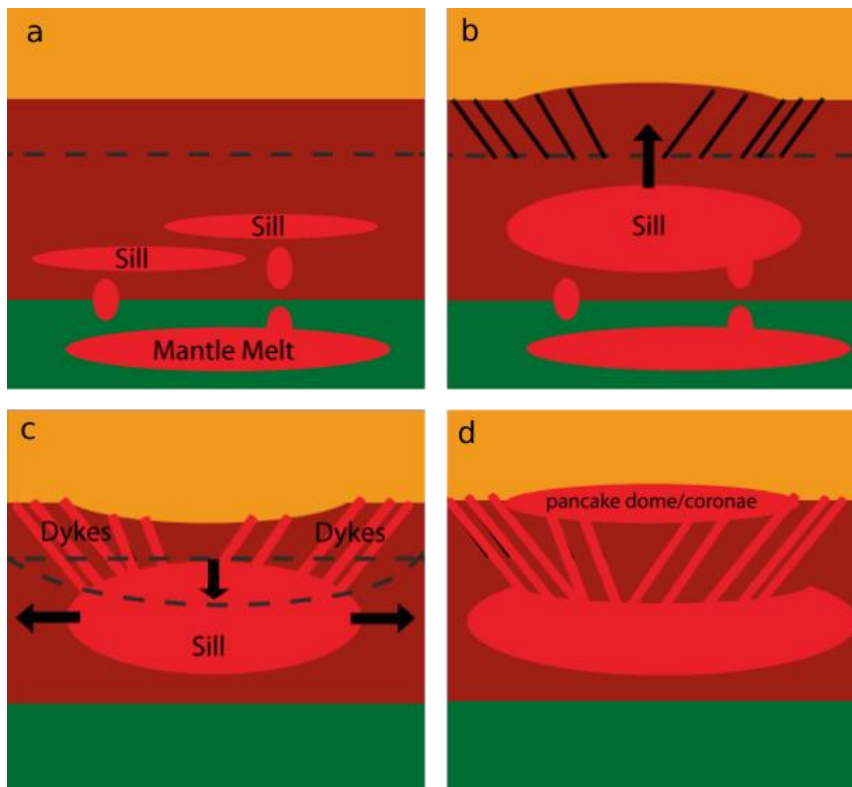
Figure 6 – Model for coronae formation on Venus by Mikhail and Heap (2017). The atmosphere (yellow), lithosphere (dark red), melts (red) and mantle (green) are represented. Black dashed lines represent the brittle-ductile transition zone (BDT). Solid black lines represent fractures. (a) mantle melting and migration into ductile lithosphere (sill-formation); (b) Sill-expansion results in doming and fracturing of the brittle lithosphere; (c) Co-genic collapse

and magma migration through dykes; (d) Short-lived magmatism (pancake dome/coronae formation). Note that dykes only ascend when they reach the BDT.

The tesserae (or tessera terrains, Figure 7) constitute 8-10% of the Venusian surface and occur as a dominant tectonic terrain on Venusian highlands. These intensely deformed terrains make up subcircular crustal plateaus with diameters in the range of 1500 to 2500 km, and elevations of 0.5 to 4 km above the surrounding volcanic plains. They are interpreted as the oldest terrains on Venus and, thus, their formation is fundamental to the understanding of Venusian geodynamic evolution (Romeo and Turcotte, 2008).

Emissivity studies by the VIRTIS instrument aboard Venus Express showed a lower emissivity in tessera terrains in comparison to the surrounding basaltic rocks. This indicates tesserae are composed of rocks with lower Fe than basalts, possibly related to felsic mineralogy in silicic rocks or weathered basalts, the latter being unlikely due to the present lack of water on the Venusian surface (Gilmore et al., 2017).

Silicic magmas on Earth are primarily generated in subduction zones or collisions, although they can also be the product of partial melting from hydrated basalts and eclogites within the lower crust. In both scenarios the presence of water is necessary to produce granitic rocks, indicating tesserae could be a remnant of a water-rich Venus Nevertheless, silicic magmas can also be generated under conditions of low water content as a product of basic melt differentiation, something which has been used to explain felsic rocks on the Moon, Mars, asteroidal meteorites, and Venus (Gilmore et al., 2017 and references therein).

According to Romeo and Turcotte (2008), there are two main hypotheses for the formation of tesserae, one relating them to downwelling and the other to upwelling mantelic flows. The first involves tectonic crustal thickening due to concentric compression caused by a subsolidus flow and horizontal accretion of an ancient thin lithosphere on a cold mantle downwelling flow. The upwelling plume model accomplishes crustal thickening by magmatic underplating and volcanism due to the interaction of an ancient thin lithosphere with a large thermal mantle plume.
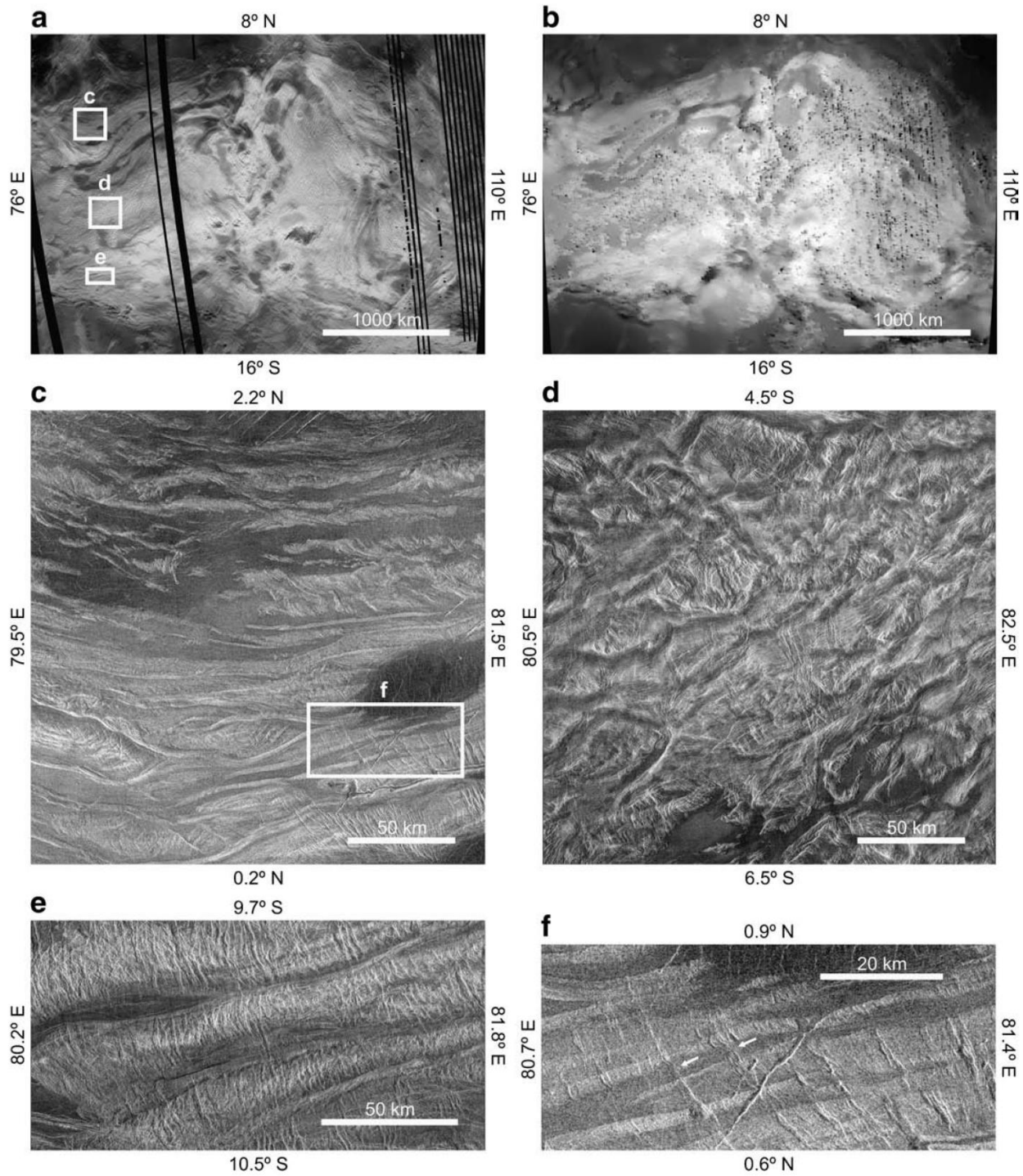
Figure 7 – Different types of tesserae in Eastern Ovda, the largest crustal plateau on Venus. Extracted from Romeo and Turcotte (2008).

14

II.1.4 Atmosphere

Venus has the most massive atmosphere of all terrestrial planets in the solar system, with an average composition of 96.5% CO_2 and 3.5% N_2 and a surface temperature of ~700 K (Basilevsky and Head, 2003). The planet contains about two times more carbon (1.25 x 10^{20} kg of C) and nitrogen (4.8 x 10^{18} kg of N) than the atmosphere, hydrosphere, and sediments of Earth combined (5.4 x 10^{19} kg of C and 3 x 10^{18} kg of N). Its enveloping clouds (Figure 8) are yellowish probably due to the admixture of S or $FeCl_3$ within the droplets of sulphuric acid that compose them (Donahue and Russell, 1997). The wind velocity at the upper boundary of the cloud layer, blowing from East to West (opposite to planet's rotation) is about 100 m/s (Basilevsky and Head, 2003).
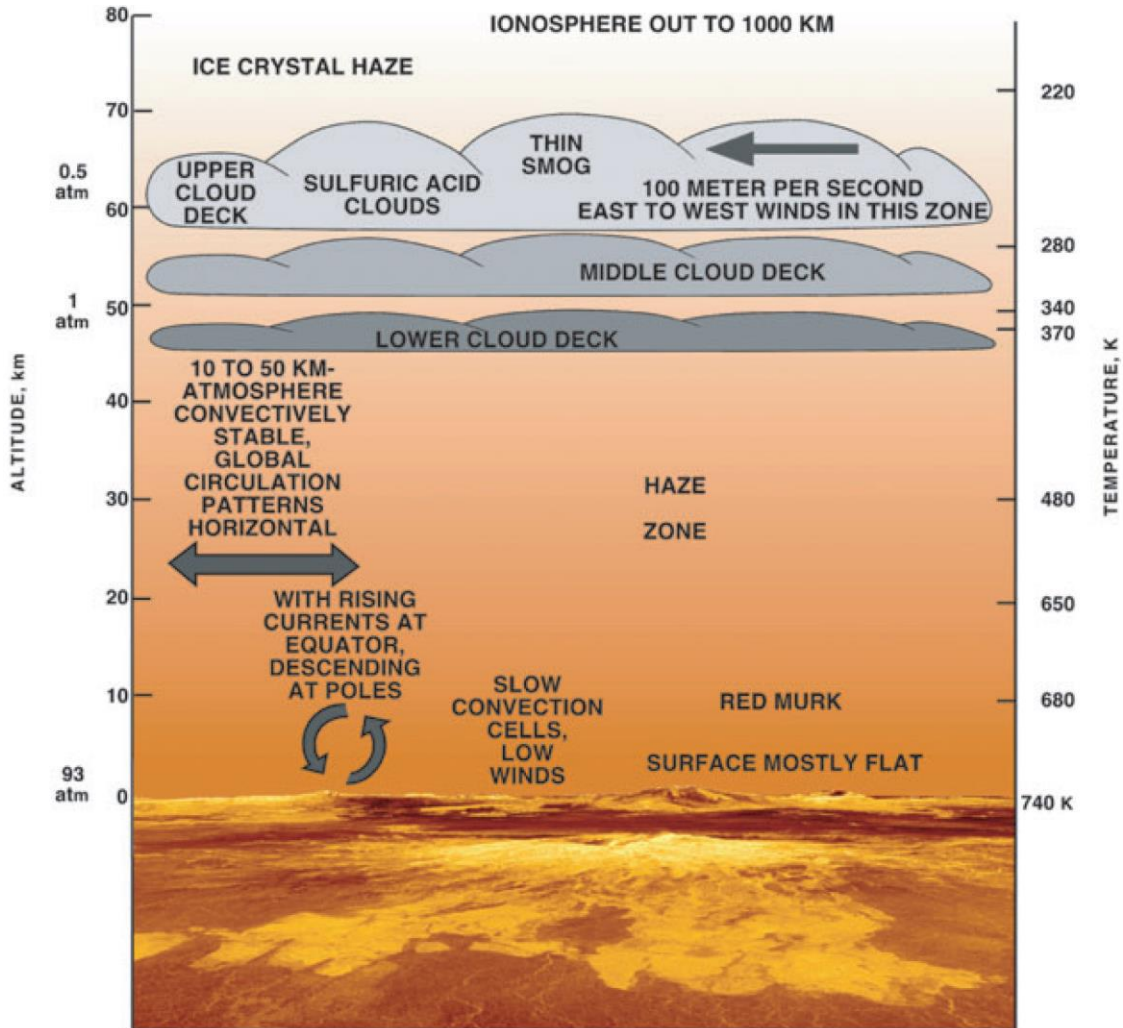
Figure 8 – Schematic structure of Venusian atmosphere as presented by Basilevsky and Head (2003).

The high CO_2 content provides a strong greenhouse effect which is the main responsible for the planet's high surface temperatures (e.g. Pollack et al., 1980; Kasting, 1988).The classical theory for the strong greenhouse effect is that it has been initiated by the evaporation of a water ocean about 100 Ma after the planet formation, resulting in a runaway greenhouse effect. This theory is supported by the deuterium/hydrogen ratio in the Venusian atmosphere (0.024), which is about 150 higher than in Earth's ocean water, meaning a lot of Venusian hydrogen (water) has been lost to space (Donahue and Russell, 1997). Alternatively, Venus' water could be stocked in its mantle, something which has been suggested by Lécuyer et al. (2000)

II.2 Venusian Tectonics and Geodynamics

Earth is the only planet in the Solar System with an active-lid regime in which cold lithospheres are constantly subducted and recycled, cooling the planet's interior and maintaining a global heat cycle (Lenardic et al., 2016). A more common regime in the Solar System is the stagnant-lid regime, where the planet has a sole tectonic plate (Wilson, 2009). This tectonic style is not associated with significant horizontal surface motions and the crust does not participate in mantle overturn and interior cooling (Weller et al., 2015). A third possibility is a transition between the two previously mentioned regimes: the episodic regime, characterized by periods of quiescence (like in stagnant-lid regimes) but with punctual catastrophic overturn events (e.g. Moresi and Solomatov, 1995)

The three tectonic regimes can occur on a planet at different times in its evolution (Figure 9). For example, as Earth cools and internal energy sources are tapped, plate tectonics will begin to wane and eventually cease entirely: Earth will move from a mobile-lid into a stagnant-lid regime (Weller et al., 2015). If the stagnant-lid regime persists for a while, the outer part of the planet may become much cooler, thus denser, than its interior, occasioning instability and consequent lithosphere overturn, entering an episodic regime. It has also been argued that an increase in the long-term surface temperature of a planet can extend to the planet's interior and initiate a transition from active- to stagnant-lid tectonics (e.g. Lenardic et al., 2008; Landuyt and Bercovici, 2009; Weller et al., 2015).

The near-random distribution of impact craters on Venus led to the hypothesis of episodic global resurfacing events. This model proposes that the lithosphere cools and thickens for long

periods (500-1000 Ma) before it gets too dense and becomes unstable. Then, in a short period (~50 Ma), the whole lithosphere overturns and is replaced with a younger buoyant lithosphere, whereupon the subduction-like process stops and the cycle recommences (Ghail, 2015).
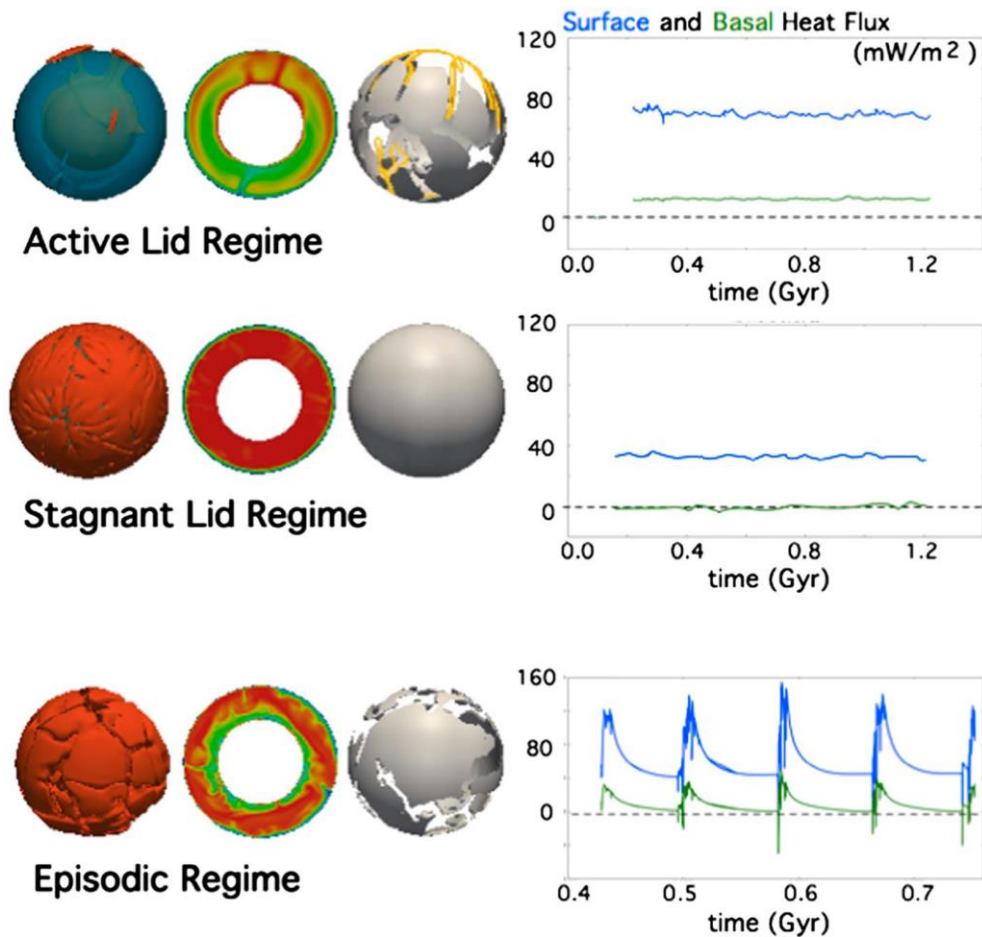
Figure 9 – Different tectonic regimes and surface and basal heat fluxes from 3D numerical mantle experiments (Lenardic et al., 2016). It is widely accepted that Venus is in a stagnant lid regime which may have episodic resurfacing events (episodic regime).

An important parameter that controls the tectonic style, as mentioned earlier, is the surface temperature. Driscoll and Bercovici (2014) suggest that the high surface temperatures enhance the healing of tectonic damage, enabling the development of tectonic plates on Venus. The high surface temperature also affects significantly the rheology of Venusian crust and mantle, greatly influencing geomorphology and tectonics (Bercovici and Ricard, 2014; Mikhail and Heap, 2017).

17

Aitta (2012) shows numerically how surface temperature affects mantle dynamics. The strength of the mantle convection which produces plate tectonics can be measured by the Rayleigh number (Eq. 1). A comparison between Earth's and Venus shows that Earth's Rayleigh number is 86% larger than Venus'. This difference is a consequence of Venus' high surficial temperatures, which results in a smaller ΔT value. A smaller Ra number means mantle convection is less effective on Venus so that its mantle would have 46% smaller convection strength than the Earth's, being a possible explanation for Venus' lack of plate tectonics.

$$Ra = \frac{g\alpha\Delta T d^3}{vK} \qquad (1)$$

Where g is the average gravitational acceleration in the mantle, ΔT the temperature difference between the top and bottom of the convecting layer minus adiabatic temperature difference, d the thickness of the convecting layer, v the kinematic viscosity and k is the thermal diffusivity and α thermal expansivity.

Even though not as vigorous as Earth's, Venusian mantle convection and its consequences are evidenced by deformation above upwelling mantle plumes registered by gravity and topography data provided by the Magellan mission (Smrekar et al., 2018). These hot plumes from the core-mantle boundary create surface uplift and recent volcanism (Smrekar et al., 2010; Davaille et al., 2017, Figure 10). An important aspect of fluid mechanics is the effect of temperature-dependent viscosity on plumes. In Venus, under stagnant-lid convection, most of the temperature or viscosity contrasts seem to occur across the cold top boundary layer (Johnson and Richards, 2003). Jellinek et al. (2002) suggest that this might account for the abundance of transient plumes on Venus relative to Earth. For the latter, lithosphere subduction leads to larger temperature contrasts across the core-mantle boundary than in a stagnant-lid regime. The greater temperature (and viscosity) contrasts stabilize plumes conduits on Earth, whereas on Venus plumes are less stable and more transient (Figure 11).

In a series of experiments relating Ra and plume upwelling, Schaeffer and Manga (2001) show that cold and stiff upper boundary layer behaves almost independently of the lower boundary layer. In contrast, the hot, low-viscosity lower boundary layer generates plumes with a higher characteristic frequency and smaller spacing, as expected, but also with a frequency and

spacing imposed by the cold downwelling plumes (Johnson and Richards, 2003). In summary, a stiff upper boundary layer is only weakly affected by hot, low-viscosity plumes, while the lower boundary layer is strongly influenced by cold stiff downwellings. These results have implications for the formation of Venusian coronae, unique crustal features which are believed to be formed by upwelling plumes (discussed in section II.1.3.2).
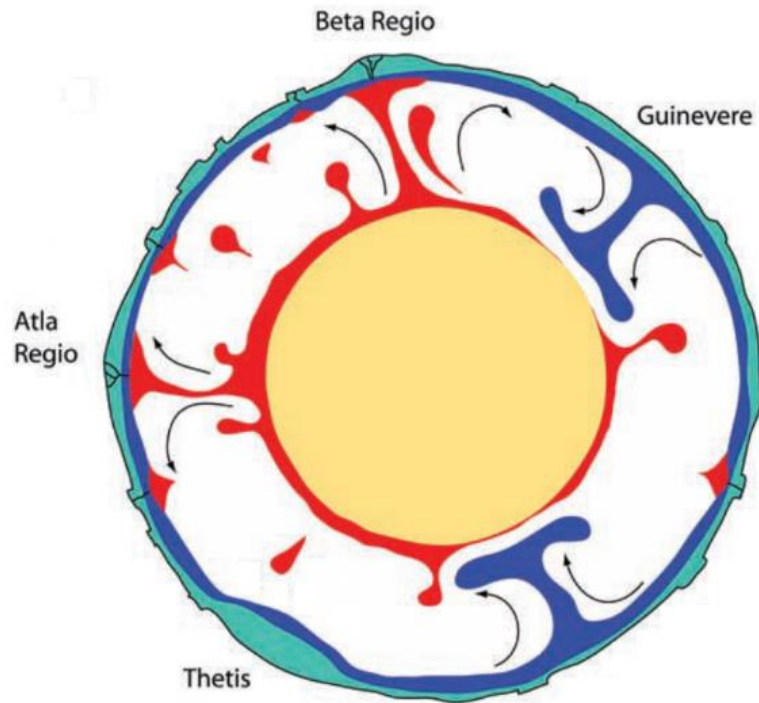
Figure 10 – Schematic model of Venusian geodynamics influenced by mantle plumes from Johnson and Richards (2003).
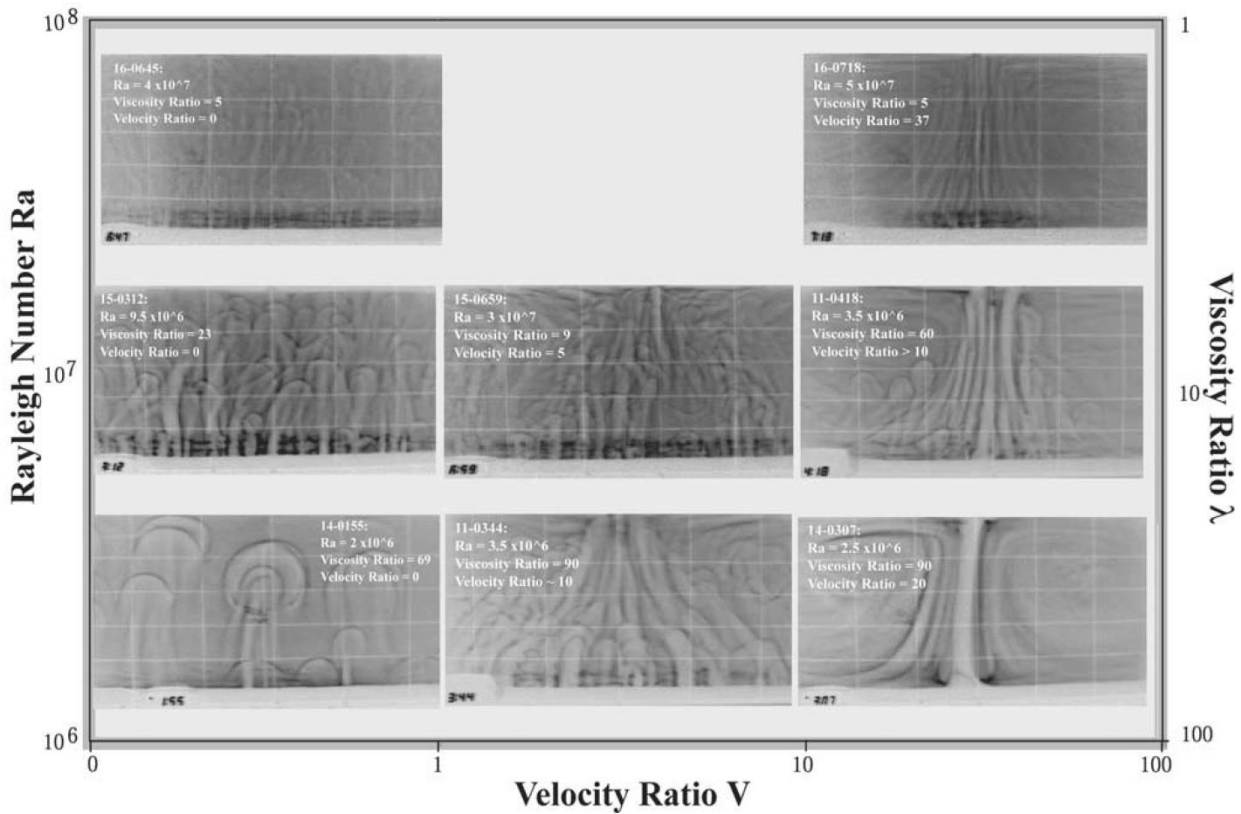
Figure 11 – Shadowgraphs from Johnson and Richards (2003) showing how plume upwelling varies as a function of Rayleigh number, viscosity ratio across the lower thermal boundary layer, and imposed large-scale flow (horizontal velocities).

II.3 Diffusion

Crank (1975) defines diffusion as the process by which matter is transported from one part of a system to another as a result of random molecular motion. In a more recent definition, Zhang (2010) states that diffusion is the random motion of particles (atoms, ions, and molecules) in minerals, glasses, melts, fluids, and gases due to thermal activation on the atomic scale. Nevertheless, this randomness is not entirely true, since molecules do have a preferred direction. If a component is not uniform in the medium, i.e. if there is a chemical gradient or potential, then molecules will move from regions of higher potential to regions of lower potential. This leads to a net flux, which tends to homogenize molecule concentration in the system given enough time (Crank, 1975; Zhang, 2010; Figure 12).
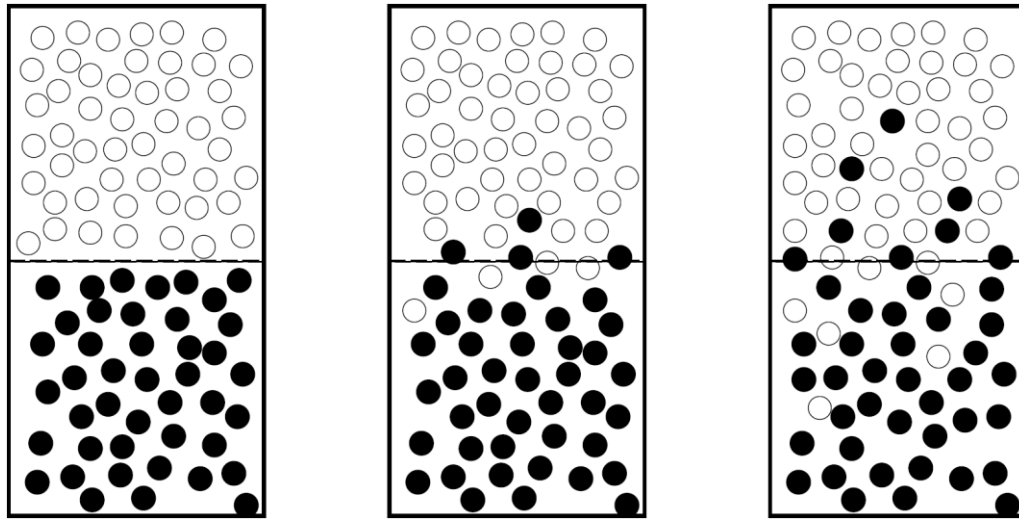
Figure 12 – Example of random motion of particles (diffusion). At first, A particles (Fe^{2+} ions in garnet, for instance) represented by white circles are in the upper part of the rectangle and black circles (Mg^{2+} ions in garnet, for instance), representing B particles, occupy the lower part. Due to random motion, with time, there will be a net flux of A from the upper to the lower rectangle, and a net flux of B from the lower to the upper rectangle. Given enough time, A and B will become eventually randomly, evenly, distributed in the whole system. Extracted from Zhang (2010).

According to Zhang (2010), diffusive transport is the only mechanism for particles to move within a mineral. In silicate melts, mass transport can also occur by flow or convection in addition to diffusion. Even so, in boundary layers, mass transport is driven by diffusion. This mechanism also affects crystal growth and dissolution in melts, crucial processes in magma solidification and evolution. Geochronology also relies on the understanding of diffusion processes acting on minerals, since the loss of radiogenic nuclides from a mineral also occurs through diffusion (^{40}K decaying to ^{40}Ar, for instance).

Thus, understanding the diffusion mechanism is important for different areas in geology and planetary sciences. Early in the 20th century, many geologists studied diffusion in minerals (e.g. Penrose, 1914; Van Orstrand, 1915). The appearance of commercial electron microprobes in the 60s made it possible for more scientists to measure diffusion coefficients, leading to a great increase in the rate of diffusion-related articles (Brady and Cherniak, 2010). Presently, there is a great number of works published addressing diffusion in minerals, melts, and glasses.

Fick (1855) was the first to address diffusion on a quantitative basis based on the equation of heat conduction from Fourier (1822). Fick's equation, known as Fick's 1st Law of Diffusion (Eq. 2), is based on the hypothesis that the rate of transfer of a diffusing substance through the

unit area of a section is proportional to the concentration gradient measured normal to the section (Crank, 1975). This equation considers an isotropic medium, in which structure and diffusion properties are virtually the same in any point or direction.

$$F = -\frac{D\partial C}{\partial x}$$

(2)

Where F is the rate of transfer per unit area of section; C is the concentration of diffusing substance; x the space coordinates measured normal to the section; and D is the diffusion coefficient.

On Eq. (2), the diffusive flux is exclusive to the concentration gradient. In most diffusion studies, it is necessary to describe the relationship between concentration, space, and time. Fick's 2nd Law of Diffusion (Eq. 3), also known as the diffusion equation, is the fundamental differential equation for describing diffusion in one-dimension models.

$$\frac{\partial C}{\partial t} = D\frac{\partial^2 C}{\partial x^2}$$

(3)

Where C is the concentration in a given volume [abundance $*$ length^{-3}]; t is the time of the experiments [time]; D is the diffusion coefficient [length^2 $*$ time^{-1}]; and x is displacement [length].

Fick's 1st and 2nd laws are the basis for most diffusion equations, which vary depending on the medium and components involved (see Crank, 1975 for the other numerous solutions of these equations). This is the case for the Arrhenius Equation (Eq. 4), another important tool for studying the diffusion mechanism.

$$D = D_0 . e^{-Ea/(RT)}$$

(4)

Where D is the diffusion coefficient [length^2 $*$ time^{-1}]; D_0 is the pre-exponential factor (corresponds to D at an infinite time) [length^2 $*$ time^{-1}]; E_a is the activation energy (the necessary enthalpy for forming the activated complex) (J/mol), R is the gas constant (8.314 J/mol.K), T is the absolute temperature (K).

This chapter addresses a general theoretical background necessary to understand the diffusion mechanism and its implications, based mainly on the work of Zhang (2010). A detailed guide on the mathematic formalism for diffusion processes is given in Crank (1975).

II.3.1 Types of diffusion

The diffusion process always involves a diffusion medium and one or more diffusing species. The classification of diffusion depends firstly if it is based on the medium or the species involved. The main types of diffusion are summarized in this section (for details, see Zhang, 2010). Volume diffusion, grain-boundary diffusion and bulk diffusivity (sections II.3.1.1, II.3.1.2, and II.3.1.3, respectively) refer to classifications based on the diffusion medium, while the other sections refer to classifications based on the diffusion species.

II.3.1.1 Volume diffusion

When the term "diffusion" is used without any other qualifiers, it usually means volume diffusion. It is the diffusion occurring in the interior of a phase (e.g. a garnet crystal).

The Fe^{2+} and Mg^{2+} diffusion in a garnet crystal, which leads to the ions' homogenization in the system (Figure 12), is a type of volume diffusion.

The diffusion medium can be isotropic or anisotropic. In the first case, the medium properties do not alter depending on the direction of diffusion (glass, melts, isometric minerals, as garnet). In opposition, within anisotropic mediums, diffusion properties are altered depending on the direction observed. The latter is related to non-isometric minerals or other directional systems.

II.3.1.2 Grain-boundary diffusion

Grain-boundary diffusion refers to the mass transfer mechanisms along interphase interfaces, including mineral-fluid interfaces (or surfaces), interfaces within a crystal, or different crystals. Grain-boundary diffusion is very common since most mineral phases have defects in the crystal lattice, forming different interphases. Diffusion along grain boundaries occurs at higher rates than in volume diffusion. For instance, the grain-boundary diffusivity of Si at forsterite-forsterite boundaries is about 9 orders of magnitude greater than the volume diffusivity of Si in

forsterite at a 1473 K temperature (Farver and Yund, 2000). Sometimes the term 'interface' diffusion is also used to address grain-boundary diffusion.

II.3.1.3 Bulk Diffusivity

This type of diffusion is also referred to as 'effective diffusion' and is central to this work. Here, the analysis is based on the average diffusivity in a heterogeneous medium. This means that within the analyzed system, different phases, grain boundaries, or components may exist, representing multiple diffusion domains. The bulk diffusivity addresses the overall diffusivity, which can be used to understand diffusion in multi-phase solids (such as rocks or crystals), multi-grain single-phase solids, or porous materials (Zhang and Liu, 2012). In rocks, the bulk diffusivity results from the combination between the volume diffusion occurring within minerals, and the grain-boundary (or interface) diffusion. This relation is shown by Eq. 5. This approach is highly important to geological and planetary sciences because the systems studied are usually complex and heterogeneous, so the measurement of diffusion in individual homogeneous materials (volume or lattice diffusion) or grain boundaries may be insufficient to describe the overall (bulk) diffusivity.

$$D_{bulk} = D_l + \left(\frac{3\delta}{d}\right).D_{if} \tag{5}$$

Where D_{bulk} is the bulk diffusivity; D_l is the lattice or volume diffusion in a crystal; δ is the interface width; d is the grain size; D_{if} is the interface or grain-boundary diffusion.

II.3.1.4 Self-diffusion

This type of diffusion occurs in a system with no chemical potential, i.e. if the system is entirely homogeneous and uniform. Different isotopes of the same element, which do not conFigure a chemical gradient, are used to measure this type of diffusion.

For example, a diffusion couple of ^{44}Ca and ^{40}Ca in a basaltic melt where one side is more enriched in ^{44}Ca than the other. This does not constitute a chemical potential but the particles will move randomly and the diffusion rates can be measured by tracking the isotopes' mobility.

II.3.1.5 Tracer diffusion

Molecules of a tracer element that was absent (or had very little concentrations) in the system are introduced to address its diffusivity. In this kind of diffusion, the system is essentially uniform, with the only variation being the introduced tracer.

Figure 13 shows a typical example of a tracer diffusion experiment. The tracer, previously virtually inexistent in the system, is added onto one side of the system and can have its mobility tracked.
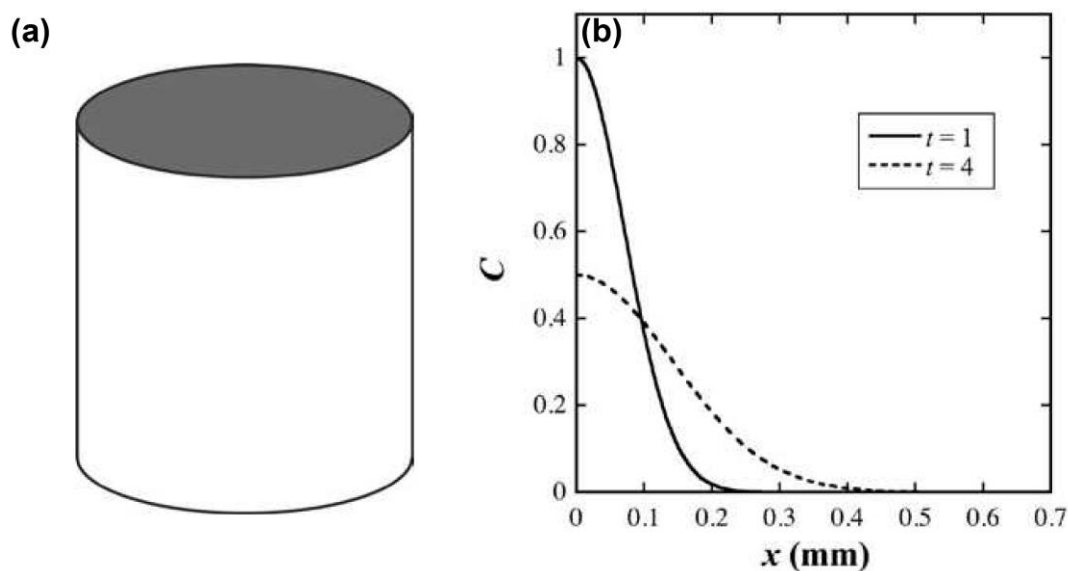
Figure 13 – Tracer diffusion example from Zhang (2010). On (a), a tracer, previously absent in the system, is added onto the upper part of the medium. On (b), the diffusion profile shows the travel distance of the tracer across the system, where the vertical axis is the tracer concentration (C), and the horizontal axis represents the distance (x).

II.3.1.6 Chemical Diffusion

This kind of diffusion occurs when there is a chemical gradient in the system. Can be divided into 'trace element diffusion' when a situation similar to the one described in 'tracer diffusion' occurs, but the tracer element is less than 1 wt.%, with a minor chemical gradient; 'binary diffusion' when a binary system is used (e.g. Fe-Mg diffusive exchange in olivine or garnet); 'Multispecies diffusion' when the diffusing component can be present in two or more species (e.g. CO_2 diffusion that may be in the form of carbonate ions and CO_2 molecules; (Nowak et al., 2004); 'Multicomponent diffusion' when the diffusive transport involves three or more components in the system (e.g. different crystals in a rock).

II.3.2 What affects diffusion

Many parameters affect the diffusion process. Here, the most relevant ones are summarized.

II.3.2.1 Temperature

In short, higher temperature means higher diffusivity. This can be perceived logically since a rise in temperature means more agitated molecules. The Arrhenius Equation (Eq. 4) reflects well this relationship.

Many diffusion experiments show that particles follow Arrhenian behavior, i.e., values fit into straight lines with a negative slope in log D vs. 1 (or 1000)/T plots (Figure 14).
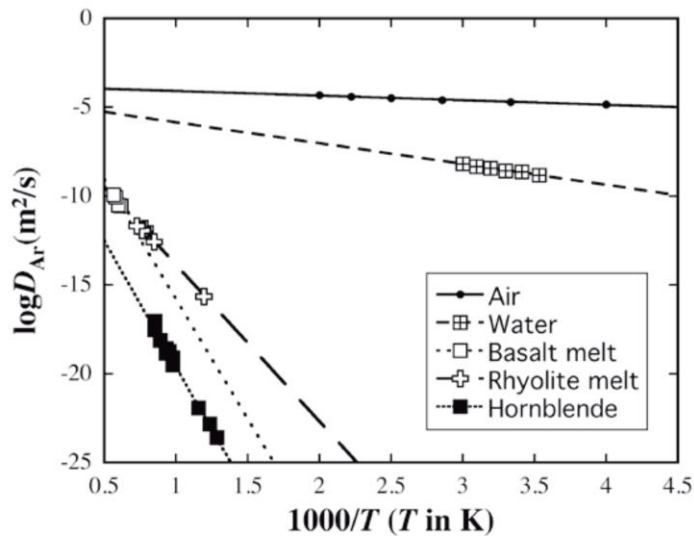
Figure 14 – Ar diffusion data showing Arrhenian behavior (Zhang, 2010, see references therein for sources).

II.3.2.2 Pressure

The relation between pressure and diffusion is complex. In a small pressure range, log D is usually linear with P, showing that a raise in P results in a smaller diffusivity (Figure 15). Nevertheless, D can also increase with pressure at higher pressures (Figure 16). This is shown by Eq. 6, a variation from Eq. 4:

$$D = D_0 . e^{-(E+P\Delta V)/(RT)} \qquad (6)$$

Where E is the activation energy at zero pressure, P is a given pressure, ΔV is the activation volume (volume difference between the activated complex and the non-activated state). $E + P\Delta V$ is the activation energy at pressure P.
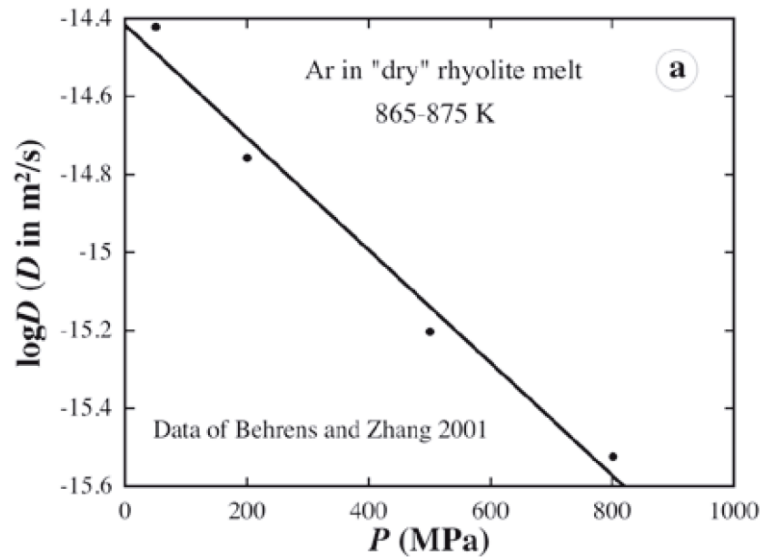
Figure 15 – Log D vs. P plot showing that diffusivity decreases with increasing pressure. Data from Behrens and Zhang (2001) shown in Zhang (2010).
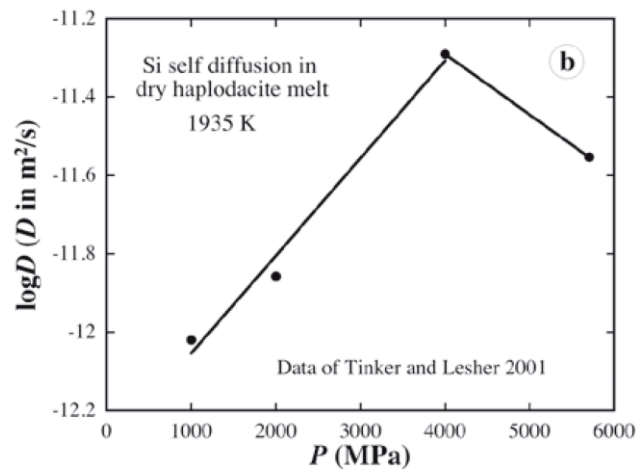
Figure 16 – Diffusivity first increases, and then decreases with pressure on data from Tinker and Lesher (2001). This is caused by the variations in the activation volume (ΔV). First, ΔV is < 0, at ~ 4000 MPa, $\Delta V > 0$. Extracted from Zhang (2010).

The activation energy for diffusion is always positive. However, the activation volume can be either positive or negative, resulting in negative or positive slopes for log D, respectively. The latter explains why diffusion can increase or decrease with increasing pressure.

II.3.2.3 Crystalline Phases and Defects

The crystal lattice usually presents gaps, or defects, in its structure. Diffusion usually occurs through these defects. Atoms "jump" into a defect, leaving another one vacant for another atom to jump in, and so on.

Defects can be classified as point defects or extended defects. The first include vacancies (unoccupied sites that are normally occupied), interstitials (atoms occupying normally unoccupied sites), and impurities (atoms occupying sites that are normally occupied by other atoms, e.g. Al occupying a Si site). Impurities are classified as an extrinsic defect, whereas the others are intrinsic defects. Extended defects include line defects (e.g dislocations), plane defects, domain boundaries, grain boundaries (e.g. crystalline phases), and bulk defects or impurities (such as a fluid inclusion). Point defects play the most important role in volume diffusion, but extended defects may produce fast diffusion paths.

In short, a higher number of defects (e.g. in response to tectonic deformation) in the crystal lattice means a higher diffusion rate.

II.3.2.4 Oxygen Fugacity

Oxygen fugacity affects the oxidation state of multivalent elements (e.g. Fe^{2+} and Fe^{3+}; Eu^{2+} and Eu^{3+}). Usually, the diffusivity of the reduced species is higher than the oxidized one. This occurs because, generally, reduced species make weaker bonds with the rest of the structure.

Ergo, increasing oxygen fugacity usually decreases the diffusivity of an element of interest.

II.3.2.5 Composition

The major and minor chemical compositions of both the medium and species affect the diffusivity of a component. For example, the addition of H_2O into rhyolite melts increases Ar diffusion exponentially (Behrens and Zhang, 2001).

The silicate network plays an important role in diffusion. Si^{4+} is a network former while ions such as Ca^{2+}, Na^+, K^+, and Mg^{2+} act as network modifiers (Amalberti et al., 2016). The

addition of modifier cations depolymerizes the Si-O-Si glass network by breaking Si-O bonds and forming non-bridging oxygens (NBO, Le Losq et al., 2014). This leads to an increase in diffusion since NBO creates pathways (extended defects) through which atoms diffuse faster (Amalberti et al., 2016). The breaking of Si-O bonds and the formation of NBO also explains the changes in diffusion rates between glasses and melts (Figure 17).

Also, diffusivities of most components decrease as SiO_2 content increases, often showing linear relation between log D and SiO_2. Nevertheless, in some cases increasing SiO_2 content increases diffusion. It is the case of He, Li, and Na (Behrens, 2010)
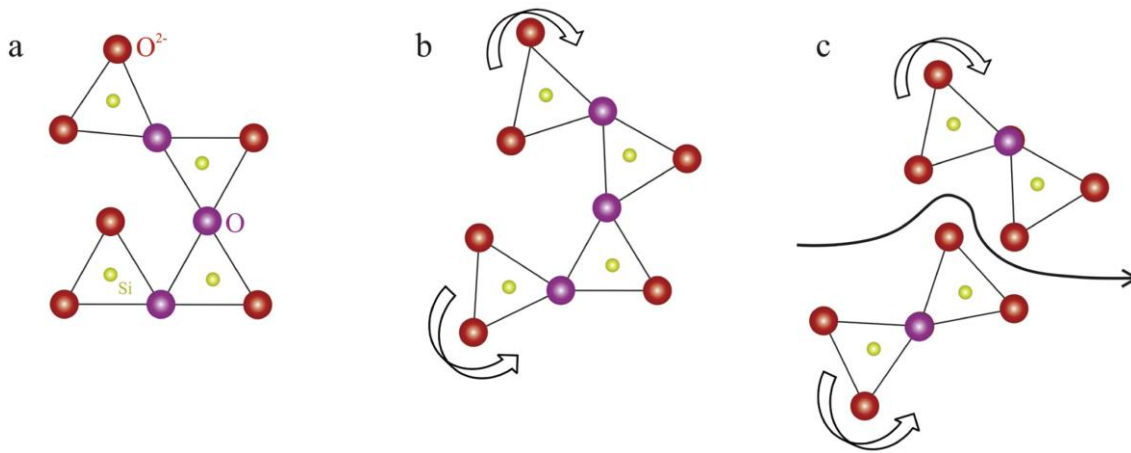
Figure 17 – The effects of altering silica network in diffusion (Amalberti et al., 2016). Non-bridging oxygens (O^{2-}) are represented by red circles; bridging oxygens (O) are represented by purple circles. (a) glass state; (b) glass transition; (c) melt. There is an increase in diffusion from (a) to (c) due to the formation of NBOs.

II.3.2.6 Relation between Particle Size, Charge, and Medium Viscosity

The Stokes-Einstein equation (Eq. 7) is the classical one to relate diffusivity, viscosity, particle radius, and temperature, as follows:

$$D = \frac{k_B T}{6\pi a \mu} \tag{7}$$

Where k_B is the Boltzmann constant (1.3807 x 10^{-23} J/K), a is the radius of the particle, and μ is the fluid viscosity.

This equation works well when addressing the diffusion of heavier noble gases or other relatively large neutral molecules in aqueous solutions. However, it does not work for the diffusion of any known neutral species in silicate melts.

The melt viscosity is not necessarily inversely proportional to the diffusivity. For instance, tracer diffusivity of Li and Na increases as viscosity increases from basaltic to rhyolitic melts (Zhang et al., 2010).

Also contrary to the Stokes-Einstein equation, the relation between size of the diffusing species and diffusivity is not universal. For instance, the ionic radius increases from $Li^+ < Na^+ < K^+ < Rb^+ < Cs^+$, but the tracer diffusivity decreases from $Na > Li > K > Rb > Cs$ by orders of magnitude (e.g. Jambon, 1982). The opposite behaviour happens with the alkaline earth elements, ionic radii increasing from $Be^{2+} < Mg^{2+} < Ca^{2+} < Sr^{2+} < Ba^{2+}$, and tracer diffusivity decreasing from Sr and Ba > Ca > Mg > Be (Mungall et al., 1999). On the last case, smaller cations have lower diffusivity, opposed to what Eq. 6 suggests.

As mentioned earlier, the diffusivity of ionic species decreases with increasing charges (negative or positive), because of the stronger bonds created with higher charges.

II.3.2.7 Ionic Porosity

The ionic porosity (IP) is the measure of the "empty" spaces in a structure. Since diffusion is driven by the random motion of particles, more "empty" spaces mean more diffusion. IP can be calculated using the general and simple Eq. 8.

$$IP = 1 - \frac{V_{ions}}{V_{total}}$$
(8)

Where V_{ions} is the calculated volume of anions and cations in the medium; and V_{total} is the unit cell volume of the medium.

II.3.3 Diffusion of noble gases

The noble gases (helium, neon, argon, krypton, xenon, and radon) constitute Group 0 (column 18) of the periodic table. They are highly volatile, colorless, odorless, monatomic, and unreactive at standard temperature and pressure (Ballentine and Barry, 2017).

Noble gases are ideal neutral tracers of diffusion because their chemical inertness inhibits

the formation of bonds that could affect the glass/liquid/crystal structure (Amalberti et al., 2016). Figure 18 shows a general view of the different diffusivities of all noble gases in different environments, while Figure 19 shows the different activation energy for each noble gas (and H_2O). For more detailed information on noble gas diffusion in silicate glasses and melts, see Behrens (2010).
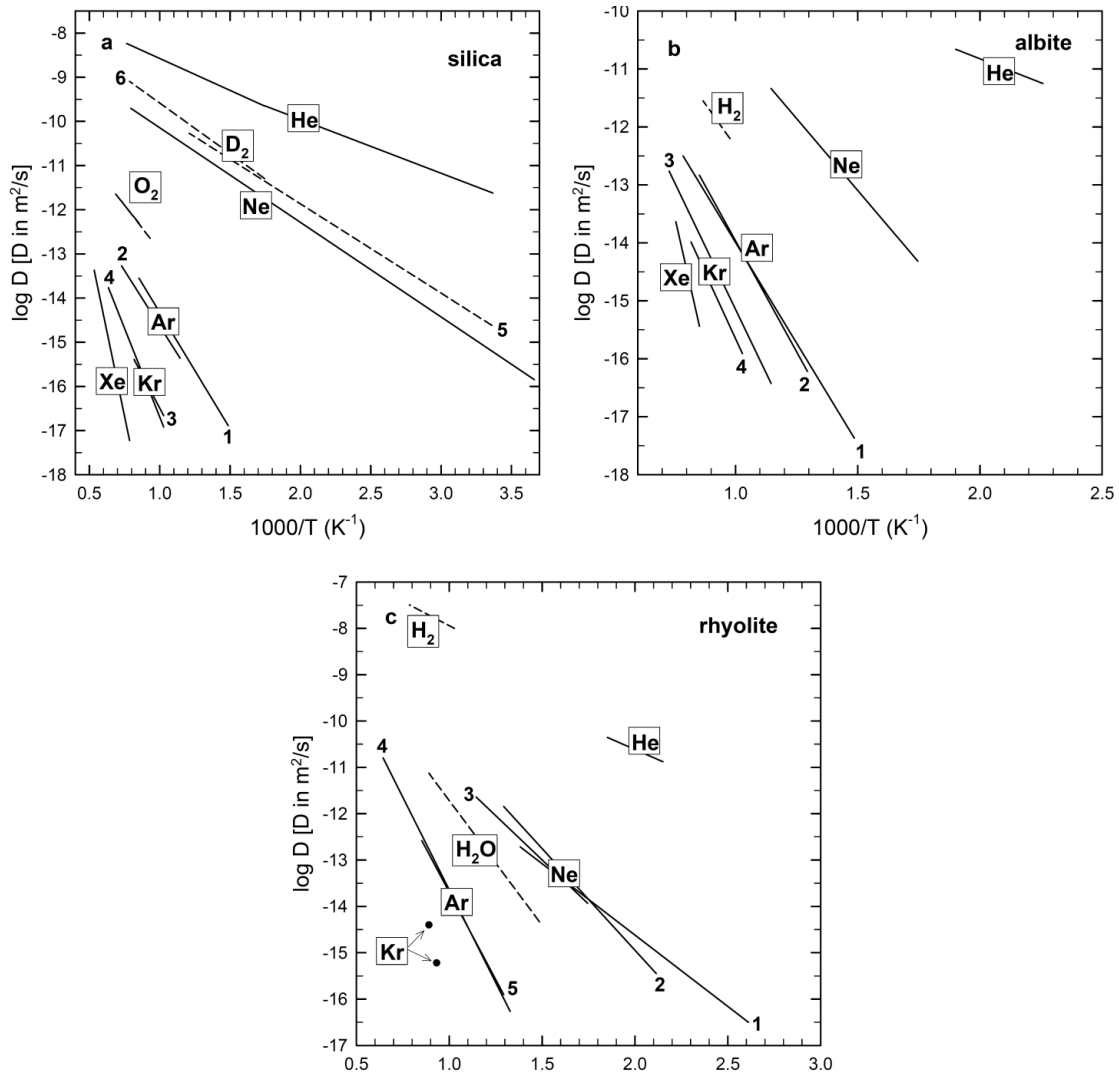
Figure 18 – Noble gas diffusion (solid lines) and molecular diffusion (dashed lines) in glasses and melts at near-ambient pressure, if not specified (compiled by Behrens, 2010). See references therein for each data reference (a) Si glass. Ar 1 = 20-373 MPa, Kr 3 = 152-315 MPa; (b) Albite ($NaAlSi_3O_8$). Ar 2 = 118-371 MPa, Kr 4 = 23-315 MPa, H_2 = 180 MPa. (c) Water-poor rhyolite glasses and melts. Ne 1: tektite, Ne 2,3 two different obsidians. Ar 4 = 116-373 MPa, Ar 5 = 200 MPa.
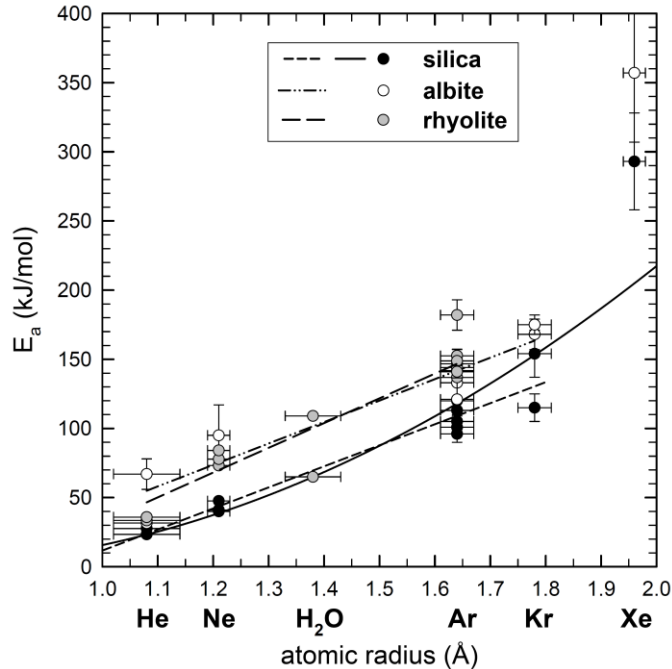
Figure 19 – Comparison of activation energies for noble gases in SiO_2 glass, albite, and rhyolite glass and melts (Behrens, 2010). H_2O spherical molecule included for comparison. Note that activation energy increases with increasing atomic radius.

II.3.4 Ar diffusion in basaltic systems

Earth is the only known terrestrial planet with an active-lid tectonic style, in which lithospheres are constantly recycled in the planet (Lenardic et al., 2016). On Earth, magma (and rock) compositions are tightly linked to the location in which the melts were generated. For example, chains of elongate volcanoes in the deep oceans form the ocean ridges, composed of relatively metal-rich, silica-poor volcanic rocks called basalts. These rocks are direct partial melts of the underlying mantle as it rises and decompresses in response to the spreading apart of lithospheric plates. Other chains of volcanoes are created along convergent plate boundaries (subduction zones), generating silica- and volatile-rich, metal-poor rocks (andesites). Intraplate volcanism is a third different way of generating magma, representing locations of unusually vigorous mantle upwelling resulting in a variety of compositions (Wilson, 2009).

A more common regime in the Solar System is the stagnant-lid regime, where the planet has a sole tectonic plate. This tectonic style is not associated with significant horizontal surface motions and the crust does not participate in mantle overturn and interior cooling (Weller et al., 2015). In such systems, magmatism is believed to be generated by the partial melting of

upwelling mantle plumes. The products are rocks with compositions similar to those of terrestrial tholeiitic basalts (Wilson, 2009). The only samples ever returned from other bodies in the Solar System were those collected from the Moon by the Apollo missions, which show basaltic compositions (Shearer, 2006). Basaltic compositions are also observed in the *in situ* chemical analysis on the surface of Mars and Venus. Remote sensing from orbiters on Mercury and Io (one of Jupiter's moons) also indicates basaltic volcanism in those planets (Wilson, 2009). On Venus, the crust holds K/U ratios and Si, Fe, Mg, and Mn abundances similar to those of terrestrial mid-oceanic ridges, being associated with tholeiitic basalts (Bougher et al., 1997). In summary, the basaltic composition seems to be a good guess for the bulk crustal composition of a terrestrial planet and thus, studying the diffusion of Ar in basaltic systems may provide valuable information about rocky planets.

The diffusivity of Ar has been studied in several different conditions mostly because of its implications to geochronology with the K-Ar and Ar-Ar methods. Thermochronometry by the $^{40}Ar/^{39}Ar$ technique addresses many areas of Earth and planetary processes, such as mountain uplift and erosion, pluton emplacement and cooling, regional metamorphism, asteroid accretion and cooling, and shock metamorphism of meteorites and their parent bodies (Cassata et al., 2011 and references therein).

Ar diffusivities were determined in single gem-quality crystals or crystal powder (e.g. Foland, 1974; Mark Harrison, 1981; Harrison et al., 1985, 2009; Fortier and Giletti, 1989; Foland and Xu, 1990; Cassata et al., 2011; Popov et al., 2020); silicate melts (e.g. Behrens and Zhang, 2001; Nowak et al., 2004; Spickenbom et al., 2010; Amalberti et al., 2016; Guo and Zhang, 2016, 2018); or glass (e.g. Reynolds, 1957; Carroll, 1991; Carroll and Stolper, 1993; Amalberti et al., 2016). Authors have also calculated the bulk diffusivities of different materials in rocks before (e.g. Becker and Shapiro, 2000; Boving and Grathwohl, 2001; Zhang et al., 2004; Moldrup et al., 2007; Peng et al., 2012; Zhang and Liu, 2012). These studies are usually related to the relationship between diffusivity and pore size/distribution, with implications for the industry sector. However, data concerning the bulk diffusivity of Ar in whole rocks are absent in the literature. Since rocky planets are made of silicic rocks and magma, the diffusivity of single crystal phases is not enough to describe the diffusivity of the system, making it harder to extract information from the Ar atmospheric geochemistry data obtained from these planets.

Figures 20 and 21 show the results of argon diffusion experiments with polymerized glasses and melts. The plots show that increasing alkali content increases Ar diffusion.
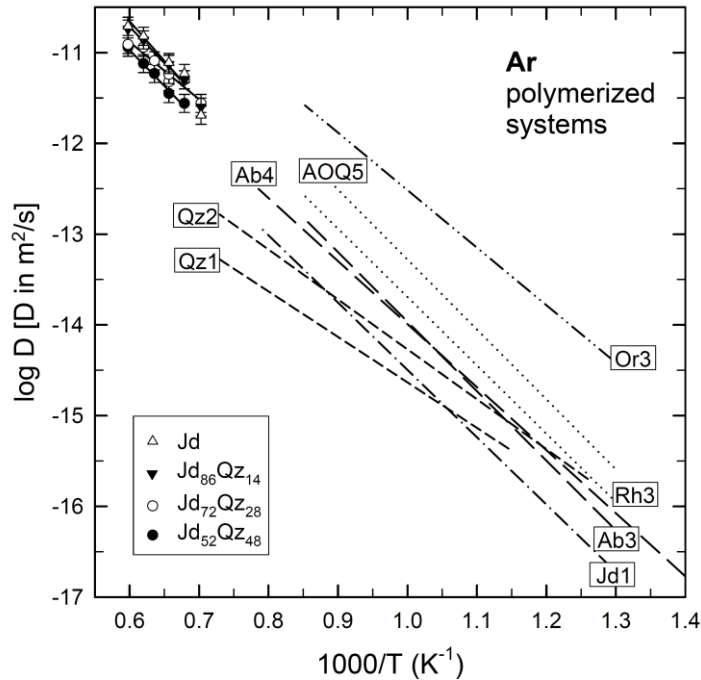
Figure 20 – Ar diffusion data in various polymerized glasses and melts (Behrens, 2010, see references therein for sources). Symbols and solid lines correspond to high-T melts of the join Quartz-Jadeite at 500 MPa. Non-sold lines are Arrhenius relationships for glasses and super-cooled melts. Qz1, Jd1: silica and jadeite composition at near-ambient pressure. Qz2: silica composition at ~200 MPa; Ab3, Or3, Rh3: albite, orthoclase, and, rhyolite compositions, respectively, at ~200 MPa; Ab4: albite composition at near-ambient pressure; AOQ5: metaluminous haplogranite AOQ at 200 MPa.
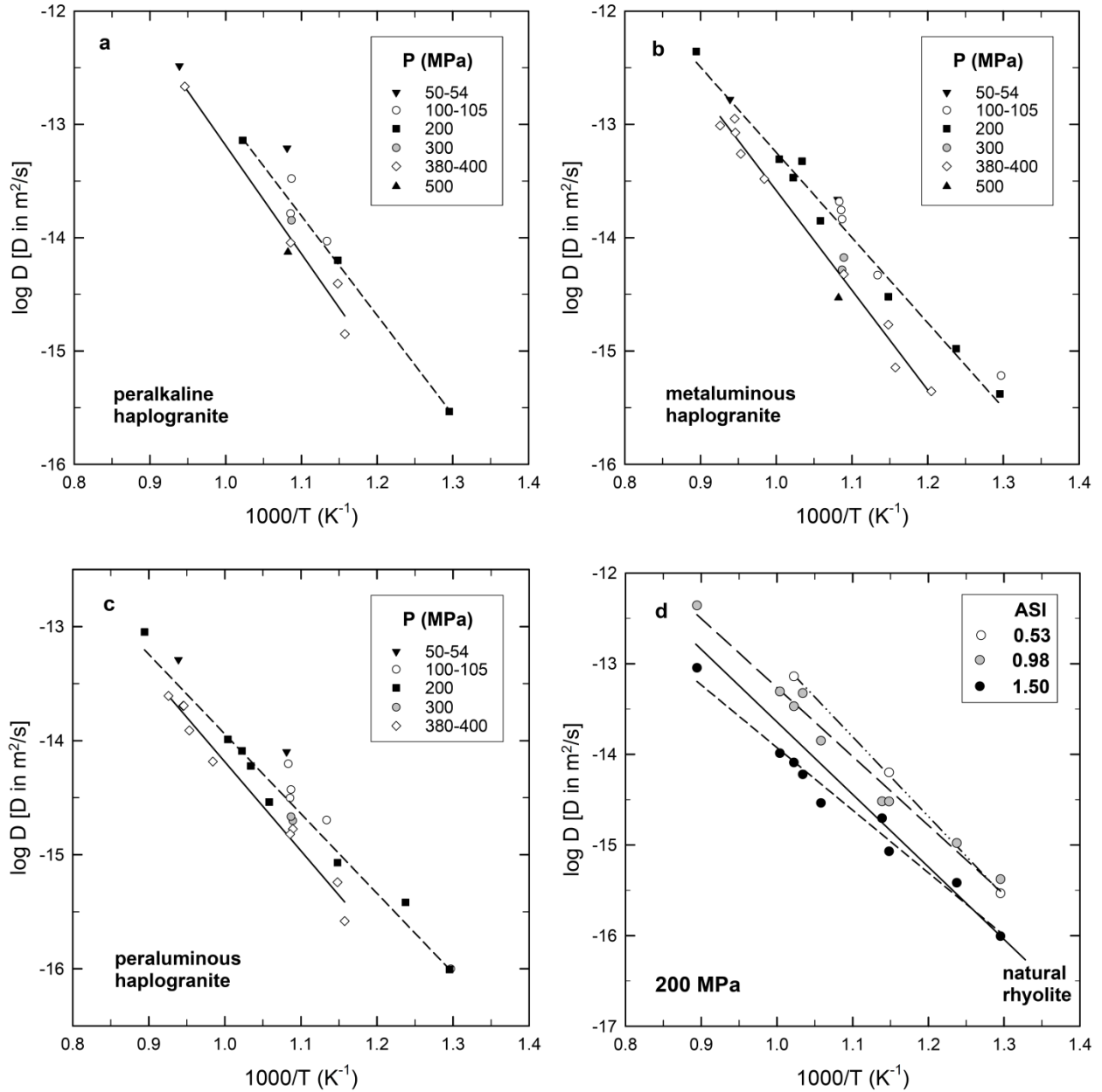
Figure 21 – Arrhenius plots for Ar diffusion in haplogranite glasses with different alumina/alkali contents from Behrens (2010). a) peralkaline melts (ASI = 0.53; AOQPB) at various pressures; b) metaluminous melts (ASI = 0.98; AOQ) at various pressures; c) peraluminous melts (SI = 1.50; AOQPB) at various pressures. Solid lines are regressions to data at 380-400 MPa, dashed lines are regressions to data at 200 MPa.; d) Comparison of diffusivities at 200 MPa. Note that the solid line for dry natural rhyolite after Behrens and Zhang (2001) is systematically below the data for metaluminous halogranite.

II.3.4.1 Ar Diffusion in Plagioclase

A wide range of results constraining diffusion in plagioclase is shown in Figure 22.

Cassata et al. (2009) analyzed Ar diffusion in plagioclase crystals from the Bushveld Complex (South Africa) to constrain the thermal history of the area. Some of the results, relevant to the present work, are presented in Figure 23. These results show that the diffusion kinetics of each plagioclase crystal is intrinsically different. Variations can be related to differences in the quantity, orientation, and interaction of structural and chemical defects of each crystal, as well as subtle variations in shape and chemical zoning. The authors defined activation energies of 155-178 kJ/mol and $\ln(D_0/a^2)$ values between 3.5 and 6.5. These diffusion parameters correspond to closure temperatures of 225-300ºC for a 10ºC/Ma cooling rate.
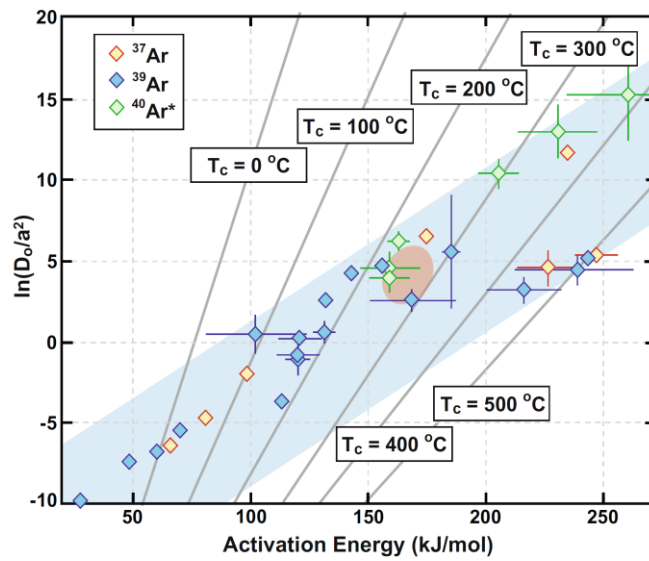
Figure 22: Kinetic parameters for the diffusion of [40]Ar, [39]Ar, and [37]Ar in plagioclase from existing data (see text for sources), extracted from Cassata et al., 2009. The red oval spans the range of diffusion parameters presented on that paper.
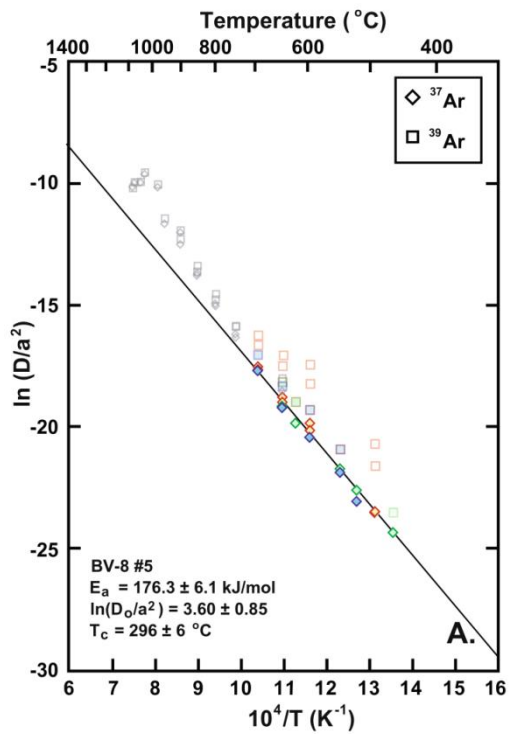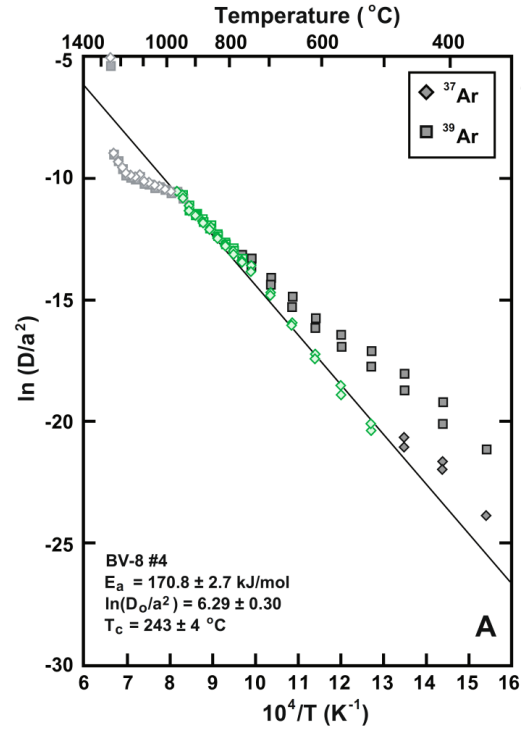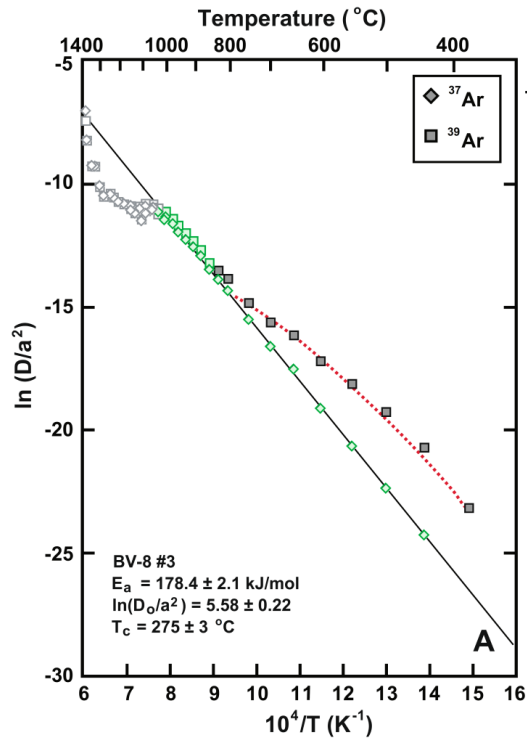
Figure 23 – Ar diffusion data in plagioclase from Cassata et al. (2009). BV-8#3, 4, and 5 are the sample identifications. E_a is the activation energy. $Ln(D_0/a^2)$ is the frequency factor. T_c is the closure temperature. Differences in values are probably linked to intrinsic differences in crystals' internal composition or imperfections.

II.3.4.2 Ar Diffusion in Pyroxene

A big quantity of Earth's [40]Ar is carried by pyroxenes in the mantle and crust. Clinopyroxene inclusions within diamonds contain up to 1.4 wt% K (Cassata et al., 2011).

A few authors have addressed Ar diffusion in pyroxenes in the past. Amirkhanov et al. (1959) first reported an E_a for [40]Ar in pyroxene crystals of 307 kJ/mol. Schwartzman and Giletti (1977) registered an E_a of > 301 kJ/mol, also for [40]Ar. Many works addressing whole-rock meteorites registered E_a from 300 to 406 kJ/mol (e.g. Kunz et al., 1997; Cassata et al., 2010). Watson et al. (2007) constrained diffusion parameters in enstatite crystals (orthopyroxenes, OPX), finding D_0 = 1.4 x 10^{-20} m^2/s and E_a = 32.2 kJ/mol, assimilating similar values for clinopyroxenes (CPX).

The big differences in values acquired by Watson et al. (2007) and the other authors lead Cassata et al. (2011) to further investigate Ar diffusion in pyroxenes. Thus, Cassata et al. (2011) ran experiments with CPX and OPX gem-quality crystals to constrain Ar mobility within these systems.

The main results from Cassata et al. (2011) are shown in Figures 24, 25, and 26. These show that CPX crystals yield an average E_a of ~379.2 kJ/mol and D_0 of ~1.36 x 10^{-4}, while OPX crystals yield an average E_a of 371 kJ/mol and D_0 of ~5.73 x10^{-2}. The experiments show Arrhenius arrays between 850 and 1350ºC, and defined closure temperatures were 600-800ºC for a 10ºC/Ma cooling rate and 0.1 - 1mm grain size. These data indicate that radiogenic [40]Ar should be degassed rapidly from Earth's mantle during partial melting events.
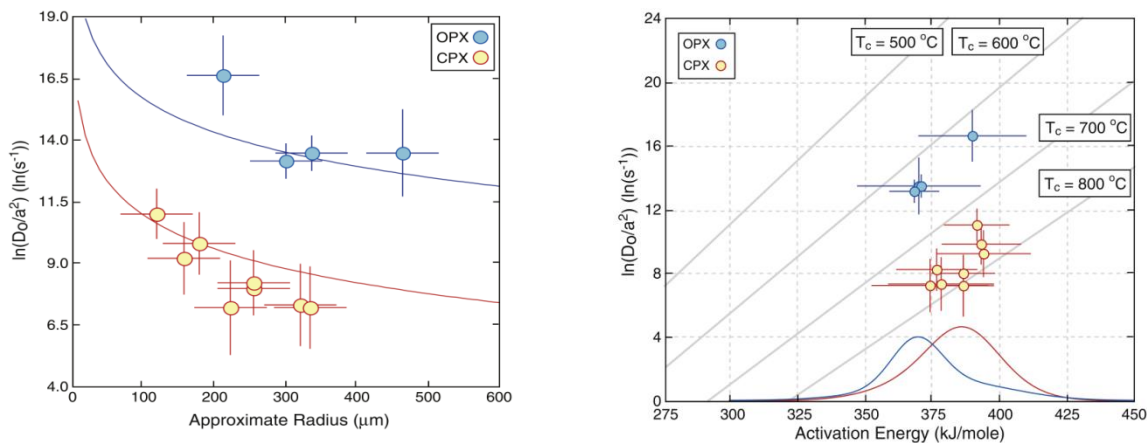
Figure 24 – Plots from Cassata et al (2011). Left plot: approximate diffusion lengthscale versus $\ln(D_0/a^2)$. If each CPX and OPX crystal is characterized by the same D_0 and differences in $\ln(D_0/a^2)$ values are only due to grain size variations, data were expected to plot on the red and blue lines, respectively. Since the observations are in fair

agreement with these relationships, it appears that grain size variations account for at least most of the observed variance in $\ln(D_0/a^2)$ values and therefore that the physical crystal dimensions define the diffusion domain boundaries. Right plot: Summary of kinetic parameters for the diffusion of ^{37}Ar in CPX and OPC. Lines correspond to closure temperatures (Dodson, 1973) between 500 and 800°C, calculated for a 10°C/Ma cooling rate.
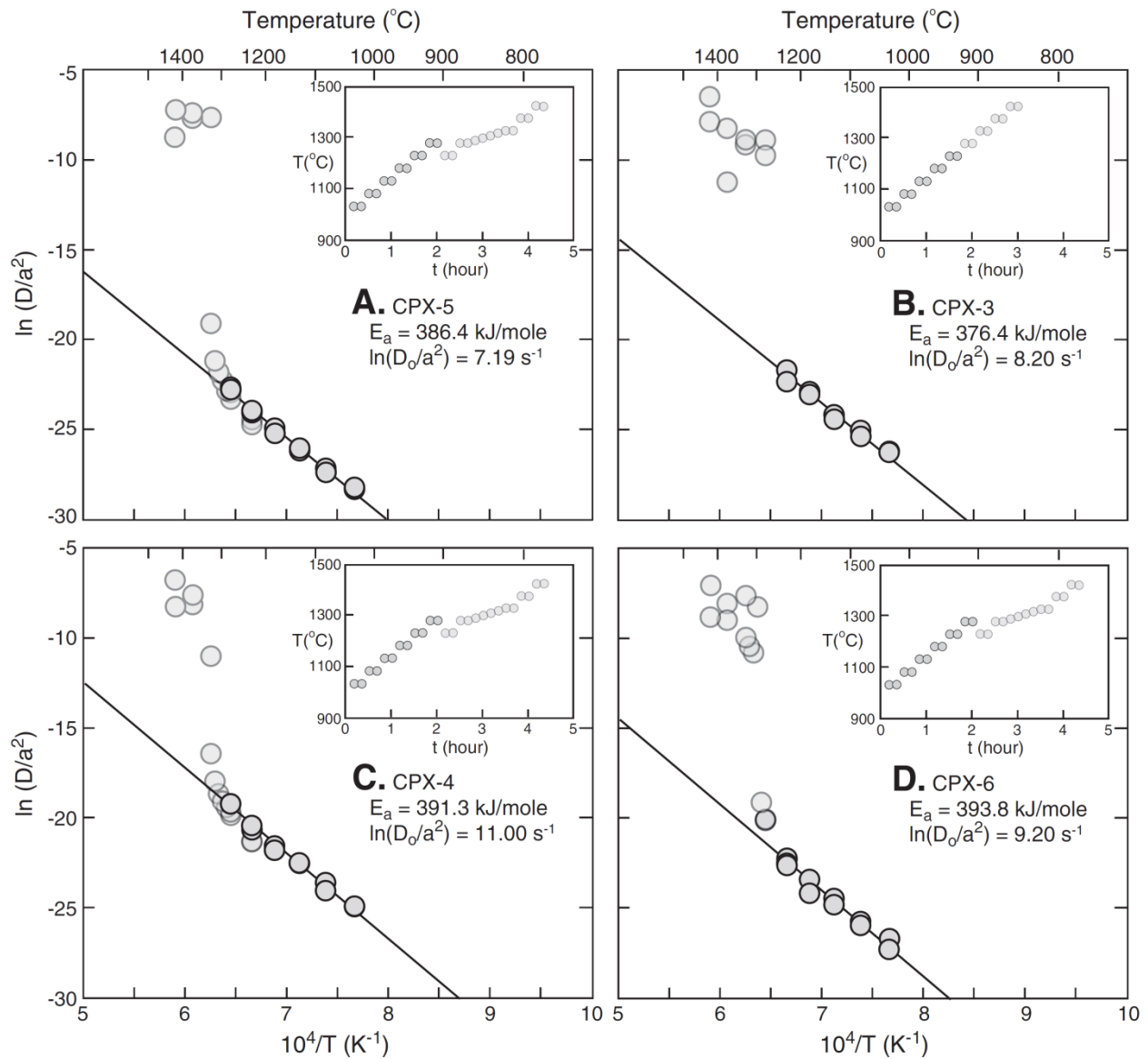
Figure 25 – Arrhenius plots for different CPX crystals from Cassata et al (2011).
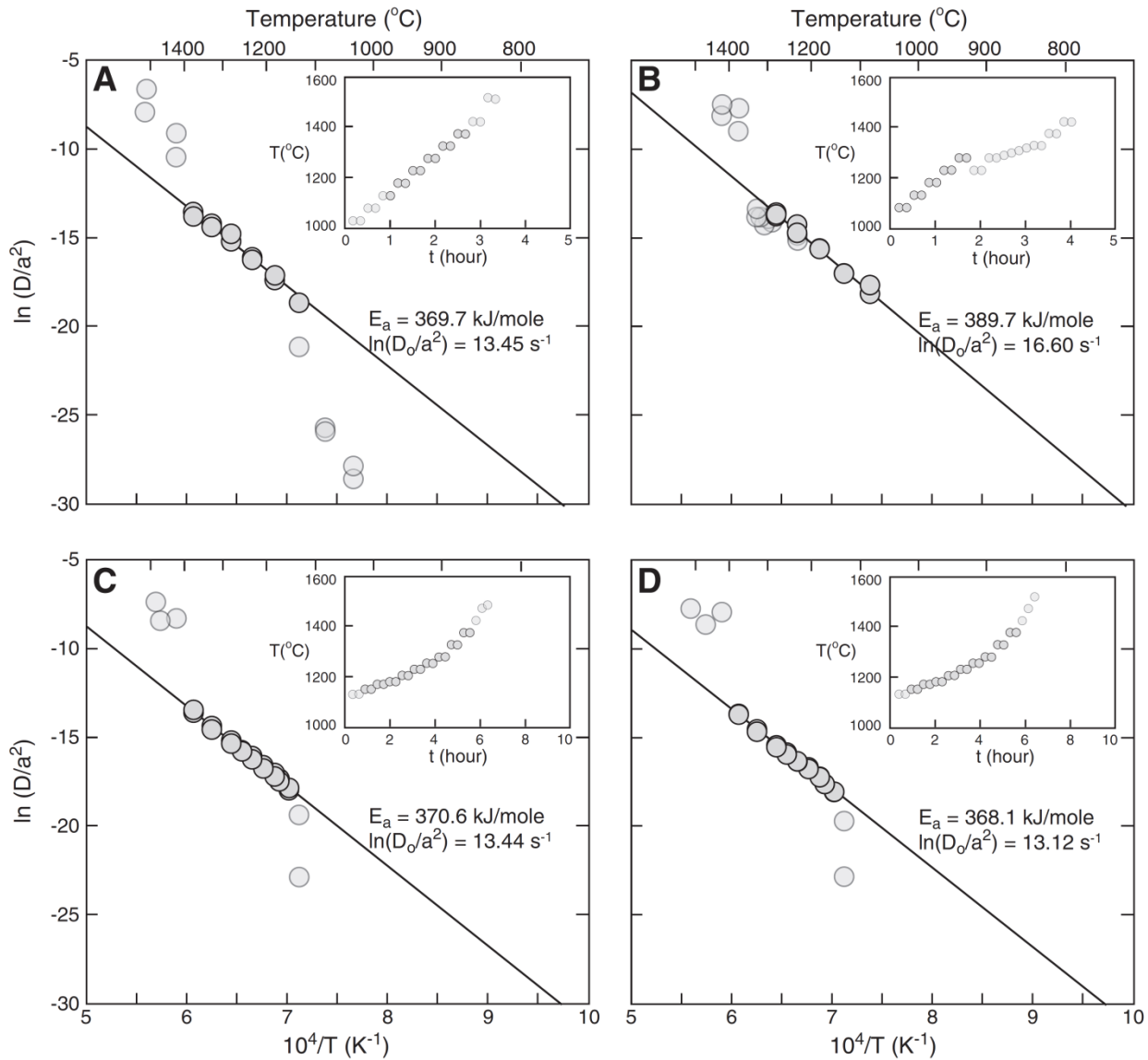
Figure 26 – Arrhenius plots for different OPX crystals from Cassata et al. (2011).

II.3.4.3 Ar Diffusion in Basaltic Glass

Amalberti et al. (2016) undertook experimental studies to investigate the diffusion of He, Ne, and Ar in the CMAS (CaO-MgO-Al_2O_3-SiO_2) system over a broad temperature range (423-1198 K) to cover diffusion in liquid-glass transitions. The authors used two different synthetic glass samples for comparison (compositions shown in Table 2).

Table 2 – Compositions of synthetic basaltic glasses G1 and G2 used in the experiments of Amalberti et al (2016) and their melt-glass transition temperatures (T_g).

	SiO_2	Al_2O_3	MgO	CaO	T_g
G1	50%	9%	16%	25%	1005 K
G2	64.6%	15.9%	8%	11.5%	1080 K

They reported results in terms of activation energy. An Ea ~350 kJ/mol was determined for Ar in basaltic glass G1. This value was considered too high by the authors, and the reasons for the possible error are unknown. For G2, the authors defined an Ea = 64.5 kJ/mol between 723 and 898 K; Ea = 166 kJ/mol for temperatures >898 K.

The low-temperature Ar diffusion data (1003< T< 1040 K) shown in Figure 27 suggests that isotopic fractionation is temperature-dependent: $D^{40}Ar/D^{36}Ar$ decreased intensively with decreasing temperature, from near 1 at T>1040K to 0.76 close to T_g (1003 K).
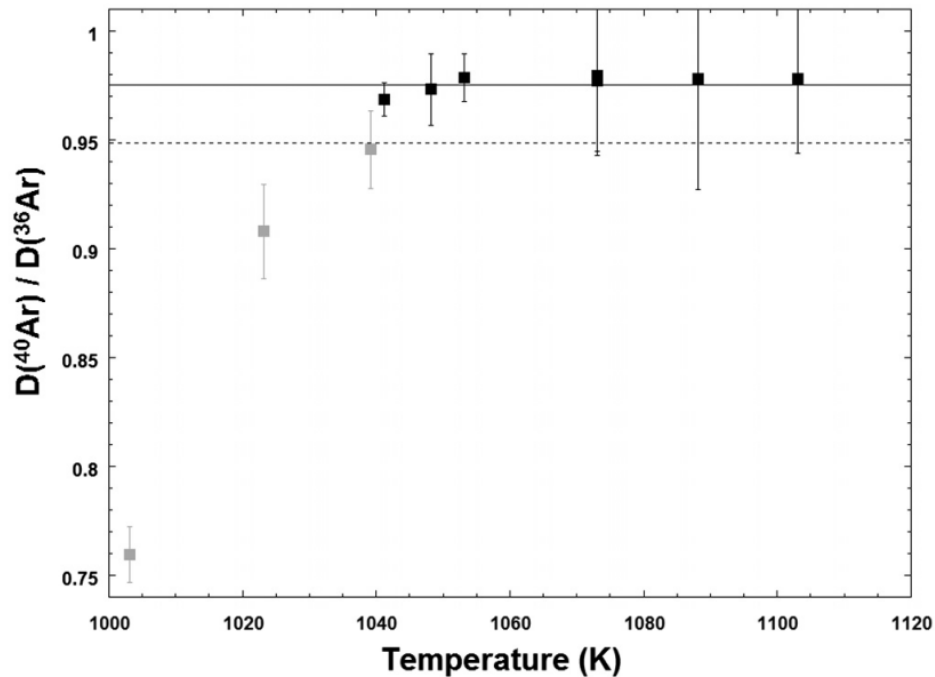
Figure 27 – $^{40}Ar/^{36}Ar$ ratio in glass G1 as a function of temperature. The dashed line corresponds to Graham's law: $D(^{40}Ar)/D(^{36}Ar) = 0.95$. The solid line corresponds to the average value of the high-temperature data (solid symbols: T > 1040K): $D(^{40}Ar)/D(^{36}Ar) \sim 0.98$.

II.3.4.4 Ar Diffusion in Basaltic Melts

Amalberti et al. (2018) conducted Ar diffusion experiments to determine the diffusion coefficient of Ar at 1673 K in a synthetic basaltic liquid with composition G1 (Table 2). The authors found $D_{ar} = 9.3$ x 10^{-7} $cm^2.s^{-1}$ at atmospheric pressure. Nowak et al. (2004) reported Ar diffusivities (experiments at 500 MPa) in Hawaiitic melts (relatively similar to G1 composition) for temperatures ranging from 1623 K (D = 2.8 x 10^{-7} $cm^2.s^{-1}$) to 1773K (D = 1.6 x 10^{-6} $cm^2.s^{-1}$). Lux (1987) measured Ar diffusivity in a natural tholeiite melt at 1623 K, finding $D_{ar} = 6.5$ x 10^{-6} $cm^2.s^{-1}$. Figure 28 shows these values plotted on a LogD vs 1/T graph.
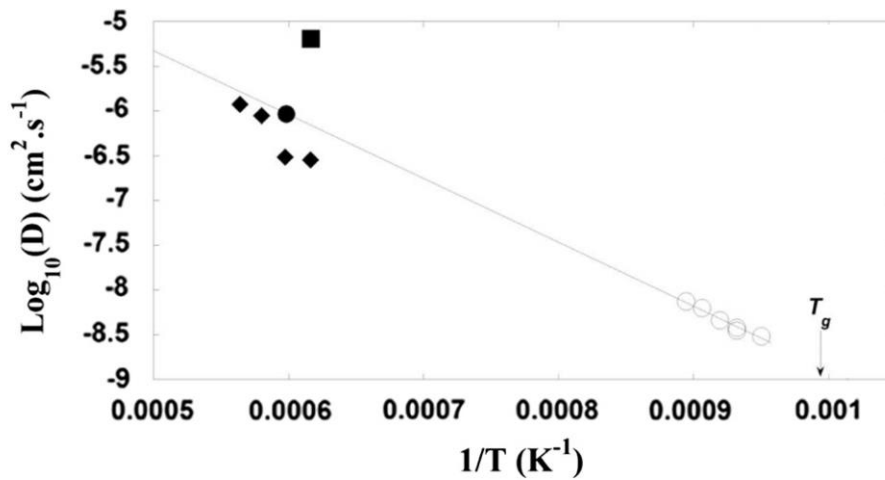
Figure 28 – Arrhenius diagram for Ar diffusion in basaltic melts (Amalberti et al., 2018, see references therein for sources). Black circles correspond to diffusion coefficients measured in G1 glass at high temperatures from Amalberti et al. (2018); white circles correspond to lower temperature diffusion coefficients in basaltic glass measured by Amalberti et al. (2016). Solid diamonds are for Hawaiitic melt. Solid black squares are for a natural tholeiite melt. T_g is the glass-melt transition temperature (1005 K).

For the activation energies, Nowak et al. (2004) reported $E_a = 257$ kJ.mol^{-1} for Ar in synthetic Hawaiitic melts at 500 MPa and 1623-1773 K. For a similar melt composition, Carroll (1991) reported $E_a = 144$ kJ.mol^{-1} at 128-373 MPa and 773-1773 K. Hazelton et al. (2003) reported $E_a = 130$ kJ.mol^{-1} for Ar in a natural alkali basalt at 0.1 MPa and T > 1250 K. Amalberti et al. (2018) report $E_a = 136.5$ kJ.mol^{-1} at 0.1 MPa and 1673 K. Differences in E_a values are likely attributed to differences in composition and pressure between the experiments (Amalberti et al., 2018). Hazelton et al. (2003) and Amalberti et al. (2018) show very similar results, indicating that melt structure, as measured by the parameter of non-bridging oxygen/silica

tetrahedrally coordinated cation (NBO/T), plays a major role on Ar diffusion parameters since the materials used in both studies had similar NBO/T values.

CHAPTER III – MATERIALS AND METHODS

Most of this work was carried out in experimental and analytical laboratories in addition to office hours to analyze and report the data generated. These processes are described ahead.

III.1 Experiments

All experiments, including sample preparations, were performed at the Laboratory of Experimental Petrology and Geochemistry at the Institute of Geosciences (IGc), University of Sao Paulo (USP).

The experimental set-up for this research followed a simple logic: increase Ar concentration within our samples to create a chemical potential; submit these samples to Venusian surface temperatures; measure the changes of Ar concentration in samples through time; calculate diffusion coefficients based on the latter. Thus, the experiments were divided into three steps: (1) testing Ar injection into samples (rock or glass); (2) generating Ar saturated microgabbro beads; and (3) submitting these beads to Venusian surface temperatures during different time intervals. All steps were performed in atmospheric pressure (~1 atm) using two different furnace apparatuses.

The GERO HTRV 70-250/18 vertical tubular furnace with drop-quench mechanism (VTF; Figure 29) was used in all steps. This furnace is attached to an AALBORG gas-mixing controller and a type-B thermocouple ($Pt_{94}Rh_6$-$Pt_{70}Rh_{30}$) connected to a Eurotherm 3508 thermal controller for gas flow and temperature monitoring, respectively (details in Mallmann et al., 2014). Three temperature calibration operations were performed during this research following the procedures from Mallmann et al. (2014). Temperatures recorded on the hot zones were 1205ºC, 1204ºC, and 1202ºC for the calibrations done in January 2019, June 2019, and October 2020, respectively (Figure 30). Since the zirconia electrolyte (SIRO2-C700) was inserted at a precise temperature of 1200ºC, this means that temperature readings were 5ºC, 4ºC, and 2ºC higher than the actual temperature inside the furnace during the three calibrations respectively. These differences were corrected, so the temperature values in this report are accurate. The hot zone is defined by the region where temperature uncertainty is <1ºC.

A JUNG J200 muffle furnace (MF) was also used. This furnace has a temperature uncertainty of 10ºC and has ambient atmospheric composition.

Liquidus and *solidus* temperatures (1143ºC and 940ºC, respectively) for the starting sample (IC09) were calculated using the software Rhyolite-MELTS (version 1.02, Gualda et al., 2012).
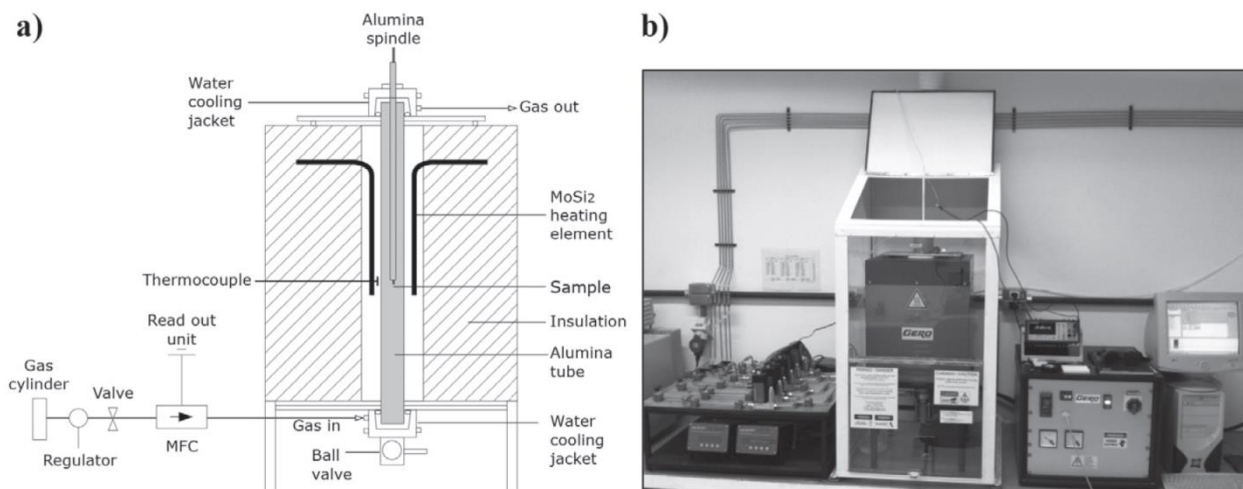
Figure 29 – Schematic drawing (a) and photograph (b) of the VTF extracted from Mallmann (2014).
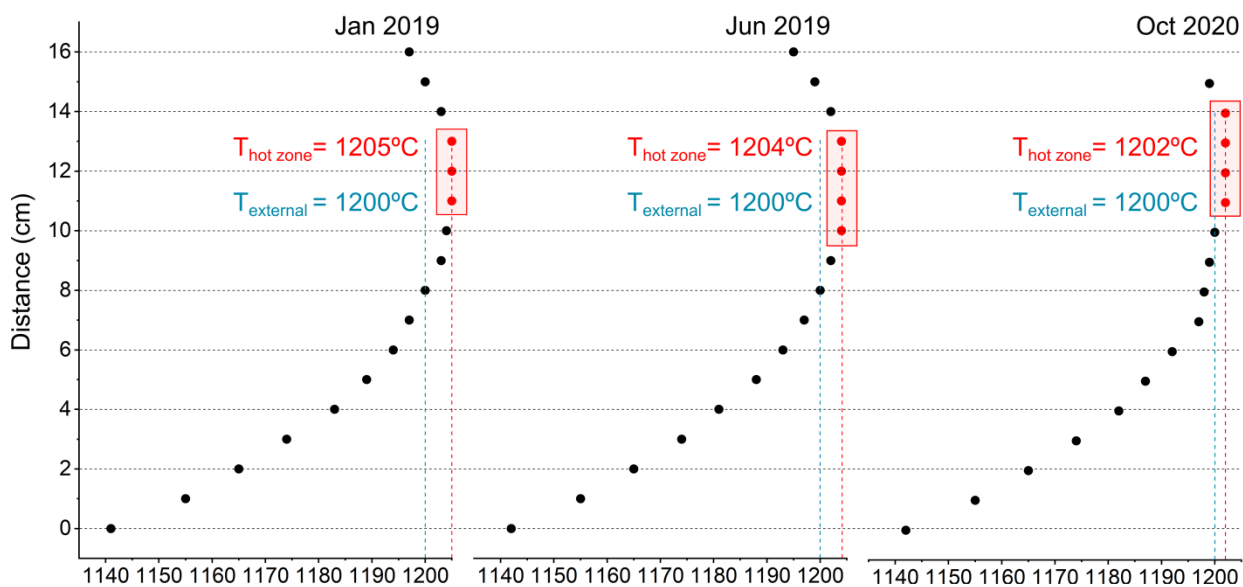
Figure 30 – Temperature profiles during calibration showing the hot zone within the furnace. Distance zero refers to the sample holder's maximum reach inside the furnace. Hot zones are highlighted in red boxes. $T_{hot\ zone}$ and $T_{external}$ refer to the temperature readings and the actual temperatures in the hot zone, respectively.

III.1.1 Starting material

Fe/Mg, Mg/Mn, K/U, and U/Th ratios suggest that Venusian basalts are the product of similar degrees of partial mantle melting as those on Earth (Treiman, 2007). Additionally, the only *in-situ* major elements' data from the surface rocks of Venus are those from the Venera 13, Venera 14, and Vega 2 missions, which indicate tholeiitic basaltic compositions (Bougher et al., 1997). For these reasons, the starting material used in this work (IC09) is a tholeiitic basalt from the Limeira Intrusion, SE Brazil, which was already in possession of our research group (e.g. Lino, 2015; Carvalho, 2020; Lino and Vlach, 2021).

These rocks are part of the Parana Magmatic Province, the South American counterpart of the Parana-Etendeka Large Igneous Province. In this context, the Limeira Intrusion is a lopolithic to wedge-shaped body comprising many rock-types (from basalts to coarse-grained melagranodiorites) associated with a continental-scale extension which culminated on the opening of the South Atlantic Ocean during the Lower Cretaceous (e.g. Milani, 1992; Ernesto et al., 1999; Janasi et al., 2011; Lino and Vlach, 2021).

Hand-sized rock samples were crushed using a mechanical press (< 200 mesh powder), succeeded by an additional crush using agate elements to minimize grain size. This was done to facilitate sample melting and homogenization for the following experiments.

The starting material's composition was determined by Carvalho (2020) through x-ray fluorescence. Table 3 shows the compositions of the starting material and of the Venusian surface rocks for comparison. The mg# ($100*MgO/(MgO + FeO^T)$) was calculated for the starting material and the Venusian rocks, however, due to very large uncertainties, the latter is ignorable. The CIPW norm obtained from Carvalho (2020) is also shown in Table 3. The CIPW norm for the Venusian rocks is not shown because data inaccuracy makes it impractical.

Table 3 – Major elements compositions (obtained through XRF), CIPW norm, and mg# of the starting sample IC09 (data from Carvalho, 2020) and Venus' surface rocks obtained by the Venera 13, Venera 14, and Vega 2 missions (data from Treiman, 2007; see references therein for original sources). CIPW norm for the Venusian rocks is not shown due to data uncertainty.

	IC09	Venera 13	Venera 14	Vega 2
Composition (wt% oxide)				
SiO_2	48.63	45.1 ± 6	48.7 ± 7.2	45.6 ± 6.4
TiO_2	4	1.6 ± 0.9	1.25 ± 0.8	0.2 ± 0.2
Al_2O_3	12.92	15.8 ± 6	17.9 ± 5.2	16 ± 3.6
FeO	14.2	9.3 ± 4.4	8.8 ± 3.6	7.7 ± 2.2
MnO	0.23	0.2 ± 0.2	0.16 ± 0.16	0.14 ± 0.24
MgO	4.4	11.4 ± 12.4	8.1 ± 6.6	11.5 ± 7.4
CaO	8.67	7.1 ± 2	10.3 ± 2.4	7.5 ± 1.4
Na_2O	2.77	-	-	-
K_2O	1.06	4 ± 1.2	0.2 ± 0.14	0.1 ± 0.16
SO_3	-	1.6 ± 2	0.35 ± 0.6	1.9 ± 1.2
Total	96.88	96.1 ± 35.1	95.8 ± 26.7	90.6 ± 22.8
mg#	36	69 ± 136	62 ± 92	73 ± 86
CIPW norm (wt%)				
Quartz	6.09	-	-	-
Orthoclase	6.56	-	-	-
Albite	25.72	-	-	-
Anorthite	20.21	-	-	-
Diopside	15.03	-	-	-
Hypersthene	12.78	-	-	-
Magnetite	3.22	-	-	-
Ilmenite	5.62	-	-	-
Apatite	1.39	-	-	-
Total	96.62			

III.1.2 Experimental test: Ar injection in glass and microgabbro beads

In many diffusion experiments authors use pressure apparatuses to enhance noble gas incorporation into their samples (e.g. Koepke and Behrens, 2001; Amalberti et al., 2016, 2018). Here, we used a *superliquidus* temperature (1200ºC) combined with the 100% Ar atmosphere to make our melt Ar saturated at atmospheric pressure, a procedure very similar to that of Marrocchi and Toplis (2005).

This initial step was taken to check if we would be able to saturate our samples with Ar using this technique and to compare differences in Ar content between a glass sample and its crystallized replicate (microgabbro).

The starting material powder was mixed with polyethylene gel to produce two highly viscous ~5 mm spheres. These spheres were mounted onto Pt-Rh (70Pt30Rh) wires using the wire-loop technique (e.g. Corrigan and Gibb, 1979; Figure 31a). They rested for 24h hours at room temperature for drying.

These assemblages were then mounted onto a Pt-Rh wire hanger (Figure 31b) and inserted into the furnace hot zone, which was on standby at 650ºC. The furnace temperature was set to increase at a tax of 300ºC/h, while Ar flux was set at 10 x 400 (4000 cm³/min). After 1.5h, the system reached 1200ºC (57ºC above *liquidus* temperature) and remained in these conditions for 4 hours to completely melt the solution. At this point, one of the aliquots was dropped and quenched into a vial containing pure water to form a single Ar-saturated basaltic glass bead. The other sample stayed in the furnace and a 2.5ºC/h cooling rate combined with a 50 x 10 (500 cm³/min) Ar flux was set to promote crystallization under Ar-saturated conditions. Initial Ar flux was reduced because the furnace was already fully saturated with Ar. After 140h, the system reached 850ºC (90ºC below *solidus* temperature), when all phases should have crystallized and the remaining sample was quenched, generating an Ar-saturated microgabbro bead. All these procedures were done at atmospheric pressure, different from most diffusion experiments where samples are annealed to add the diffusant into the samples. We expected that even at low pressures, full Ar saturation in the chamber and high temperature would be enough to dope our samples with the gas.

By the end of this step, we had 1 basaltic glass bead (IC09-GL) and 1 microgabbro bead (IC09-MG; Figure 32). To check if we were able to insert Ar into the aliquots, these were

analyzed through mass spectrometry (step-heating technique). The starting material (IC09) was also analyzed for comparison (results shown in next chapter).
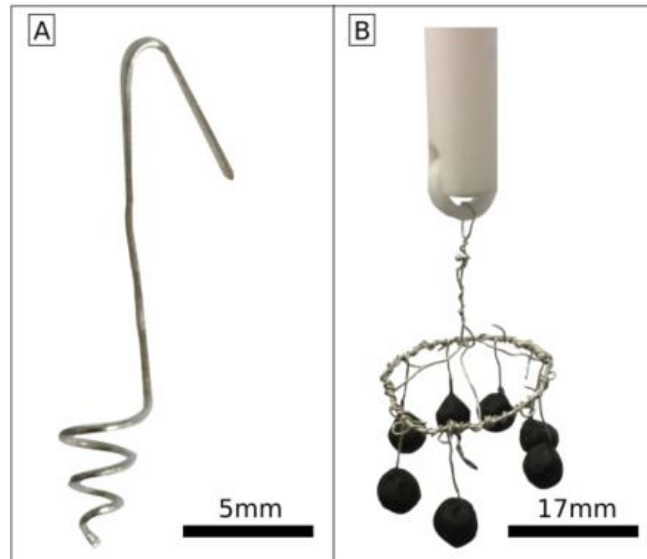
Figure 31 – A- Pt-Rh wire shape for the wire-loop technique; B - IC-09 powder combined with polyethylene gel mounted onto Pt-Rh wires and wire hanger. PS: only two beads were inserted into the furnace during test experiments.

Figure 32 – Glass (left) and microgabbro (right) beads seen through a magnifying glass.

III.1.3 Generation of Ar-saturated microgabbro beads

After verifying the successfulness of the test experiments, multiple Ar-saturated microgabbro beads were generated following the same procedure. There was a change in initial Ar flux from 4000 cm³/min (as in the test experiments) to 1900 cm³/min to minimize the number

of bubbles in the samples, as was observed on the aliquots of the test experiments. Experimental conditions are illustrated in Figure 33.

The technique used allows the loading of 8 beads into the furnace per batch. Here, we did two batches containing 5 aliquots each, for a total of 10 Ar-saturated microgabbro beads like the one shown in Figure 34.
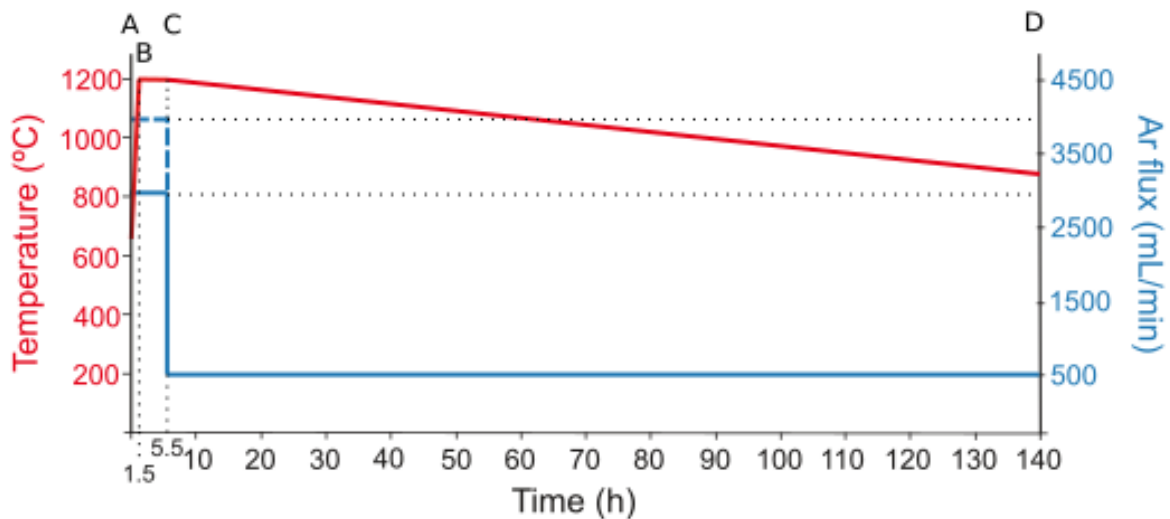
Figure 33 – Experimental conditions for the generation of Ar saturated microgabbro beads in the VTF. The temperature is shown in red (left) and Ar flux in blue (right). The dashed blue line relates to the test experiments' initial Ar flux (4000 cm³/min). Final experiments' conditions are represented by the solid blue line (initial Ar flux = 2900 cm³/min). From A to B, increasing temperature rate was set at 300°C/h. From B to C, the temperature remained constant. The glass bead was quenched at C. From C to D, decreasing temperature rate at 2.5°C/h. Microgabbro beads were quenched at D.

Figure 34 – Pictures of one of the microgabbro beads. Attached to the Pt wire (left); inner half (middle); outer half (right).

III.1.4 Exposition of beads to Venusian surface temperatures

This step was done using the vertical tubular furnace (VTF) and the muffle furnace (MF) simultaneously to compare the effects of atmospheric composition on diffusivity. Four microgabbro beads were inserted into each of the furnaces which had their temperatures set at 460ºC, corresponding to the Venusian average surface temperature.

VTF had a CO_2 flux of 50 x 200 (1000 cm³/min) during the first two hours of the experiment to saturate the inside of the furnace with the gas. Afterward, CO_2 saturation was decreased to 10 x 200 (2000 cm³/min) to maintain CO_2 saturation conditions. Experiments in the MF were held under ambient atmospheric composition. Thus, the VTF represented a CO_2-dominated atmosphere (similar to Venus) and the MF a terrestrial atmosphere.

After the experiments started, one bead from each furnace was removed after 2, 4, 8, and 16 days. In the end, we had 1 bead corresponding to each of these intervals inside each of the furnaces, in addition to 2 beads which did not go back into the furnace so that we could measure the initial Ar content in the beads before they were exposed to Venusian conditions, for a total of 10 microgabbro beads. This characterizes a desorption experiment, in which a rocky material initially containing a volatile of interest is heated in a medium that is devoid of that volatile, so it will diffuse outwards (Zhang, 2010).

III.2 Analyses of the Experimental Products

The analytical part involved noble gas spectrometry to investigate variations in Ar content on the samples, and an electron microprobe to characterize the experimental products. Results are shown in the next chapter.

III.2.1 Noble gas spectrometry

Ar analyses were done through step-heating using a multi-collector Thermo Scientific ARGUS VI mass spectrometer at the Noble Gas Geochronology Laboratory, CPGeo - University of Sao Paulo.

Measurements were made on the rim and core of each bead. To collect material from both, the beads were gently broken in half with a hand press. Using a magnifying glass, loose parts from the core or rim were separated and weighted employing a high precision scale (error within 10^{-7}g). High Ar content was expected, so very small parts of the samples were needed (~0.2 mg) to produce signals within the sensors' limits and record values with maximum precision. In the case of the starting material, a random particle of the crushed sample powder was used. These were loaded onto a copper disk and inserted into the spectrometer for the analyses.

In this method, samples are individually heated in steps under ultra-high vacuum using a continuous laser beam as the heat source. Temperature is increased on each step and the released Ar is detected on each of the 5 collectors of the mass spectrometer simultaneously, which enables high precision measurements. Each laser shot results in a signal peak. Peaks' heights, given by the distance between top and base signal lines (in fA), are obtained through minimum-quadratics. This process is repeated until there is no detectable Ar left in the sample and/or when the sample melts. Blank measurements are made intermittently with the heating steps to account for instrumental background. After a series of mathematical treatments, including the removal of blank values and the comparison with a previously known Ar mass (air pipette), signals (in fA) from all heating steps are added together and converted to mass. This enables the calculation of the ^{36}Ar, ^{38}Ar, and ^{40}Ar masses released from each sample. Ar concentration (in ppb) is then obtained by dividing the Ar mass by the sample mass. All these calculations were done using python language in the web-based interacting computing platform Jupyter Notebook.

Analytical errors are calculated using the python MetroloPy package (https://nrc-cnrc.github.io/MetroloPy/_build/html/index.html) based on instrumental uncertainties implicitly obtained in each of the processes mentioned above.

III.2.2 Electron microprobe analyses

Backscatter electron (BSE) images and wavelength dispersive spectrometry (WDS) analyses of the experimental products were obtained with the JEOL JXA-FE-8530 electron microprobe (EMP), provided with a field emission gun and five wavelength dispersive spectrometers, to characterize the main textures and compositional features of the glass and mineral phases on the microgabbro. Aliquots of the test experiments (IC09-GL and IC09-MG for the glass and microgabbro, respectively) were used for these analyses.

The analyses was done under 12 kV and 10 nA for the column accelerating voltage and beam current, respectively, and variable beam diameter (minimum for the BSE images and between 1 and 5 um for quantitative analyses, see details in Carvalho, 2020). Glass and natural minerals from the Smithsonian Institute were used as standards. The matrix effects were corrected with the PRZ-Armstrong software provided by JEOL.

CHAPTER IV – RESULTS

This chapter presents the results obtained from the analyses of experimental products and the calculation of diffusion coefficients.

IV.1 Textures and Compositions of the Experimental Aliquots

Representative BSE images of the microgabbro (sample IC09-MG) and glass (sample IC09-GL) are shown in Figure 35.

The microgabbro is fairly homogeneous, with plagioclase being the most abundant phase (~50% volume), followed by pyroxene (~44% volume) and Ti-magnetite (~6% volume). These phases are easily dinstinguishable in these images due to their different average atomic numbers that result in different brightnesses (brightness increases with increasing atomic number). Plagioclase crystals are difficult to individualize (anhedral). Pyroxene (diopside/augite) crystals are mostly prismatic with subhedral to euhedral textures and lengths of 10 to 100 μm (long axis). Ti-magnetite crystals are subhedral to euhedral and 5-20 μm long.

Sample IC09-GL is also homogeneous. Unexpectedly, diminute Ti-magnetite crystals are homogeneously distributed in the glass, occupying ~3% of the sample's volume. These crystals are subhedral and have an average length of ~5 μm. The presence of vesicles is also noted in the glass aliquot.

Vesicles occur in all products and are more abundant in the glass sample (e.g. Figure 35g) in comparison to the microgabbro (e.g. Figure 35a). However, vesicle population is not homogeneous throughout the samples, so that unnanalized portions of the aliquots could also host concentrated vesicles.

The mean compositions of the glass, plagioclase, pyroxene, and magnetite crystals obtained through WDS point analyses are given in Table 4 (whole data on Appendix 1). The plagioclase crystals correspond to labradorite (average $An_{60}Ab_{39}Or_1$), while the clinopyroxenes are diopside and augite (average $Wo_{44}En_{43}Fs_{13}$). These compositions are similar to those obtained by Carvalho (2020) in crystallization experiments using the same starting material (IC09).
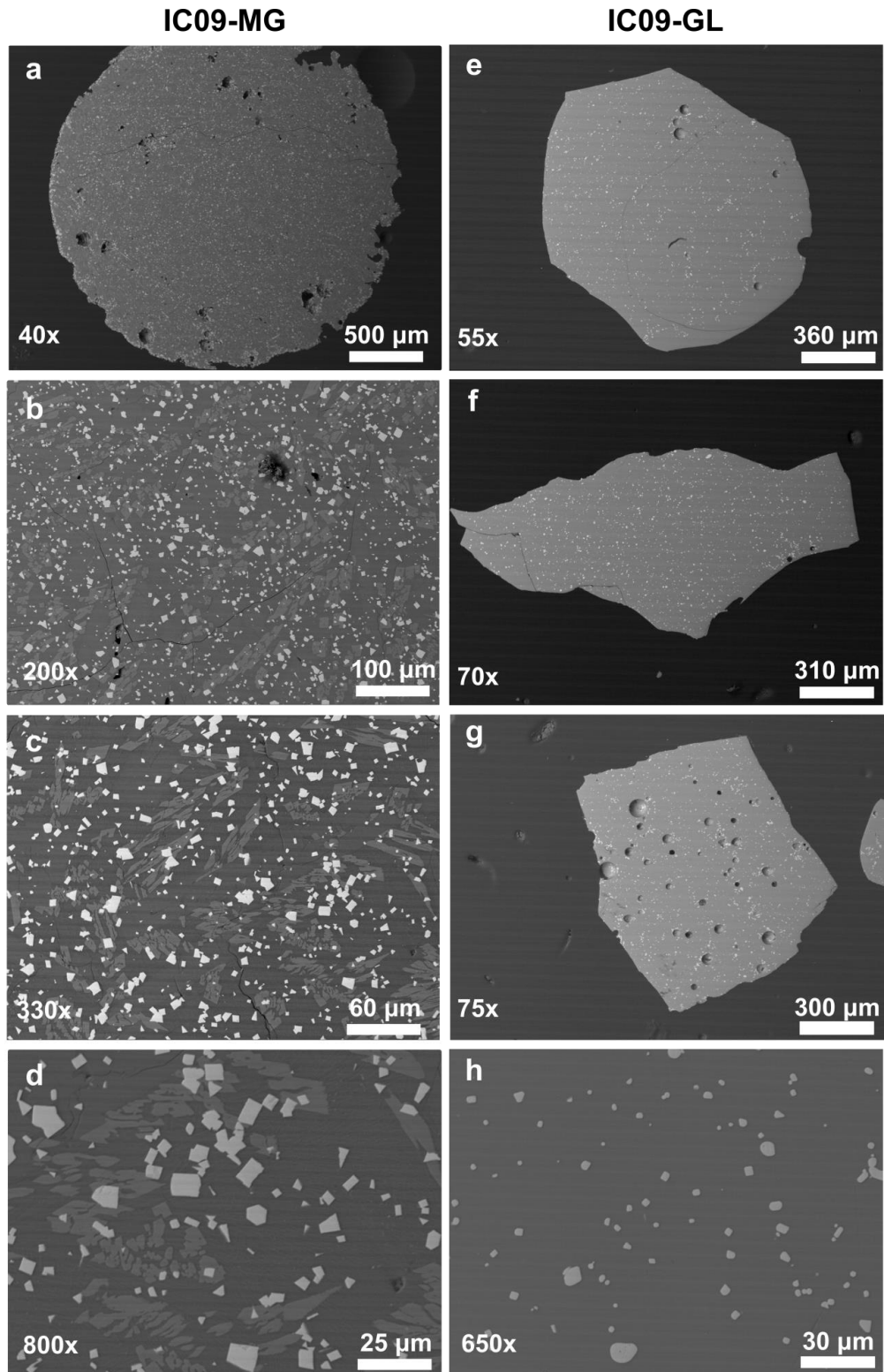
Figure 35 – Representative BSE images for the synthetic microgabbro (sample IC09-MG) and glass (sample IC09-GL) in different scales. The left column refers to the microgabbro (a, b, c, d) and the right column to the glass (e, f, g, h). Plagioclase crystals are shown in dark gray; clinopyroxenes in gray; oxides (mainly magnetite) are shown in light gray/white.

Table 4 – Average composition (wt.%) obtained by WDS point analyses of experimental products (see whole data in Appendix 1). Pyroxene and plagioclase are from sample IC09-MG; glass corresponds to sample ICO9-GL; magnetite refers to crystals from both samples.

	Pyroxene	Plagioclase	Magnetite	Glass
SiO_2	46.4	52.54	0.21	51.55
TiO_2	2.13	0.20	14.27	2.96
$ZrO3$	-	-	-	0.11
Al_2O_3	5.50	26.99	1.68	13.61
Cr_2O_3	0.04	0.00	0.40	-
FeO^T	7.24	3.04*	67.73	10.09
MnO	0.30	0.01	0.56	0.22
MgO	14.53	0.37	5.61	4.67
ZnO	-	-	0.06	-
NiO	-	-	0.02	-
CaO	20.61	11.55	0.26	8.56
Na_2O	0.56	4.18	0.02	3.04
K_2O	0.04	0.21	-	1.11
Nb_2O_5	-	-	0.01	-
P_2O_5	-	-	-	0.60
Total	97.34	99.08	90.82	96.52

* Normalized to $Fe_2O_3^T$

IV.2 Ar Spectrometry Data: Microgabbro *vs*. Glass Beads (test experiments)

All Ar spectrometry results are summarized on Table 5. The test experiments' analyses reveal that Ar was successfully added into the samples (Figure 36). The glass bead (IC09-GL) recorded values of 9232 ± 387 ppb and 10974 ± 691 ppb of Ar in its core and rim, respectively, which represents the initial Ar concentration in a 'frozen basaltic liquid'. The microgabbro bead (IC09-MG) has 122 ± 8 ppb and 146 ppb ± 5 of Ar in its core and rim, respectively. For comparison, the random piece of starting material (IC09) has 9.00 ± 0.07 ppb of Ar. The step-heating profile (Figure 37) shows very different behaviors for the Ar released from the microgabbro and glass beads. A more homogeneous Ar-loss is observed on the microgabbro, while isolated peaks of Ar are detected on the glass product.

Higher Ar concentration on the rim of the beads was expected since this portion of samples was in direct contact with Ar inside the VTF. The ratios of Ar concentrations on the rim

over the core (Ar_{rim}/Ar_{core}) in both the glass (10974 ppb/9232 ppb) and microgabbro (146 ppb/122 ppb) are very similar (~1.20).

Table 5 – Summarized Ar spectrometry data. Ar concentration is given in ppb (Ar mass / sample mass).

Sample	Ar (ppb)
Starting material	
IC09	9.08 ± 0.07
Test experiments	
IC09-GL-C	9232 ± 387
IC09-GL-R	10975 ± 690
IC09-MG-C	122 ± 8
IC09-MG-R	146 ± 5
Initial conditions	
IC09-00.1C	59 ± 5
IC09-00.2C	89 ± 6
IC09-00.1R	128 ± 5
IC09-00.2R	122 ± 6
Muffle furnace - core	
IC09-MF-02C	80 ± 3
IC09-MF-04C	46 ± 2
IC09-MF-08C	27 ± 1
IC09-MF-16C	15.08 ± 0.4
Muffle furnace - rim	
IC09-MF-02R	64 ± 6
IC09-MF-04R	30 ± 2
IC09-MF-08R	35 ± 4
IC09-MF-16R	39 ± 2
Vertical tubular funace - core	
IC09-VTF-02C	57 ± 1
IC09-VTF-04C	150 ± 5
IC09-VTF-08C	24 ± 1
IC09-VTF-16C	14.8 ± 0.3
Vertical tubular furnace - rim	
IC09-VTF-02R	56 ± 2
IC09-VTF-04R	57 ± 3
IC09-VTF-08.1R	290 ± 14
IC09-VTF-08.2R	128 ± 4
IC09-VTF-16R	20 ± 1
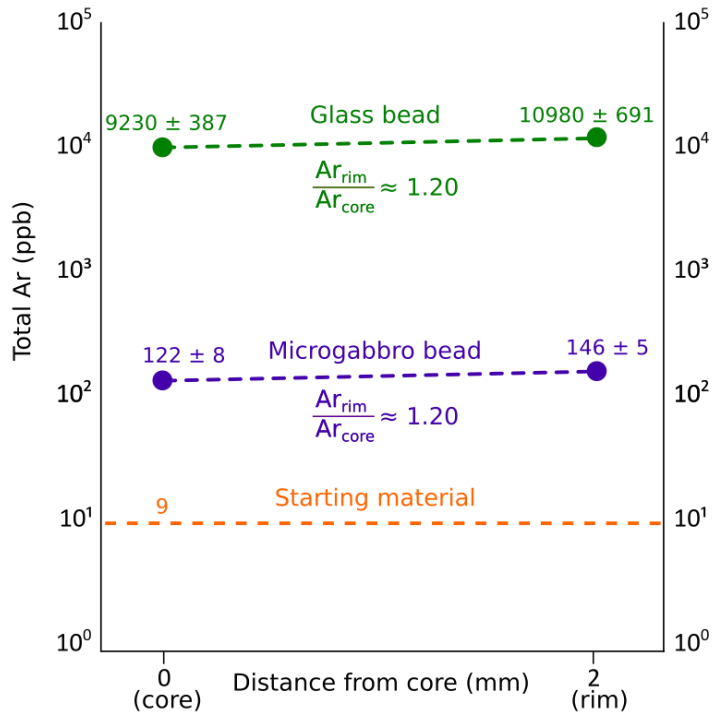
Figure 36 – Ar spectrometry data from test experiments in ppb showing that Ar was successfully incorporated into samples. The starting material (IC09), in orange, has much less Ar than the experimental products. Ar content on the glass bead (IC09-GL), in green, is ~10 times greater than on the microgabbro bead (IC09-MG), in purple. The Ar_{rim}/Ar_{core} ratios of the beads are virtually the same.
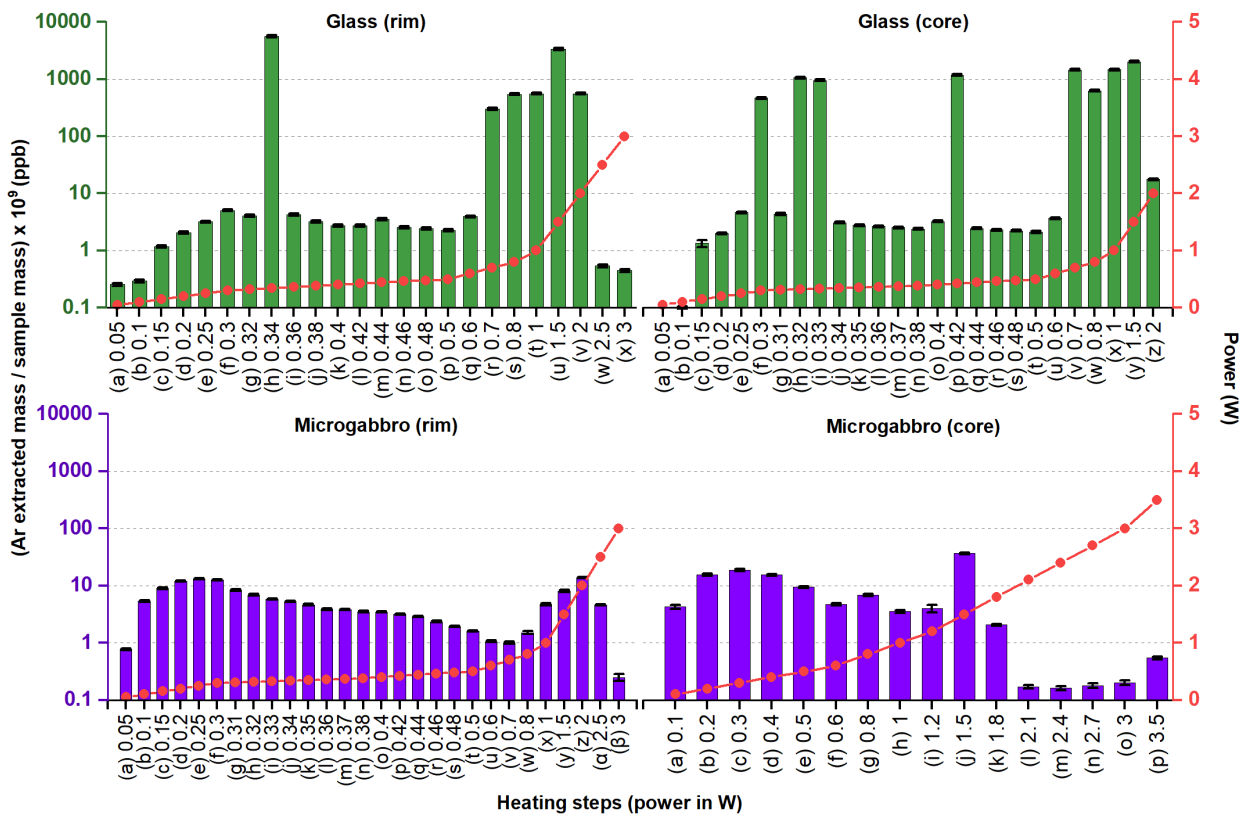
Figure 37 – Step-heating profiles for the glass (green) and microgabbro (purple) beads. Numbers on the left side indicate the amount of Ar released on each heating step (green and purple columns). The Ar mass is divided by the sample mass, giving values in ppb to facilitate the comparison between the two beads. Values on the right side (connected red dots) indicate the power of each heating step in W.

IV.3 Ar Spectrometry Data: Microgabbro under Venusian Surface Conditions

The Ar concentration profiles from experiments done on the muffle furnace (MF) and vertical tubular furnace (VTF) indicate a general Ar loss trend for all experiments (see Figure 38 and Table 5). In these profiles, day 0 refers to the initial conditions of the experiments (samples IC09-00.1 and IC09-00.2). Two analyses were done for the rim and core of these two replicates to check for data consistency. For this reason, day 0 data are the same in both graphs (59 ± 5 ppb and 89 ± 6 for the core; 128 ± 5 ppb and 122 ± 6 ppb for the rim). Here, there is a larger difference between rim and core values in comparison to the test experiments, probably caused by the change in Ar flux mentioned earlier.
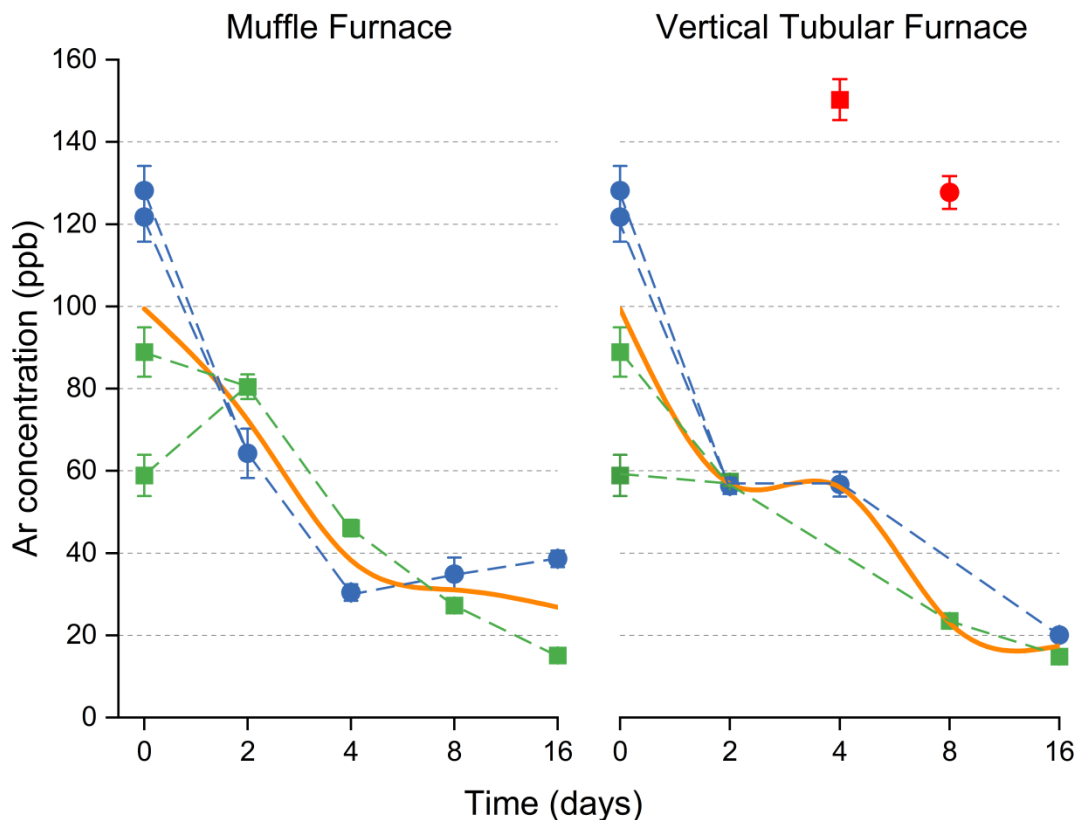
Figure 38 – Ar profiles from experiments done in the muffle furnace (left) and vertical tubular furnace (right). Rim and core measurements are represented by blue circles and green squares, respectively. Outliers are shown in red. The solid orange line represents the average value between rim and core measurements.

The core of the beads in the MF had a decrease in Ar content from day 0 to 16 (excluding the lower value from sample IC09-00.1C on day 0), as evidenced from samples IC09-MF-02C (80 ± 3 ppb), IC09-MF-04C (46 ± 2 ppb), IC09-MF-08C (27 ± 1 ppb), and IC09-MF-16C (15 ± 1 ppb).

The rims of the beads in the MF show a decrease in Ar content from day 0 to day 4, with concentrations of 64 ± 6 ppb and 30 ± 2 ppb in samples IC09-MF-02R and IC09-MF-04R, respectively. From day 4 to day 16, Ar concentration increased within the beads. Results from samples IC09-MF-08R (35 ± 4 ppb) and IC09-MF-16R (39 ± 2 ppb) can be considered a slight increase or constancy in Ar content from the 8th to the 16th day of the experiment.

Experiments held on the VTF had similar results. Samples IC09-VTF-02C and IC09-VTF-02R had very similar Ar content (57 ± 1 ppb and 56 ± 2 ppb, respectively). Samples IC09-VTF-04C (150 ± 5 ppb), IC09-VTF-08C (23.5 ± 0.7 ppb), IC09-VTF-16C (14.8 ± 0.3 ppb) show

that the VTF beads' core had a general decrease trend over the experimental period. Samples IC09-VTF-04R (57 ± 3 ppb), IC09-VTF-08R (128 ± 4), and IC09-VTF-16R (20 ± 1 ppb) show that the rims of the VTF beads had similar behavior. The high Ar peaks on samples IC09-VTF-04C and IC09-VTF-08R are considered outliers, possibly related to the local concentration of microvesicles in the samples.

The VTF and MF experiments had similar behaviors during the step-heating (Figures 39 and 40), except for samples IC09-VTF-04C and IC09-VTF-08R, where isolated peaks of Ar were detected. This behavior is similar to that of the glass bead (section IV.2).
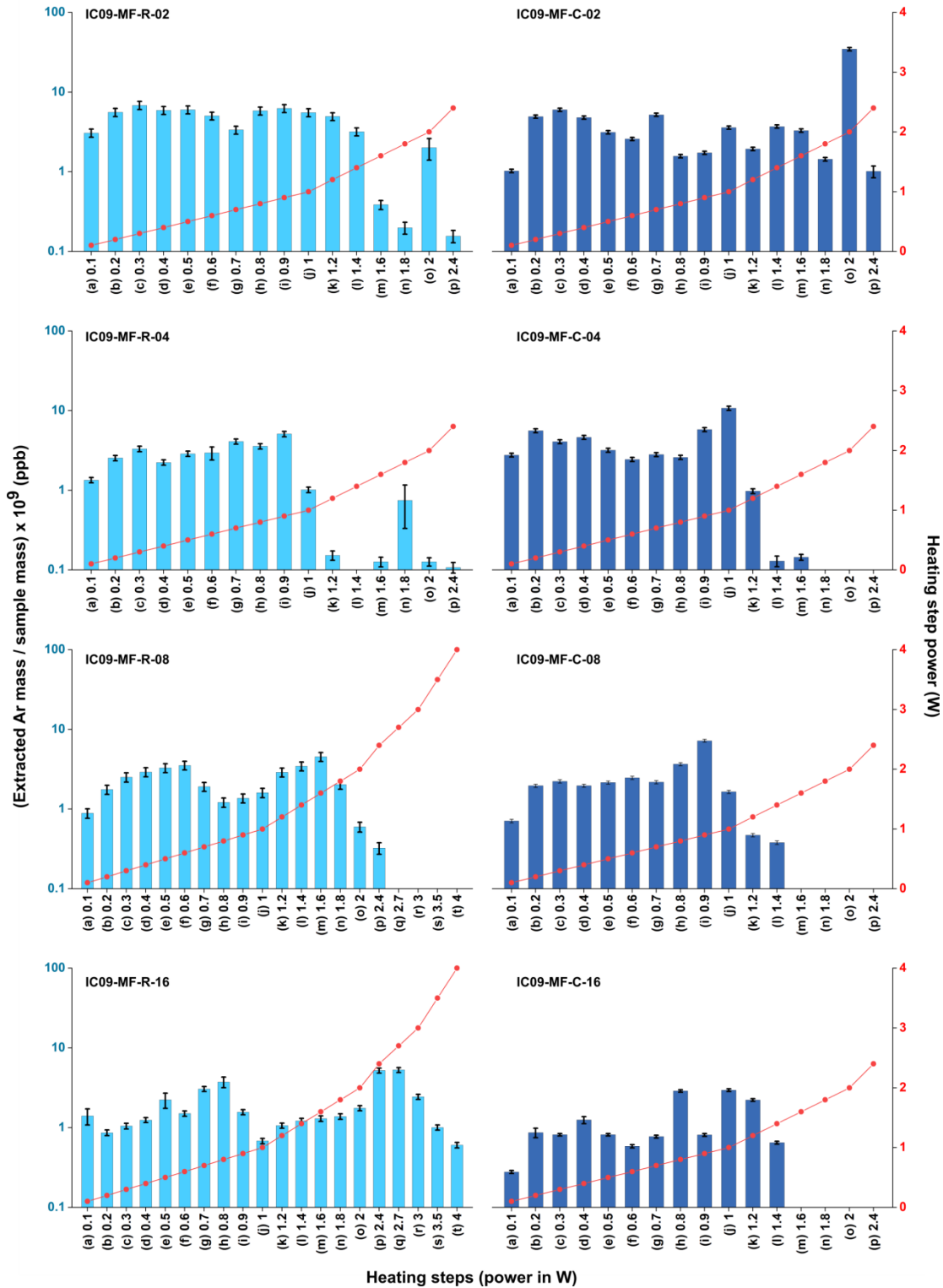
Figure 39 – Step-heating profiles for the experiments held on the Muffle Furnace (MF). Numbers on the left side indicate the amount of Ar released on each heating step (blue columns) in ppb. Values on the right side (connected red dots) indicate the power of each heating step in W.
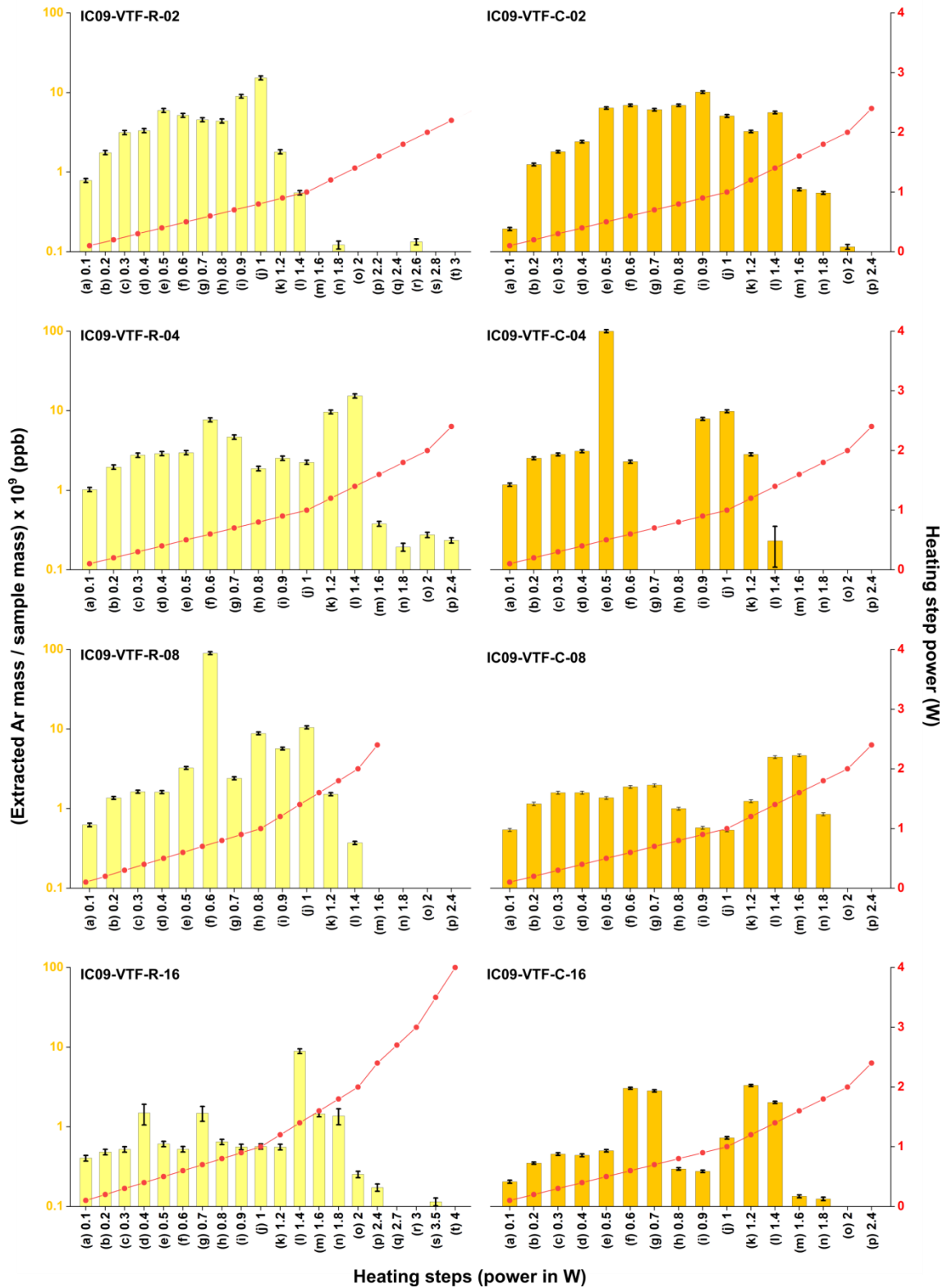
Figure 40 – Step-heating profiles for the experiments held on the vertical tubular furnace (VTF). Numbers on the left side indicate the amount of Ar released on each heating step (yellow columns) in ppb. Values on the right side (connected red dots) indicate the power of each heating step in W.

IV.4 Diffusion Coefficients

Two different approaches were used for determining diffusion coefficients using the software Origin 2020 (version 9.7.0.185, Academic) for calculations. The first, explained on section IV.4.1, considers the beads homogenous spheres losing Ar to the atmosphere during the experiments. The second (section IV.4.2.) addresses the Ar diffusion occurring in a semi-infinite medium, i.e. from cores to the rims of the beads.

IV.4.1 Diffusion from a homogeneous sphere into an infinite reservoir

According to Crank (1956), this solution can be used when the medium (in our case, microgabbro bead) is a sphere that is homogeneous in diffusant distribution, and the substance is diffusing into an infinite reservoir (in our case, the atmosphere). As depicted in Figure 38, Ar concentration in the beads became fairly homogeneous after day 2. Accordingly, this solution is suiTable for our data.

The fractional loss equation for spherical geometry (Crank, 1956) describes the diffusive mass loss in desorption experiments as follows:

$$\frac{M_t}{M_\infty} = 1 - \frac{6}{\pi^2} \sum_{n=1}^{\infty} \frac{1}{n^2} \, exp - \left(\frac{n^2 \pi^2 D t}{x^2} \right) \tag{9}$$

In cases where $M_t / M_\infty \leq 0.9$ (our case), Eq. 9 can be written as follows (Zhang, 2010):

$$\frac{M_t}{M_\infty} \approx \frac{6\sqrt{Dt}}{x\sqrt{\pi}} - \frac{3Dt}{x^2} \tag{10}$$

Where M_t is the amount of Ar which diffused out of the bead at time t; M_∞ is the amount of Ar which would have diffused out of the bead at an infinite time (*i.e.* total amount of Ar); x is the diffusing distance (radius of the sphere); D is the diffusion coefficient; t is time.

To define the mean Ar concentration in the beads at different times, we calculated the average value between core and rim concentrations at each time. The value used for M_∞ is 99.5 ppb, which is the average Ar concentration at day 0 (samples IC09-00.1C; IC09-00.1R; IC09-00.2C; IC09-00.2R). The definition of M_t is done by subtracting the initial average Ar concentration by the average concentration at time t (for example, M_4 in the MF is 99.5 – 38.3 = 61.2).

Samples were nearly spherical and with approximate diameters of 4 mm. For this reason, the value of x (sphere radius) used in the calculations is 2 mm.

To calculate D, data were plotted in M_t/M_∞ *vs.* t scatter graphs. After, a curve fitting function based on Eq. 10 was used to see which values of D would best represent the obtained data (Figure 41).

Using this method, we found D values of (3.43 ± 0.73) x 10^{-13} and (4.06 ± 0.63) x 10^{-13} m²/s for the experiments done on the MF and VTF, respectively. The 0.92 and 0.96 coefficients of determination (R^2) show that the curves represent the data accurately. The D/x^2 parameter is shown to facilitate comparison with other data in literature, with values of (8.57 ± 1.83) x 10^{-8} s^{-1} and (10.15 ± 1.58) x 10^{-8} s^{-1} for the MF and VTF, respectively.
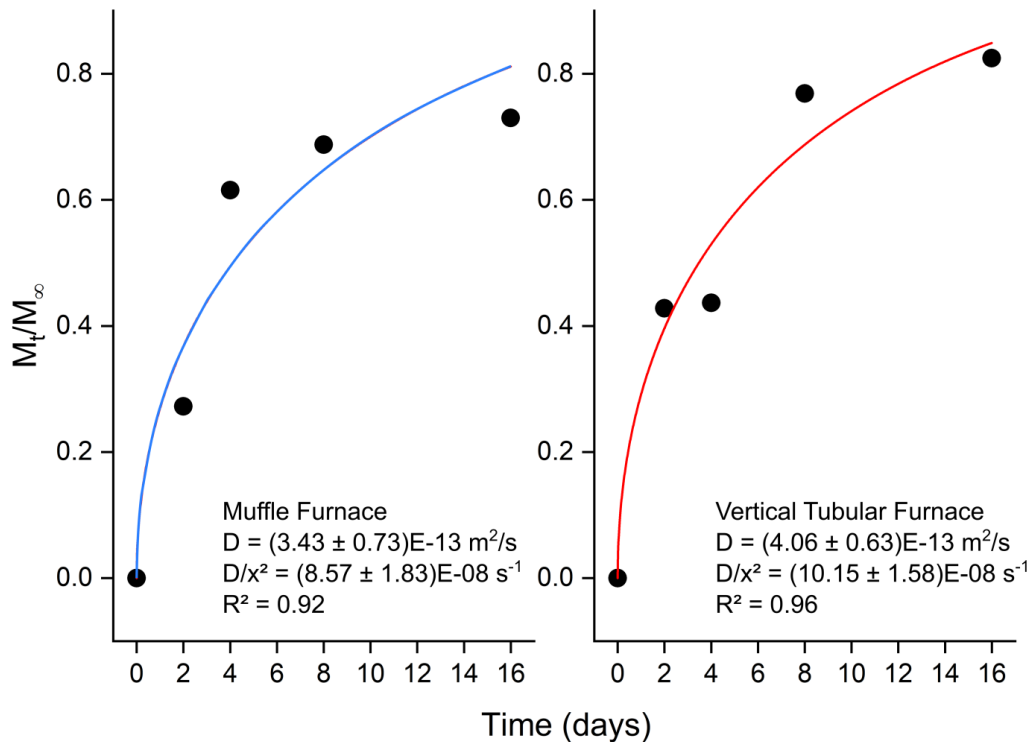
Figure 41 – Diffusion data from experiments done using the MF (left) and VTF (right). The best-fitting curves define the diffusion coefficient D. The y axis represents the fractional loss of Ar (see text for details). D/x^2 parameter is shown to facilitate comparisons with other data. The R^2 refers to the determination coefficient.

IV.4.2 Half-space diffusion problem with constant initial and surface concentrations

Here, the diffusion coefficients were calculated using the solution known as the half-space diffusion problem with constant initial and surface concentrations, which can be used for desorption experiments (Zhang, 2010), defined as:

$$C = C_s + (C_i - C_s)erf\frac{x}{\sqrt{4Dt}}$$ (11)

where C is the final concentration of the diffusant; C_s is the surface concentration, C_i is the initial concentration, x is the distance; D is the diffusion coefficient; and t is time.

The C_s for the experiments done in the VTF is zero since the furnace had a 100% CO_2-controlled atmosphere. For the MF, the value of C_s would be different because the atmosphere has around 1% of Ar. According to Zhang (2010), if the volatile concentration on the surface of the medium is zero or a low equilibrium value, C_s can be considered null. Figure 38 shows that Ar concentration changed similarly on the MF and VTF beads throughout the experiments, suggesting that the atmospheric Ar did not affect the experiments, so that C_s can be considered zero. Thus, the solution becomes Eq. 12:

$$C = C_i erf\frac{x}{\sqrt{4Dt}}$$ (12)

Here, C is the Ar concentration on the beads (experimental data from section IV.2); C_i is the average of values obtained at day 0 for core or rim analyses (samples IC09-00.1C, IC09-00.2C, IC09-00.1R, and IC09-00.2R; 59 ppb, 89 ppb, 128 ppb, and 121 ppb, respectively); x is the diffusing distance, t is the specified time (0, 2, 4, 8, or 16 days expressed in seconds).

The value of x is hard to determine accurately because (1) we cannot assure that the analysed material was collected exactly from the core of the beads, and (2) the diffusing distance is not necessarily the sphere radius. For this reason, two values of x were used: a maximum value of 2 mm (sphere radius), and a minimum value of 0.1mm (estimated distance of the material collected on the rim of the bead to the atmosphere)

To find the value of D, data were plotted in concentration *vs.* time scatter graphs. After, curve fittings based on Eq. 12 were made to see which values of D would best represent the

obtained data (Figure 42). Since there were two different initial concentration values for rim or core analyses, the average values were considered for t = 0. The two diffusive distances (x) were also considered. For the maximum x (2 mm), D values obtained were $(1.54 \pm 0.60) \times 10^{-11}$ m²/s; $(3.12 \pm 3.01) \times 10^{-11}$ m²/s; $(1.58 \pm 0.67) \times 10^{-11}$ m²/s, and $(2.98 \pm 2.1) \times 10^{-11}$ m²/s, for the MF core, MF rim, VTF core, and VTF rim, respectively. For the minimum x (0.1 mm), the values of D obtained were $(3.85 \pm 1.39) \times 10^{-14}$ m²/s; $(7.1 \pm 7.36) \times 10^{-14}$ m²/s; $(4.15 \pm 1.3) \times 10^{-14}$ m²/s, and $(7.46 \pm 5.16) \times 10^{-14}$ m²/s for the MF core, MF rim, VTF core and VTF rim, respectively. The determination coefficients show that the calculated values of D represent Eq. 12 reasonably well, with values of 0.57; 0.92; 0.96, and 0.98 for the MF core, MF rim, VTF core, and VTF rim respectively. Due to the uncertainties of x, the D/x^2 parameter is important for these data, with values of $(3.85 \pm 1.45) \times 10^{-6}$ s^{-1}; $(7.45 \pm 5.21) \times 10^{-6}$ s^{-1}; $(3.95 \pm 1.49) \times 10^{-6}$ s^{-1}, and $(7.81 \pm 7.44) \times 10^{-6}$ s^{-1}, for the MF core, MF rim, VTF core, and VTF rim, respectively.
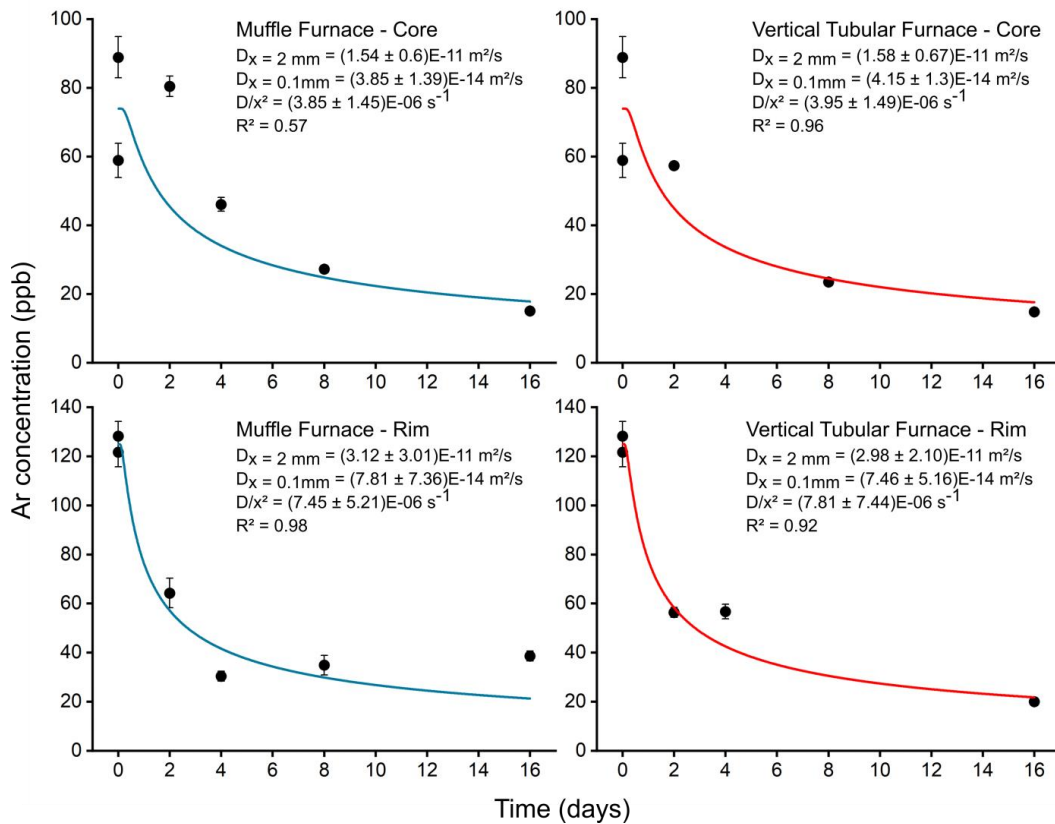
Figure 42 – Diffusion data obtained from experiments and the best fitting curves (Eq. 12) used to define the diffusion coefficients (*D*). Data from samples IC09-VTF-04C and IC09-VTF-08R are not shown because they extrapolate the y axis and were considered outliers. The determination coefficient (R²) was calculated considering the average composition at t = 0 (75 ppb for the cores, 125 ppb for the rims) based on samples IC09-00.1C and IC09-00.2C for

the cores,and IC09-00.1R and IC09-00.2R for the rims. $D_{x = 2mm}$ and $D_{x = 0.1mm}$ refer to diffusion coefficients calculated using the maximum and minimum values of x estimated in the models (see text for details), respectively. D/x^2 parameter is shown to facilitate comparisons with other data.

CHAPTER V – DISCUSSION

This section presents a discussion involving the results obtained from the experiments and their implications to the geodynamics of Venus.

V.1 Evaluating the Experiments

In this work, we created an experimental design to determine the bulk diffusivity of Ar in microgabbros under Venusian surface conditions. The experimental products and apparatuses are discussed in this section.

V.1.1 Experimental products

By the end of all experiments, a total of twelve different aliquots were generated (11 microgabbro beads, 1 glass bead). Unexpected features were observed in the experimental products through the EMP analyses, including the presence of crystal in the glass bead, the microgabbro texture, and the presence of vesicles in the samples, which are discussed ahead.

The Ti-magnetite crystals in the glass bead (sample IC09-GL) evidenced by the BSE images (Figure 35) can be attributed to two hypotheses: (1) the *liquidus* temperature estimated (1143ºC) was lower than the true *liquidus* of the system, so the 1200ºC temperature used was not high enough to completely melt the solution; or (2) the drop-quench mechanism was not fast enough to inhibit crystal formation in the system. These subhedral to euhedral crystals had high nucleation and presented small sizes (average ~10 μm) indicating that they were formed in a rapid cooling process. Furthermore, no absorption features were observed, which would be expected if they were only partially melted. These facts indicate that hypothesis (2) is more plausible. Carvalho (2016) ran glass-generating experiments using the same starting material. In that study, the author used a melting temperature of 1300ºC in a muffle furnace, followed by an additional melting at 1300ºC to homogenize the sample. Even so, Ti-magnetite crystals were present in some portions of the glass very similar to the ones found in our study. The author explained that these crystals were neoformed when the sample was transported from the furnace to the recipient containing deionized water. Here, we used the drop-quench mechanism which 'freezes' the experimental product much faster (< 1 s), but, apparently, not fast enough to generate a crystal-free glass. A possible explanation is that the opening of the VTF valve to execute the drop-quench would cause sufficient cooling to form the oxide crystals so that the

69

sample would be exposed to a temperature lower than 1200ºC for a few seconds before being drop-quenched. WDS point analyses show that IC09-GL has lower TiO_2 and FeO^T content in comparison to the XRF analyses done by Carvalho (2016) in a crystal-free glass (2.96 *vs.*4 and 10.09 *vs.* 14.2, respectively; see Tables 3 and 4). This is explained by the presence of the Ti-magnetite crystals on IC09-GL that fractionates these elements from the melt.

BSE images of the microgabbro fragment analyzed (sample IC09-MG; Figure 35) reveal a different texture from that obtained by Carvalho (2016) in a similar experiment using the same starting material (IC09). The author used a cooling rate of 1 ºC/h (vs. 2.5 ºC/h here) and a controlled atmospheric composition of CO and CO_2 to obtain oxygen fugacities close to the QFM (vs. 100% Ar controlled atmosphere here). Also, Carvalho (2016) used the electroplating technique to saturate the platinum wires with Fe and avoid the migration of Fe from the samples to the wires during the experiments. Even though the clinopyroxene and Ti-magnetite crystals show similar textures in both works, here, the plagioclase crystals are anhedral and impossible to individualize, while those from Carvalho (2016) are subhedral to euhedral. Furthermore, WDS analyses made here (Table 4) show that most plagioclase crystals are closely mixed with other phases. We do not have a clear explanation for these differences, but they could be related to the differences in oxygen fugacity and/or cooling rate between our experiments and those from Carvalho (2016).

The presence of vesicles (or microbubbles) in the experimental products speaks directly to the solubility of Ar. There are a few parameters that influence noble gas solubility in melts, glasses, and crystals, such as the system's density, molar volume, temperature, pressure, and ionic porosity (e.g. Fortier and Giletti, 1989; Carroll and Stolper, 1993; Paonita, 2009; Baxter, 2010; Iacono-Marziano et al., 2010). Due to their chemical inertness, atoms of rare gases dissolve in 'free spaces' of the silicate melt structure, following a physical mechanism of dissolution (Doremus, 1966; Studt et al., 1970; Shelby, 1976). In agreement with this principle, Carroll and Stolper (1993) show that ionic porosity (IP) is the main parameter influencing Ar solubility in silicate melts and glasses, which is widely accepted. IP can be defined as the difference between the unit cell volume of a mineral and the calculated volume of the anions and cations in the system (see Eq.6 on section III.2.7), i.e. IP is the free space in the melt or glass structure (Carroll and Stolper, 1993). Iacono-Marziano et al. (2010) show that temperature and pressure conditions are intrinsically connected to the IP, and that, together, these are the main controllers of noble gas

solubiity. The authors show that the solubility of most tholeiitic melts increases with temperature and IP, and decreases with pressure.

According to the literature, the solubility of Ar in tholeiitic melts at 1 bar is in the range of 2.5 x 10^{-5} to 9 x 10^{-5} cm³ (SPT)g^{-1} (i.e. 41 to 160 wt ppb; Fisher, 1970; Hayatsu and Waboso, 1985; Jambon et al., 1986). Our results show Ar concentrations of ~8 ppb, ~10,000 ppb, and ~130 ppb for the starting material (IC09), the glass bead (IC09-GL), and the microgabbro bead (IC09-MG), respectively (Figure 36). These values indicate that we were successful in increasing the Ar content in the melt (represented by the glass bead) and that the temperature drop combined with crystallization reduced Ar concentration in the system (represented by the microgabbro bead). The presence of bubbles in both the glass and microgabbro beads evidences the excess of Ar in the system, indicating that we were able to saturate the melt with Ar.

The step-heating graphs (Figure 37) show separate spikes of Ar detection for the glass, in contrast to the smoother Ar loss profile for the microgabbro. This can be attributed to the presence of Ar-filled microbubbles in the glass chips analyzed. Considering a density of 2.7 g/cm³ for the tholeiitic glass (e.g. Clark et al., 2016), the diameter of the glass chips analyzed (weighted at ~ 0.2 mg) would be around 260 μm. Bubbles from 1 to 45 μm (diameter) can be seen on BSE images on the glass (Figure 35), indicating that they could be present in the analyzed glass chips and that this explanation for the Ar excess is plausible.

Figure 34 shows that macroscopic vesicles are present in the microgabbro bead (1000 to 5000 μm in diameter), but very few microscopic bubbles were detected by the BSE images (Figure 35). Ar analyses on the microgabbro did not detect bubbles because they were either larger than the microgabbro chips analyzed or inexistent, except for the results from samples IC09-VTF-04C and IC09-VTF-08R which were considered outliers (probably Ar-bubble related).

Rapid bubble nucleation can occur when sudden changes in volatile saturation take place on the magma (Prousevitch et al., 1993; L'Heureux, 2007), which happened when the melt was exposed to large amounts of Ar in the experiment. The glass and microgabbro beads remained in the furnace for 5.5 and 140 hours, respectively. We interpret that the longer dwell time for the microgabbro allowed the system to get closer to equilibrium, while diffusion-induced bubble growth generated larger bubbles in comparison to the glass. Additionally, a temperature decrease makes samples' IP decrease, meaning that Ar solubility should be reduced due to the lack of 'free space' in the solution (Carroll and Stolper, 1993; Iacono-Marziano et al., 2010). These

mechanisms explain the lower Ar concentration in the microgabbro in comparison to the glass bead, because the Ar occupying the crystallizing melt diffused either into the atmosphere or into the bubbles.

The presence of these bubbles in the glass/microgabbro beads should not interfere in the determination of diffusion coefficients because conceptually they should be Ar-filled. If so, Ar atoms would still diffuse outwards to the atmosphere because the atmosphere is an infinite reservoir with a lower chemical potential than the bubbles. This is evidenced by the identical Ar_{rim}/Ar_{core} ratios for the microgabbro and glass beads, which indicates that Ar diffusion was homogenous across the samples (i.e diffusion inside the sample and diffusion into the atmosphere) despite the differences in bubble size and distribution, and crystal growth between the samples.

All this considered, we believe the experimental set-up responded well to its purpose and that we were able to replicate the necessary conditions to determine the bulk diffusivity of Ar in a Venusian-like rock.

V.1.2 Experimental apparatuses: MF *vs.* VTF

Two different furnace apparatuses were used in this research. The VTF was used at the start of the experiments to dope the microgabbro (or glass) beads with Ar (sections IV.1.2 and IV.1.3). After, both the VTF and MF were used simultaneously during the expositions of the beads to Venusian average surface temperature (460 ºC; described in section IV.1.3), with the VTF representing a 100% CO_2 atmosphere and the MF a terrestrial atmospheric composition. The idea of using both furnaces had the main objective of comparing the effects of atmospheric composition on the diffusivity of Ar.

Figure 38 shows that the results obtained from both furnaces are similar, except for the analyses of samples IC09-VTF-04C and IC09-VTF-08R. The spikes of Ar concentration can be attributed to the presence of microbubbles (as discussed above) or other unidentified analytical problems. It is unlikely that the CO_2 atmosphere had any interaction with the Ar inside the sample due to the noble gas' inertness. It is also unlikely that bubble growth occurred during this step of the experiments because there was no increment of Ar in the system to enhance bubble growth. Also, Figures 39 and 40 show that the heating steps had similar behavior for the MF and VTF samples. For these reasons, we believe that these outliers on VTF samples are the results of

microbubbles produced when the microgabbro beads were generated (process described in section IV.1.3), having no link with the 100% CO_2 atmosphere.

The diffusion data obtained from Ar concentrations also allow us to compare the results obtained from experiments held on both furnaces. Figure 43 shows that the log D obtained for the samples exposed to MF and VTF had very similar values. This is a reflex of the similar Ar concentrations obtained from the experiments held on both furnaces.

Thus, we believe that conducting the experiments on the VTF or MF made no difference in the results obtained. This is important for future research because the MF is easier to operate, even though the VTF has better temperature control (~10 ℃ *vs.* ~1 ℃ errors for the MF and VTF, respectively).
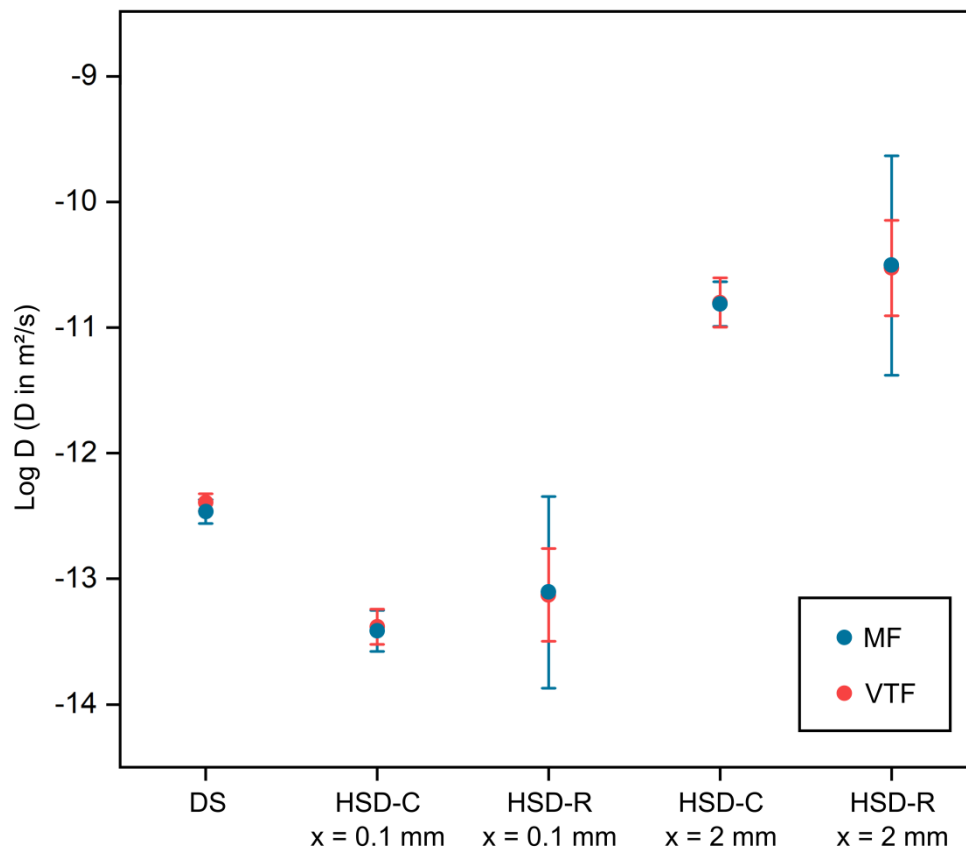
Figure 43 – Comparison between the log D obtained from experiments held on the MF (blue) and VTF (red). Notice that values are very similar. DS refers to the 'diffusion from a homogeneous sphere' solution (presented in section V.4.1) and HSD refers to the 'half-space diffusion' solution (presented in section V.4.2).

V.2 Diffusion Coefficients

In this research, ten different diffusion coefficients were obtained for the experiments (summarized in Table 6). These values can be divided into two large groups: those obtained through the 'diffusion from a homogeneous sphere' (DHS) solution (described in section V.4.1; Eq.10) and those obtained through the 'half-space diffusion problem' (HSD) solution (section V.4.2; Eq. 11). It is hard to identify which of the two methods is more accurate by comparing our results with the literature because this is the first time the bulk diffusivity of Ar in microgabbros is addressed. Thus, it is necessary to discuss the principles involved in each of these solutions to the diffusion problem.

Table 6 – Diffusion coefficients (D) obtained in this work. Log D and D/x^2 are also shown (x is the diffusing distance). DHS refers to the solutions from section V.4.1 (diffusion from a homogeneous sphere into an infinite reservoir), while HSD refers to the half-space diffusion problem (section IV.4.2). The letters a, b, c, d, e, f, g, h, i, j are used to facilitate correlations in text.

	D (m²/s)	Log D	D/x^2 (s^{-1})
[a] DHS-MF	$(3.43 \pm 0.73) \times 10^{-13}$	-12.46 ± 0.09	$(8.58 \pm 1.83) \times 10^{-8}$
[b] DHS-VTF	$(4.06 \pm 0.63) \times 10^{-13}$	-12.39 ± 0.07	$(1.02 \pm 0.16) \times 10^{-7}$
[c] HSD-MF-C, $x = 0.1$ mm	$(3.85 \pm 1.39) \times 10^{-14}$	-13.41 ± 0.16	$(3.85 \pm 1.45) \times 10^{-6}$
[d] HSD-MF-R, $x = 0.1$ mm	$(7.81 \pm 7.36) \times 10^{-14}$	-13.11 ± 0.76	$(7.81 \pm 5.21) \times 10^{-6}$
[e] HSD-VTF-C, $x = 0.1$ mm	$(4.15 \pm 1.30) \times 10^{-14}$	-13.38 ± 0.14	$(4.15 \pm 1.49) \times 10^{-6}$
[f] HSD-VTF-R, $x = 0.1$ mm	$(7.46 \pm 5.16) \times 10^{-14}$	-13.13 ± 0.37	$(7.46 \pm 7.44) \times 10^{-6}$
[g] HSD-MF-C, $x = 2$ mm	$(1.54 \pm 0.6) \times 10^{-11}$	-10.81 ± 0.18	$(3.85 \pm 1.45) \times 10^{-6}$
[h] HSD-MF-R, $x = 2$ mm	$(3.12 \pm 3.01) \times 10^{-11}$	-10.51 ± 0.87	$(7.81 \pm 5.21) \times 10^{-6}$
[i] HSD-VTF-C, $x = 2$ mm	$(1.58 \pm 0.67) \times 10^{-11}$	-10.80 ± 0.20	$(4.15 \pm 1.49) \times 10^{-6}$
[j] HSD-VTF-R, $x = 2$ mm	$(2.98 \pm 2.1) \times 10^{-11}$	-10.53 ± 0.38	$(7.46 \pm 7.44) \times 10^{-6}$

V.2.1 Comparison between solutions for the diffusion problem

The DHS solution (Eq. 10 described in section V.4.1) has been used by different authors (e.g. Foland, 1974; Harrison et al., 2009; Zhang, 2010) and it correlates the degassing occurring in a perfect sphere containing a homogeneously distributed volatile content with diffusion. As evidenced by Figures 32 and 34, even though our beads are slightly oval/drop-shaped, they are

very close to perfect spheres, so we believe they fit this solution reasonably well. When it comes to the volatile homogeneity across the bead, Figure 38 shows that from the second day of experiments onward, aliquots submitted to the MF and VTF exhibit very similar Ar concentrations on the rims and cores of the beads, indicating a homogeneous distribution. For these reasons, the DHS solution should describe the experiments accurately, which is confirmed by the determination coefficients (R^2) calculated for the models (0.92 and 0.96 for the MF and VTF, respectively).

Another solution for the diffusion equation used in this work is the half-space diffusion problem (HSD; reported in section V.4.2). This solution is widely used in works involving diffusion in one dimension (e.g. Nowak et al., 2004; Thomas et al., 2008; Spickenbom et al., 2010; Amalberti et al., 2018). In these experiments, authors usually increase the volatile concentration on one side of a sample that was previously absent of the gas. After, diffusion profiles can be achieved by analyzing the volatile concentration across the sample after a certain time (t) using Eq. 11. The medium is called semi-infinite when the diffusant does not cross the entire sample length. In our case, the beads had Ar distributed across the whole sample, so it was not possible to make diffusion profiles along with a semi-infinite medium. Even so, this solution is applicable because the desorption of Ar means that atoms diffused from the beads' cores to the rims and finally to the atmosphere, as shown by Zhang (2010). In this case, the diffusing distance (x) would be the sphere radius (2 mm in our case). However, this value is questionable because it is impossible to assure that the Ar atomss in the bead's core diffused through the entire sample radius. Ar atoms in the core may have diffused through a minimal distance (for example, $x = 0.1$mm), and the observed changes in Ar concentration can be resulted from these small diffusive lengths. Another situation, where $x = 2$ mm, would be inappropriate if the Ar concentration at the rims of the beads is used for calculating the diffusion coefficient. In this case, x would be much smaller than 2 mm because atoms diffused from the edges of the beads to the atmosphere. For this reason, diffusion coefficients were also calculated considering a diffusing distance of 0.1 mm (a minimal distance). This gave us a wide range of diffusion coefficients (8 different values), ranging from log D = -13.77 to -9.64 m²/s (considering minimum and maximum error values). For this reason the D/x^2 data obtained here is more reliable for this solution.

With all this considered, it becomes clear that the DHS solution provides more simple and reliable data because the experiments fit the solution's conditions better, making it possible

to determine all parameters more accurately. Hence, we believe that the diffusion coefficients that best represents the bulk diffusivity of Ar in the analyzed conditions are those represented by solutions DHS-MF and DHS-VTF, with values of (3.43 ± 0.73) x 10^{-13} m²/s and (4.06 ± 0.63) x 10^{-13} m²/s, respectively. As discussed earlier, results from the VTF and MF were very similar. Thus, the most accurate value of D is the average between these two values: (3.75 ± 0.68) x 10^{-13} m²/s, with log $D = -12.43 \pm 0.08$, and $D/x^2 = (9.4 \pm 1.7)$ x 10^{-8} s^{-1}.

V.2.2 Comparison between our data and the available literature data

There are two main challenges when comparing our results with the literature: (1) many authors report their diffusion data based on the Arrhenius Equation (Eq.4), using the D_0 (pre-exponential factor) and Ea (activation energy) as parameters, and (2) there is no data concerning the bulk diffusivity of Ar in tholeiitic rocks.

This first challenge is caused by the fact that in this work we could not obtain the values of Ea and D_0 because our experiments were done solely at the temperature of 460 ºC. One way of calculating these parameters would be to repeat the same experiments using different temperatures, making it possible to obtain the value of D_0 by calculating the angle formed by the slope of the line of points in a D vs. 1/T graph (Zhang, 2010). With the value of D_0, it would be possible to calculate Ea using the Arrhenius equation, allowing us to compare our data with the literature more easily. However, it is not impossible to find authors who report their diffusion data based on D, log D, D/x^2, or log D/x^2, and these works will be used for comparison here.

As of challenge (2), the solution we found is to make comparisons with diffusion data concerning Ar in silicic glasses. Due to our incapacity of calculating D_0 and Ea, the number of works available for comparison is reduced.

As illustrated by Figure 44 (absolute values on Table 7), the diffusion coefficients obtained in this work are orders of magnitude greater than those obtained by Reynolds (1957) and Nakayama and Shackelford (1990) who calculated the diffusion of Ar in similar temperatures (308 - 470 ºC and 500 - 675 ºC, respectively) in a potash-lime-silica-alumina glass and a SiO_2 glass, respectively. Our most reliable values of D (DHS solution) are comparable with those obtained by Perkins and Begeal (1971) and Amalberti et al. (2016) at higher temperatures (700 - 900 ºC) in CMAS and SiO_2 glasses, respectively (see description of Table 7 for glass compositions).
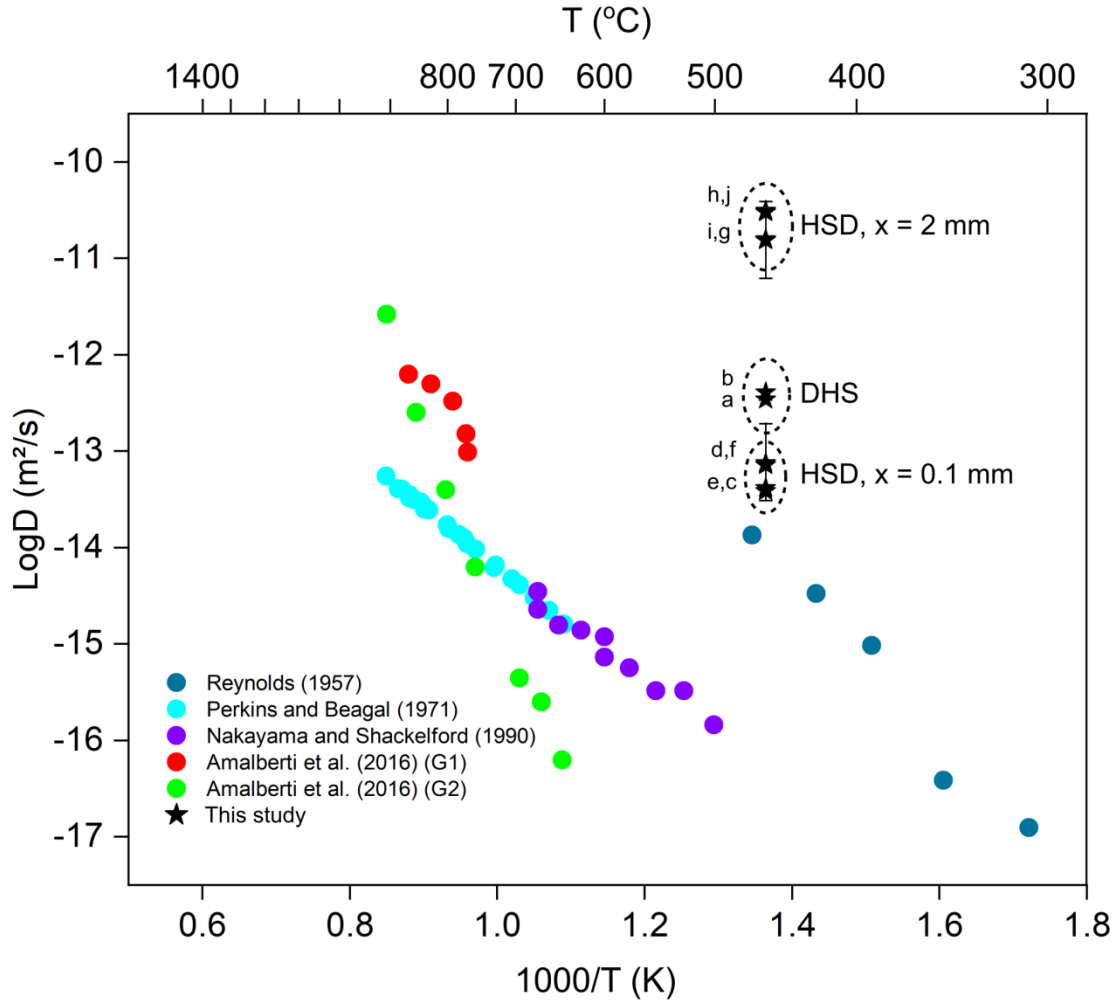
Figure 44 – Log *D* values obtained by different authors at 0.1 MPa. DHS (Eq. 10) and HSD (Eq. 11) refer to the two different solutions for the diffusion equation used in this work ('diffusion from a homogeneous sphere into an infinite reservoir' and 'half-space diffusion problem', respectively). Letters a, b, c, d, e, f, g, h, i, j refer to the values of log *D* based on the different solutions used in this work (see Table 6 for reference). Data from Reynolds (1957) refers to potash-lime-silica-alumina glass (53% SiO_2, 7% Al_2O_3, 36% K_2O, 4% CaO wt%); Perkins and Begal (1971) and Nakayama and Shackelford (1990) refers to SiO_2 glasses; Amalberti et al. (2016) G1 and G2 refer to two CMAS glasses (50% SiO_2, 15% Al_2O_3, 11% MgO, 23% CaO wt% and 60% SiO_2, 25% Al_2O_3, 5% MgO, 10% CaO wt%, respectively).

Table 7 – Compilation of Ar diffusion data in silicic glasses plotted in Figure 44. All experiments were done at atmospheric pressure (0.1 MPa). Data from Reynolds (1957) refers to potash-lime-silica-alumina glass (53% SiO_2, 7% Al_2O_3, 36% K_2O, 4% CaO wt%); Perkins and Begal (1971) and Nakayama and Shackelford (1990) refers to SiO_2 glasses; Amalberti et al. (2016) G1 and G2 refer to two CMAS glasses (50% SiO_2, 15% Al_2O_3, 11% MgO, 23% CaO wt% and 60% SiO_2, 25% Al_2O_3, 5% MgO, 10% CaO wt%, respectively).

Work	T (ºC)	T (1000/K)	D (m²/s)	Log D
Reynolds (1957)	308	1.72	1.25E-17	-16.90
Reynolds (1957)	350	1.61	3.85E-17	-16.41

Reynolds (1957)	390	1.51	9.71E-16	-15.01
Reynolds (1957)	425	1.43	3.34E-15	-14.48
Reynolds (1957)	470	1.35	1.35E-14	-13.87
Perkins and Beagal (1971)	644	1.09	1.62E-15	-14.79
Perkins and Beagal (1971)	662	1.07	2.25E-15	-14.65
Perkins and Beagal (1971)	679	1.05	3.02E-15	-14.52
Perkins and Beagal (1971)	698	1.03	4.1E-15	-14.39
Perkins and Beagal (1971)	707	1.02	4.74E-15	-14.32
Perkins and Beagal (1971)	729	1.00	6.6E-15	-14.18
Perkins and Beagal (1971)	731	1.00	6.21E-15	-14.21
Perkins and Beagal (1971)	757	0.97	9.6E-15	-14.02
Perkins and Beagal (1971)	770	0.96	1.1E-14	-13.96
Perkins and Beagal (1971)	774	0.96	1.26E-14	-13.90
Perkins and Beagal (1971)	782	0.95	1.37E-14	-13.86
Perkins and Beagal (1971)	798	0.93	1.58E-14	-13.80
Perkins and Beagal (1971)	800	0.93	1.73E-14	-13.76
Perkins and Beagal (1971)	830	0.91	2.45E-14	-13.61
Perkins and Beagal (1971)	837	0.90	2.52E-14	-13.60
Perkins and Beagal (1971)	837	0.90	2.68E-14	-13.57
Perkins and Beagal (1971)	843	0.90	2.98E-14	-13.53
Perkins and Beagal (1971)	854	0.89	3.15E-14	-13.50
Perkins and Beagal (1971)	862	0.88	3.26E-14	-13.49
Perkins and Beagal (1971)	862	0.88	3.52E-14	-13.45
Perkins and Beagal (1971)	875	0.87	4.02E-14	-13.40
Perkins and Beagal (1971)	882	0.87	4.1E-14	-13.39
Perkins and Beagal (1971)	905	0.85	5.55E-14	-13.26
Nakayama and Shackelford (1990)	500	1.29	1.45E-16	-15.84
Nakayama and Shackelford (1990)	525	1.25	3.27E-16	-15.49
Nakayama and Shackelford (1990)	550	1.22	3.29E-16	-15.48
Nakayama and Shackelford (1990)	575	1.18	5.65E-16	-15.25
Nakayama and Shackelford (1990)	600	1.15	1.19E-15	-14.92
Nakayama and Shackelford (1990)	600	1.15	7.34E-16	-15.13
Nakayama and Shackelford (1990)	625	1.11	1.39E-15	-14.86
Nakayama and Shackelford (1990)	650	1.08	1.58E-15	-14.80
Nakayama and Shackelford (1990)	675	1.05	2.28E-15	-14.64
Nakayama and Shackelford (1990)	675	1.05	3.52E-15	-14.45
Amalberti et al (2016) (G1)	769	0.96	9.77E-14	-13.01
Amalberti et al (2016) (G1)	771	0.96	1.51E-13	-12.82
Amalberti et al (2016) (G1)	791	0.94	3.31E-13	-12.48
Amalberti et al (2016) (G1)	826	0.91	5.01E-13	-12.30
Amalberti et al (2016) (G1)	863	0.88	6.31E-13	-12.20
Amalberti et al (2016) (G2)	646	1.09	6.31E-17	-16.20
Amalberti et al (2016) (G2)	670	1.06	2.51E-16	-15.60
Amalberti et al (2016) (G2)	698	1.03	4.47E-16	-15.35
Amalberti et al (2016) (G2)	758	0.97	6.31E-15	-14.20
Amalberti et al (2016) (G2)	802	0.93	3.98E-14	-13.40
Amalberti et al (2016) (G2)	851	0.89	2.51E-13	-12.60
Amalberti et al (2016) (G2)	903	0.85	2.63E-12	-11.58

These differences can be attributed to differences in materials' compositions (as explained in section II.3.2.5) or, mainly, to the types of diffusion measured here and on the other experiments. In a homogeneous, crystal-free glass, the diffusivity measured is a volume (or lattice) diffusion, because there are no interruptions on the periodic arrangement of atoms caused by crystals or other imperfections (Dohmen and Mike 2010; Zhang, 2010). This situation is different from this work because D was calculated in a polycrystalline heterogeneous system. In such systems, the grain boundaries (homophase interfaces) and interphase boundaries (boundaries between different phases) provide faster diffusion pathways which are not available in single crystals or glasses (Dohmen and Mike, 2010). Here, we calculated the bulk diffusivity (D_{bulk}) of Ar, which is the result of interface diffusion (or grain-boundary diffusion, D_{gb}) and lattice diffusion (D_l) occurring in the system (Eq. 5). In heterogeneous systems with small grain sizes (our case), D_{gb} prevails over D_l (Dohmen and Milke, 2010) as shown by Eq. 5. Thus, the D_{bulk} calculated here is strongly affected by the D_{gb}, which is typically orders of magnitude more efficient than D_l, resulting in D_{bulk} values larger than the D obtained by the other authors, which are more influenced by the D_l.

Namiki and Solomon (1998) argue that the ^{40}Ar produced from radioactive decay of ^{40}K in K-feldspars should be transported to grain boundaries within short geological periods at Venusian surface temperatures (~ 18 Ma, considering a grain size of 20 mm estimated from pictures from Venera 13 and Venera 14 missions; Surkov et al., 1984) so that the grain boundary diffusion (D_{gb}) should govern the diffusive transport. In agreement, Burnard et al. (2015) show that noble gases preferentially partition to grain boundaries because of the lower activation energy in those sites, indicating that D_{gb} should be the preponderant diffusive mechanism for noble gases in rocks.

Preliminary estimates of grain-boundary diffusion of Ar at 750 K (477 ºC) were obtained by Namiki and Solomon (1998). The authors multiplied the available volume diffusion coefficients (D_l) of Ar in glasses at that temperature range (Freer, 1981; Roselieb et al., 1992) by 10^5, provided that D_{gb} is usually several orders of magnitude more effective than volume diffusion. The authors obtained an estimated D_{gb} of 5 x 10^{-12} m²/s. This estimation is subjected to many uncertainties, however, it is fairly similar to the D_{bulk} we obtained for the average of DHS solutions: (3.75 ± 0.68) x 10^{-13} m²/s.

V.3 Characteristic Diffusion Distance and Limitations to our Models

Diffusion coefficients express the rate at which an area occupied by molecules expands (in our case, in m²/s). The distance travelled by these molecules in one dimension is called characteristic diffusion distance (L_D) and can be easily calculated using Eq. 12:

$$L_D = \sqrt{D.t} \tag{12}$$

Where L_D is the characteristic diffusion distance (m); D is the diffusion coefficient (m²/s), and t is time (s).

The L_D values obtained here (Table 8) are estimations of the distance Ar atoms would travel in microgabbros at 460 ℃ (Venusian surface) at the defined time periods in response to diffusion. The degassing of Ar happens when atoms in subsurface reach the atmosphere. Thus, the L_D values indicate the maximum depth at which Ar diffusive-driven degassing should occur in the crust of Venus. The limitations and implications of these estimates are discussed ahead.

The diffusive distances (and D_{bulk} values) were calculated considering a temperature of 460 ℃, which refers to the current average surface temperature of Venus. This is supposed to be the lowest (average) temperature in the planet's geosphere, so the D_{bulk} obtained here should reflect the (average) minimal diffusion coefficients in the Venusian crust. Even though the diffusion should be faster in subsurface because of the thermal gradient, the Ar atoms necessarily need to diffuse through the 460 ℃ crust to reach the atmosphere in a diffusion-governed degassing scenario. The largest L_D value we obtained is ~ 3,000 m (solution h), including error. Considering an average global thermal gradient of 10 ℃/km (e.g. O'Rourke et al., 2019), the temperature at that crustal depth should be around 490 ℃. This temperature is not significantly higher than the surface's 460 ℃, so the diffusion coefficient should not be very different. Thus, the D_{bulk} values should be similar throughout the crust in the estimated diffusive distances. However, the thermal gradients on Venusian crust are uncertain and vary both temporally and spatially. O'Rourke and Smrekar (2018) estimate a maximum regional gradient of 40 ℃/km under coronae, so that the temperature should be 580 ℃ at a 3,000 m depth. In this case, diffusion should be slightly faster but still relatable to our data.

Table 8 – Values of the characteristic diffusion distance (L_D) for each value of D_{bulk} obtained in this research calculated using Eq. 12. The most reliable data are those represented by the *a* and *b* solutions. Values after the bar indicate the L_D if the grain-size differences between our aliquots and Venusian rocks are considered (uncertainties not shown because these are rough estimations; see text for details).

Solution	$D\,(m^2/s)$	$L_D(\,0.5\ Ga)\,(m)$	$L_D(4.6\ Ga)\,(m)$
[a] DHS-MF	(3.43 ± 0.73) x 10^{-13}	74^{+7}_{-8} / 5	223^{+23}_{-25} / 16
[b] DHS-VTF	(4.06 ± 0.63) x 10^{-13}	80^{+6}_{-6} / 6	243^{+18}_{-20} / 17
[c] HSD-MF-C, x = 0.1 mm	(3.85 ± 1.39) x 10^{-14}	25^{+4}_{-5} / 2	75^{+12}_{-15} / 5
[d] HSD-MF-R, x = 0.1 mm	(7.81 ± 7.36) x 10^{-14}	35^{+14}_{-27} / 2	106^{+42}_{-81} / 8
[e] HSD-VTF-C, x = 0.1 mm	(4.15 ± 1.30) x 10^{-14}	26^{+4}_{-4} / 2	78^{+11}_{-13} / 5
[f] HSD-VTF-R, x = 0.1 mm	(7.46 ± 5.16) x 10^{-14}	34^{+10}_{-15} / 2	104^{+31}_{-46} / 7
[g] HSD-MF-C, x = 2 mm	(1.54 ± 0.6) x 10^{-11}	493^{+88}_{-108} / 35	1495^{+267}_{-327} / 106
[h] HSD-MF-R, x = 2 mm	(3.12 ± 3.01) x 10^{-11}	702^{+282}_{-570} / 50	2128^{+855}_{-1729} / 150
[i] HSD-VTF-C, x = 2 mm	(1.58 ± 0.67) x 10^{-11}	499^{+97}_{-120} / 35	1514^{+293}_{-365} / 107
[j] HSD-VTF-R, x = 2 mm	(2.98 ± 2.1) x 10^{-11}	686^{+210}_{-313} / 48	2080^{+636}_{-950} / 147

Another important limitation to our models is that it is impossible to define the planet's average surface temperature through geologic time. There are evidences that Earth has been through countless changes in average surface temperature since Hadean, so it is reasonable to assume that Venus may also have had similar behavior. Thus, our results are estimations that consider constant surface temperatures over the *t* intervals used in our calculations. Two values of *t* were used to allow the discussion of different diffusion scenarios. When *t* = 4.6 Ga, we are referring to the diffusion distance over the planet's lifetime. The *t* = 0.5 Ga scenario is related to the diffusion that would have occurred since the last global resurfacing event (as discussed in section II.2), when the degassing of Ar should have been highly effective because magma was in direct contact with the atmosphere (e.g. Namiki and Solomon, 1998).

Our diffusion coefficients were calculated at atmospheric pressure (0.1 MPa) and the atmosphere of Venus exerts a pressure of 9 MPa on the planet's surface. Mikhail and Heap (2017) calculated three different pore pressure gradients for the crust of Venus considering three estimated pore fluid densities: 0.89 MPa/km, 4.4 MPa/km, and 8.9 MPa/km. Using these values, we can assume that the pore pressure at the depth of 3 km should be 2.7 to 26.7 MPa. The effects of pressure on diffusion are complex (see section II.3.2.2), however, Behrens and Zhang (2001) show that *D* decreased with increasing pressure on a rhyolite melt. By analyzing their data

(Figure 15), it becomes clear that the pressure difference from our experiments and the Venusian pressure (on the surface and at a 3 km depth) should not change D_{bulk} (or L_D) significantly.

The differences from our aliquots to Venusian tholeiites in terms of grain size should provide the main differences in our estimations. It is expected that Venusian rocks should have large crystals because the high surface temperature should inhibit intrusion cooling and favor crystal growth (Kaula, 1999). Panorama pictures taken by the Venera 13 and 14 missions (Surkov et al., 1984) indicate that the rocks on Venus should have an upper bound grain diameter of ~ 20 mm (Namiki and Solomon, 1998), while our aliquots had ~0.1 mm crystals (see section IV.1). As mentioned in section V.2.2, grain size is an important parameter for diffusion because $D_{gb} >> D_l$, and systems with smaller grains are more influenced by the D_{gb}. It is possible to calculate the differences in D_{bulk} caused by the disparate grain-sizes (d) using Eq. 5 ($D_{bulk} = D_l + \left(\frac{3\delta}{d}\right).D_{if}$). If we consider that $D_{gb} = 10^5 . D_l$ as an approximation (e.g. Namiki and Solomon, 1998) and that $d = 2 . 10^{-3}$ m and $1 . 10^{-4}$ m for Venusian rocks and our experiments, respectively, we find that the D_{bulk} in the experiments should be 2000 times larger than the D_{bulk} on Venus. If these rough estimations are considered, the L_d values are reduced drastically, ranging from 2 to 50 m; and 5 to 150 m, if $t = 0.5$ and 4.6 Ga respectively (see table 8).

V.4 Implications to Venusian Geodynamics

Our most reliable data (solutions a and b) indicate that over 4.6 Ga, diffusive processes could degass Ar from a maximum depth of ~ 240 m in the crust of Venus, while solution h provides an upper bound of ~ 3,000 m. Considering a crustal thickness of 30 km (e.g. O'Rourke and Korenaga, 2015), these values indicate that the effective degassing of Ar should have occurred in 0.8 - 10% of the Venusian crust. If we consider the differences in grain size, these percentages fall to 0.01% - 0.16%. As discussed on section V.2.1, results from solution h are questionable, and thus, our most accurate results (solutions a and b) imply that > 99% of the Venusian crust would be undegassed in Ar if diffusion was the only process mobilizing Ar from the crust into the atmosphere.

These data suggest that diffusion is highly ineffective in transporting Ar from the interior of Venus to its atmosphere, as suggested by Mikhail and Heap (2017). These workers propose volcanism as the main liberating agent for transporting [40]Ar to the Venusian atmosphere, and thus, the lower atmospheric [40]Ar/[36]Ar ratio in the planet (Figure 1) should reflect a lower rate of

volcanism on Venus in comparison to Earth. This idea is supported by the differences in quantity of individual volcanoes on both planets. Earth's oceanic crust has created > 100,000 individual volcanoes (i.e. seamounts) in < 100 Ma (e.g. Wessel, 2001 and references therein), while only 70,000 individual volcanoes were created in < 700 Ma on Venus (Head and Wilson, 1992). Mikhail and Heap (2017) argue that the high surface temperatures on Venus affect the rheology of crustal rocks, making the crust mostly ductile. This would inhibit the formation of volcanoes because magma ascends more easily through fractures, which happen in the colder and shallower brittle crust. In a predominantly ductile crust, ascending mantle-derived melts should pond and spread laterally, underplating the crust until it reaches the brittle-ductile transition zone (BDT) through buoyancy-driven diapirism, when the magma can infiltrate fractures and ascend to the surface forming volcanoes (Mikhail and Heap, 2017).

Despite the indication of lower rate of volcanism on Venus, almost the entire surface of the planet is covered by volcanic plains (e.g. Ivanov and Head, 2011, 2013). Global catastrophic resurfacing events (see section II.2) could explain these voluminous bodies of extrusive rocks. These events should be important sources of ^{40}Ar to the atmosphere because the gas that was dissolved in the magma would be put in direct contact with the atmosphere. If Ar diffusion in the crust is slow and the rate of volcanism in between resurfacing events is low, then the feeding of ^{40}Ar to the atmosphere should occur as punctual degassing spikes during global resurfacing events (e.g. Namiki and Solomon, 1998). If this is true, then the crust of Venus should contain an excess of ^{40}Ar due to the ineffectiveness of diffusion in degassing Ar, and the ^{40}Ar/^{36}Ar atmospheric ratio on Venus should increase and become more similar to Earth's in the next global resurfacing event.

CHAPTER VI – CONCLUSIONS

In this work, we created an experimental design to determine the bulk diffusivity of Ar in microgabbros under Venusian surface conditions. Ar-saturated microgabbro and glass beads were generated using a Gero furnace (VTF). After, two different furnace apparatuses (MF, muffle furnace, and VTF) were used to expose the aliquots to Venusian surface temperatures so that we could compare the effects of atmospheric composition on the bulk diffusivity of Ar. The VTF represented a 100% CO_2 (0% Ar) atmosphere and the MF a terrestrial atmosphere (~ 1% Ar). We were able to calculate bulk diffusion coefficients (D_{bulk}) by tracking the changes in Ar concentration in the microgabbro beads through time (2, 4, 8, and 16 days) using the step-heating technique in an Argus multicollector mass spectrometer. Our data show that experiments held in both furnaces had similar results, evidencing that the differences in atmospheric composition did not affect the diffusion of Ar. This information is valuable for future experiments because the MF is easier to operate.

Two different solutions for the diffusion equation were used to calculate the bulk diffusivity of Ar. Our most reliable calculations show D_{bulk} values of ~ 3.5 x 10^{-13} m²/s for Ar in the analyzed conditions. This is the first time the D_{bulk} of Ar in a microgabbro was reported and our calculations show larger values than diffusion coefficients obtained for Ar in silicate glasses at similar temperatures. This is most likely related to the fact that our D_{bulk} values are highly influenced by the grain boundary diffusion (D_{gb}, i.e. diffusion occurring along the grain broundaries), which is known to be orders of magnitude faster than the lattice diffusion (D_l, i.e. volume diffusion occurring within a crystal or glass) calculated for the glass materials in the literature. This is a consequence of the micrometric crystals in the microgabbros, which provide fast diffusion pathways for Ar along grain boundaries.

It is widely accepted that diffusion and volcanism are the main liberating agents for transporting gases from the crust and/or mantle of rocky planets to their atmospheres. However, the D_{bulk} values calculated here show that diffusion is a very innefective mechanism for transporting Ar in the crust of Venus. The most reliable characteristic diffusion distances (L_D) we obtained imply that > 99% of the Venusian crust should be undegassed in Ar if diffusion was the only mechanism mobilizing the gas over the planet's 4.6 Ga. Thus, this work corroborates with the idea proposed by Mikhail and Heap (2017), in which volcanism should be the main

transporter of Ar from the interior of Venus to its atmosphere. This implicates that the lower $^{40}Ar/^{36}Ar$ ratios for Venus in comparison to Earth (1 vs. ~ 300, respectively) is a consequence of lower volcanic activity on Venus throughout its geological history, because ^{40}Ar is produced from de radioactive decay of ^{40}K in the interior of planets. Furthermore, we suggest that the degassing of ^{40}Ar on Venus should be tightly linked to global resurfacing events on the planet (e.g. Namiki and Solomon, 1998), when large volumes of magma (and ^{40}Ar) are put in direct contact with the atmosphere. This means that the $^{40}Ar/^{36}Ar$ ratios on the atmospheres of Earth and Venus should become more similar when such events occur because the accumulated ^{40}Ar in Venusian crust should be (at least partially) degassed, while the higher volcanic activity on Earth should degas ^{40}Ar continuously.

Finally, we believe that we have created a simple experimental design to determine the bulk diffusion coefficients of volatiles in rocks. Running these experiments at different temperatures would allow the calculation of the pre-exponential factor (D_0) and the activation energy (E_a), which would enable fitting the data in Arrhenius plots and compare our results with the literature more easily.

REFERENCES

Aitta, A., 2012, Venus' internal structure, temperature and core composition: Icarus, v. 218, p. 967–974, doi:10.1016/j.icarus.2012.01.007.

Amalberti, J., Burnard, P., Laporte, D., Tissandier, L., and Neuville, D.R., 2016, Multidiffusion mechanisms for noble gases (He, Ne, Ar) in silicate glasses and melts in the transition temperature domain: Implications for glass polymerization: Geochimica et Cosmochimica Acta, v. 172, p. 107–126, doi:10.1016/j.gca.2015.09.027.

Amalberti, J., Burnard, P., Tissandier, L., and Laporte, D., 2018, The diffusion coefficients of noble gases (He Ar) in a synthetic basaltic liquid: One-dimensional diffusion experiments: Chemical Geology, v. 480, p. 35–43, doi:10.1016/j.chemgeo.2017.05.017.

Amirkhanov, K.H.I., Bartnitzkii, E.N., Brandt, S.B., Voitkevich, G.V., 1959. The migration of argon and helium in certain rocks and minerals. Geochemistry Series Dokl. Acad. Sci. USSR 126.

Anderson, F.S., and Smrekar, S.E., 2006, Global mapping of crustal and lithospheric thickness on Venus: Journal of Geophysical Research E: Planets, v. 111, p. 1–20, doi:10.1029/2004JE002395.

Ballentine, C.J., and Barry, P.H., 2017, Noble Gases, *in* White W. (eds), Encyclopedia of Geochemistry. Encyclopedia of Earth Sciences Sries, Springer, Cham. p. 1–6, doi:10.1007/978-3-319-39193-9_195-1.

Basilevsky, A.T., and Head, J.W., 2003, The surface of Venus: Reports on Progress in Physics, v. 66, p. 1699–1734, doi:10.1088/0034-4885/66/10/R04.

Baxter, E.F., 2010, Diffusion of noble gases in minerals: Reviews in Mineralogy and Geochemistry, v. 72, p. 509–557, doi:10.2138/rmg.2010.72.11.

Becker, M.W., and Shapiro, A.M., 2000, Tracer transport in fractured crystalline rock: Evidence of nondiffusive breakthrough tailing: Water Resources Research, v. 36, p. 1677–1686, doi:10.1029/2000WR900080.

Behrens, H., 2009, Water Diffusion in Silicate Glasses and Melts: Advances in Science and Technology, v. 46, p. 79–88, doi:10.4028/www.scientific.net/ast.46.79.

Behrens, H., 2010, Noble Gas Diffusion in Silicate Glasses and Melts: Reviews in Mineralogy and Geochemistry, v. 72, p. 227–267, doi:10.2138/rmg.2010.72.6.

Behrens, H., and Zhang, Y., 2001, Ar diffusion in hydrous silicic melts: Implications for volatile diffusion mechanisms and fractionation: Earth and Planetary Science Letters, v. 192, p. 363–376, doi:10.1016/S0012-821X(01)00458-7.

Bercovici, D., and Ricard, Y., 2014, Plate tectonics, damage and inheritance: Nature, v. 508, p. 513–516, doi:10.1038/nature13072.

Bougher, S.W., Hunten, D.M., Philips, R.J., 1997, Venus II – Geology, Geophysics, Atmosphere, and Solar Wind Environment: Tucson, University of Arizona Press, 1362 p.

Boving, T.B., and Grathwohl, P., 2001, Tracer diffusion coefficients in sedimentary rocks: correlation to porosity and hydraulic conductivity: Journal of Contaminant Hydrology, v. 53, p. 85–100, doi:10.1016/S0169-7722(01)00138-3.

Brady, J.B., and Cherniak, D.J., 2010, Diffusion in minerals: An overview of published experimental diffusion data: Reviews in Mineralogy and Geochemistry, v. 72, p. 899–920, doi:10.2138/rmg.2010.72.20.

Brooker, R.A., Du, Z., Blundy, J.D., Kelley, S.P., Allan, N.L., Wood, B.J., Chamorro, E.M., Wartho, J.A., and Purton, J.A., 2003, The "zero charge" partitioning behaviour of noble gases during mantle melting: Nature, v. 423, p. 738–741, doi:10.1038/nature01708.

Burnard, P.G., Demouchy, S., Delon, R., Arnaud, N.O., Marrocchi, Y., Cordier, P., and Addad, A., 2015, The role of grain boundaries in the storage and transport of noble gases in the mantle: Earth and Planetary Science Letters, v. 430, p. 260–270, doi:10.1016/j.epsl.2015.08.024.

Carroll, M.R., 1991, Diffusion of Ar in rhyolite, orthoclase and albite composition glasses: Earth and Planetary Science Letters, v. 103, p. 156–168, doi:10.1016/0012-821X(91)90157-D.

Carroll, M.R., and Stolper, E.M., 1993, Noble gas solubilities in silicate melts and glasses: New experimental results for argon and the relationship between solubility and ionic porosity: Geochimica et Cosmochimica Acta, v. 57, p. 5039–5051, doi:10.1016/0016-7037(93)90606-W.

Carvalho, P. R., 2016, *Experimentos de cristalização de fusões toleíticas básicointermediárias naturais sob pressão atmosférica e implicações geológicas*. Thesis (Monography). São Paulo: Instituto de Geociências USP.

Carvalho, P.R., 2020, Implications from liquid immiscibility experiments for the evolution of tholeiitic systems: Dissertation (MSc.). São Paulo: Instituto de Geociências, USP.

Cassata, W.S., Renne, P.R., and Shuster, D.L., 2009, Argon diffusion in plagioclase and implications for thermochronometry: A case study from the Bushveld Complex, South Africa: Geochimica et Cosmochimica Acta, v. 73, p. 6600–6612, doi:10.1016/j.gca.2009.07.017.

Cassata, W.S., Renne, P.R., and Shuster, D.L., 2011, Argon diffusion in pyroxenes: Implications for thermochronometry and mantle degassing: Earth and Planetary Science Letters, v. 304, p. 407–416, doi:10.1016/j.epsl.2011.02.019.

Cassata, W.S., Shuster, D.L., Renne, P.R., and Weiss, B.P., 2010, Evidence for shock heating and constraints on Martian surface temperatures revealed by 40Ar/39Ar thermochronometry of Martian meteorites: Geochimica et Cosmochimica Acta, v. 74, p. 6900–6920, doi:10.1016/j.gca.2010.08.027.

Chassefière, E., Wieler, R., Marty, B., and Leblanc, F., 2012, The evolution of Venus: Present state of knowledge and future exploration: Planetary and Space Science, v. 63–64, p. 15–23, doi:10.1016/j.pss.2011.04.007.

Clark, A.N., Lesher, C.E., Jacobsen, S.D., and Wang, Y., 2016, Anomalous density and elastic properties of basalt at high pressure: Reevaluating of the effect of melt fraction on seismic velocity in the Earth's crust and upper mantle: Journal of Geophysical Research: Solid Earth, v. 121, p. 4232–4248, doi:10.1002/2016JB012973.

Corrigan, G., and Gibb, F.G.F., 1979, The loss of Fe and Na from a basaltic melt during experiments using the wire-loop method: Mineralogical Magazine, v. 43, p. 121–126, doi:10.1180/minmag.1979.043.325.10.

Crank, J., 1975, The Mathematics of Diffusion: Bristol, Oxford University Press, 1–421 p.

Cussler, E.L., 1997, Diffusion: Mass Transfer in Fluid Systems: Cambridge, Cambridge University Press, 580p.

Davaille, A., Smrekar, S.E., and Tomlinson, S., 2017, Experimental and observational evidence for plume-induced subduction on Venus: Nature Geoscience, v. 10, p. 349–355, doi:10.1038/ngeo2928.

Dohmen, R., and Milke, R., 2010, Diffusion in polycrystalline materials: Grain boundaries, mathematical models, and experimental data: Reviews in Mineralogy and Geochemistry, v. 72, p. 921–970, doi:10.2138/rmg.2010.72.21.

Donahue, T.M., Russell, C.T., 1997. The Venus atmosphere and ionosphere and their interaction with the solar wind: an overview. In: Bougher, S.W., Hunten, D.M., Phillips, R.J. (Eds.), Venus II – Geology, Geophysics, Atmosphere, and Solar Wind Environment: Tucson, University of Arizona Press, p. 3 – 31.

Donahue, T., 1999, New Analysis of Hydrogen and Deuterium Escape from Venus: Icarus, v. 141, p. 226–235, doi:10.1006/icar.1999.6186.

Doremus, R.H., 1966, Physical Solubility of Gases in Fused Silica: Journal of the American Ceramic Society, v. 49, p. 461–462, doi:10.1111/j.1151-2916.1966.tb13299.x.

Driscoll, P., and Bercovici, D., 2014, On the thermal and magnetic histories of Earth and Venus: Influences of melting, radioactivity, and conductivity: Physics of the Earth and Planetary Interiors, v. 236, p. 36–51, doi:10.1016/j.pepi.2014.08.004.

Dumoulin, C., Tobie, G., Verhoeven, O., Rosenblatt, P., and Rambaux, N., 2017, Tidal constraints on the interior of Venus: Journal of Geophysical Research: Planets, v. 122, p. 1338–1352, doi:10.1002/2016JE005249.

Ernesto, M., Raposo, M.I.., Marques, L.., Renne, P.., Diogo, L.., and de Min, A., 1999, Paleomagnetism, geochemistry and dating of the North-eastern Paraná Magmatic Province: tectonic implications: Journal of Geodynamics, v. 28, p. 321–340, doi:10.1016/S0264-3707(99)00013-7.

Farver, J.R., and Yund, R.A., 2000, Silicon diffusion in forsterite aggregates: Implications for diffusion accommodated creep: Geophysical Research Letters, v. 27, p. 2337–2340, doi:10.1029/2000GL008492.

Faure, G., 1986, Principles of Isotope Geology (second edition): New York, John Wiley and Sons, 608 p.

Fick, A., 1855, Ueber Diffusion: Annalen der Physik und Chemie, v. 170, p. 59–86, doi:10.1002/andp.18551700105.

Fisher, D.E., 1970, Heavy rare gases in a Pacific seamount: Earth and Planetary Science Letters, v. 9, p. 331–335, doi:10.1016/0012-821X(70)90130-5.

Foland, K.A., 1974, Ar40 diffusion in homogenous orthoclase and an interpretation of Ar diffusion in K-feldspars: Geochimica et Cosmochimica Acta, v. 38, p. 151–166, doi:10.1016/0016-7037(74)90200-2.

Foland, K.A., and Xu, Y., 1990, Diffusion of 40Ar and 39Ar in irradiated orthoclase: Geochimica et Cosmochimica Acta, v. 54, p. 3147–3158, doi:10.1016/0016-7037(90)90130-D.

Fortier, S.M., and Giletti, B.J., 1989, An Empirical Model for Predicting Diffusion Coefficients in Silicate Minerals: Science, v. 245, p. 1481–1484, doi:10.1126/science.245.4925.1481.

Fourier, J.B., 1822, *Théorie Analytique de la Chaleur*: Paris, Firmin Didot Père et Fils, 408 p.

Ghail, R., 2015, Rheological and petrological implications for a stagnant lid regime on Venus: Planetary and Space Science, v. 113–114, p. 2–9, doi:10.1016/j.pss.2015.02.005.

Gilmore, M., Treiman, A., Helbert, J., and Smrekar, S., 2017, Venus Surface Composition Constrained by Observation and Experiment: Space Science Reviews, v. 212, p. 1511–1540, doi:10.1007/s11214-017-0370-8.

Guo, C., and Zhang, Y., 2018, Multicomponent diffusion in basaltic melts at 1350 °C: Geochimica et Cosmochimica Acta, v. 228, p. 190–204, doi:10.1016/j.gca.2018.02.043.

Guo, C., and Zhang, Y., 2016, Multicomponent diffusion in silicate melts: SiO2–TiO2–Al2O3–MgO–CaO–Na2O–K2O System: Geochimica et Cosmochimica Acta, v. 195, p. 126–141, doi:10.1016/j.gca.2016.09.003.

Harrison, T.M., Célérier, J., Aikman, A.B., Hermann, J., and Heizler, M.T., 2009, Diffusion of 40Ar in muscovite: Geochimica et Cosmochimica Acta, v. 73, p. 1039–1051, doi:10.1016/j.gca.2008.09.038.

Harrison, T.M., Duncan, I., and McDougall, I., 1985, Diffusion of 40Ar in biotite: Temperature, pressure and compositional effects: Geochimica et Cosmochimica Acta, v. 49, p. 2461–2468, doi:10.1016/0016-7037(85)90246-7.

Hayatsu, A., and Waboso, C.E., 1985, The solubility of rare gases in silicate melts and implications for K☐Ar dating: Chemical Geology: Isotope Geoscience section, v. 52, p. 97–102, doi:10.1016/0168-9622(85)90009-0.

Hazelton, G.B., Axen, G., and Lovera, O., 2003, Argon retention properties of silicate glasses and implications for 40Ar/39Ar age and noble gas diffusion studies: Contributions to Mineralogy and Petrology, v. 145, p. 1–14, doi:10.1007/s00410-003-0440-7.

Head, J.W., and Wilson, L., 1992, Magma reservoirs and neutral buoyancy zones on Venus: Implications for the formation and evolution of volcanic landforms: Journal of Geophysical Research, v. 97, p. 3877, doi:10.1029/92JE00053.

Hess, P.C., and Head, J.W., 1990, Derivation of primary magmas and melting of crustal materials on Venus: Some preliminary petrogenetic considerations: Earth, Moon and Planets, v. 50–51, p. 57–80, doi:10.1007/BF00142389.

Hoffman, J.H., Hodges, R.R., Donahue, T.M., and McElroy, M.B., 1980, Composition of the Venus lower atmosphere from the Pioneer Venus Mass Spectrometer: Journal of Geophysical Research, v. 85, p. 7882, doi:10.1029/ja085ia13p07882.

Iacono-Marziano, G., Paonita, A., Rizzo, A., Scaillet, B., and Gaillard, F., 2010, Noble gas solubilities in silicate melts: New experimental results and a comprehensive model of the effects of liquid composition, temperature and pressure: Chemical Geology, v. 279, p. 145–157, doi:10.1016/j.chemgeo.2010.10.017.

Istomin, V.G., Grechnev, K. V., and Kotchnev, V.A., 1980, Mass spectrometer measurements of the composition of the lower atmosphere of venus: COSPAR Colloquia Series, v. 20, p. 215–218, doi:10.1016/S0964-2749(13)60044-X.

Ivanov, M.A., and Head, J.W., 2011, Global geological map of Venus: Planetary and Space Science, v. 59, p. 1559–1600, doi:10.1016/j.pss.2011.07.008.

Ivanov, M.A., and Head, J.W., 2013, The history of volcanism on Venus: Planetary and Space Science, v. 84, p. 66–92, doi:10.1016/j.pss.2013.04.018.

Jakosky, B.M., Slipski, M., Benna, M., Mahaffy, P., Elrod, M., Yelle, R., Stone, S., and Alsaeed, N., 2017, Mars' atmospheric history derived from upper-atmosphere measurements of ^{38}Ar/^{36}Ar: Science, v. 355, p. 1408–1410, doi:10.1126/science.aai7721.

Jambon, A., 1982, Tracer diffusion in granitic melts: Experimental results for NA, K, RB, CS, CA, SR, BA, CE, EU to 1300°C and a model of calculation: Journal of Geophysical Research: Solid Earth, v. 87, p. 10797–10810, doi:10.1029/JB087iB13p10797.

Jambon, A., Weber, H., and Braun, O., 1986, Solubility of He, Ne, Ar, Kr and Xe in a basalt melt in the range 1250-1600°C. Geochemical implications: Geochimica et Cosmochimica Acta, v. 50, p. 401–408, doi:10.1016/0016-7037(86)90193-6.

James, P.B., Zuber, M.T., and Phillips, R.J., 2013, Crustal thickness and support of topography on Venus: Journal of Geophysical Research E: Planets, v. 118, p. 859–875, doi:10.1029/2012JE004237.

Janasi, V. de A., de Freitas, V.A., and Heaman, L.H., 2011, The onset of flood basalt volcanism, Northern Paraná Basin, Brazil: A precise U–Pb baddeleyite/zircon age for a Chapecó-type dacite: Earth and Planetary Science Letters, v. 302, p. 147–153, doi:10.1016/j.epsl.2010.12.005.

Jellinek, A.M., Lenardic, A., and Manga, M., 2002, The influence of interior mantle temperature on the structure of plumes: Heads for Venus, Tails for the Earth: Geophysical Research Letters, v. 29, p. 2–5, doi:10.1029/2001gl014624.

Jiménez-Díaz, A., Ruiz, J., Kirby, J.F., Romeo, I., Tejero, R., and Capote, R., 2015, Lithospheric structure of Venus from gravity and topography: Icarus, v. 260, p. 215–231, doi:10.1016/j.icarus.2015.07.020.

Johnson, C.L., and Richards, M.A., 2003, A conceptual model for the relationship between coronae and large-scale mantle dynamics on Venus: Journal of Geophysical Research, v. 108, doi:10.1029/2002je001962.

Kasting, J.F., 1988, Runaway and moist greenhouse atmospheres and the evolution of Earth and Venus: Icarus, v. 74,

p. 472–494, doi:10.1016/0019-1035(88)90116-9.

Kaula, W.M., 1999, Constraints on Venus Evolution from Radiogenic Argon: Icarus, v. 139, p. 32–39, doi:10.1006/icar.1999.6082.

Kelley, S.P., and Wartho, J.-A., 2000, Rapid Kimberlite Ascent and the Significance of Ar-Ar Ages in Xenolith Phlogopites: Science, v. 289, p. 609–611, doi:10.1126/science.289.5479.609.

Koepke, J., and Behrens, H., 2001, Trace element diffusion in andesitic melts: An application of synchrotron X-ray fluoresence analysis: Geochimica et Cosmochimica Acta, v. 65, p. 1481–1498, doi:10.1016/S0016-7037(01)00550-6.

Kunz, J., Falter, M., and Jessberger, E.K., 1997, Shocked meteorites: Argon-40-argon-39 evidence for multiple impacts: Meteoritics & Planetary Science, v. 32, p. 647–670, doi:10.1111/j.1945-5100.1997.tb01550.x.

L'Heureux, I., 2007, A new model of volatile bubble growth in a magmatic system: Isobaric case: Journal of Geophysical Research: Solid Earth, v. 112, p. 1–14, doi:10.1029/2006JB004872.

Landuyt, W., and Bercovici, D., 2009, Variations in planetary convection via the effect of climate on damage: Earth and Planetary Science Letters, v. 277, p. 29–37, doi:10.1016/j.epsl.2008.09.034.

Lécuyer, C., Simon, L., and Guyot, F., 2000, Comparison of carbon, nitrogen and water budgets on Venus and the Earth: Earth and Planetary Science Letters, v. 181, p. 33–40, doi:10.1016/S0012-821X(00)00195-3.

Lenardic, A., Foley, B., Moore, W.B., O'Neill, C., and Jellinek, A.M., 2016, Climate-tectonic coupling: Variations in the mean, variations about the mean, and variations in mode: Journal of Geophysical Research: Planets, v. 121, p. 1831–1864, doi:10.1002/2016je005089.

Lenardic, A., Jellinek, A.M., and Moresi, L.-N., 2008, A climate induced transition in the tectonic style of a terrestrial planet: Earth and Planetary Science Letters, v. 271, p. 34–42, doi:10.1016/j.epsl.2008.03.031.

Lino, L. M., 2015, *A intrusão toleítica de Limeira (SP): Contribuições à geologia, petrografia e alterações hidrotermais*: Thesis (Monography). São Paulo: Instituto de Geociências USP.

Lino, L.M., and Vlach, S.R.F., 2021, Textural and Geochemical Evidence for Multiple, Sheet-like Magma Pulses in the Limeira Intrusion, Paraná Magmatic Province, Brazil: Journal of Petrology, v. 62, doi:10.1093/petrology/egab011.

Lorenz, R.D., Turtle, E.P., Stiles, B., Le Gall, A., Hayes, A., Aharonson, O., Wood, C.A., Stofan, E., and Kirk, R., 2011, Hypsometry of Titan: Icarus, v. 211, p. 699–706, doi:10.1016/j.icarus.2010.10.002.

Le Losq, C., Neuville, D.R., Florian, P., Henderson, G.S., and Massiot, D., 2014, The role of Al^{3+} on rheology and structural changes in sodium silicate and aluminosilicate glasses and melts: Geochimica et Cosmochimica Acta, v. 126, p. 495–517, doi:10.1016/j.gca.2013.11.010.

Mallmann, G., Fonseca, R.O.C., and Silva, A.B., 2014, An experimental study of the partitioning of trace elements between rutile and silicate melt as a function of oxygen fugacity: Anais da Academia Brasileira de Ciencias, v. 86, p. 1609–1629, doi:10.1590/0001-3765201420140014.

Marrocchi, Y., and Toplis, M.J., 2005, Experimental determination of argon solubility in silicate melts: An assessment of the effects of liquid composition and temperature: Geochimica et Cosmochimica Acta, v. 69, p. 5765–5776, doi:10.1016/j.gca.2005.08.010.

Mather, T.A., 2008, Volcanism and the atmosphere: The potential role of the atmosphere in unlocking the reactivity of volcanic emissions: Philosophical Transactions of the Royal Society A: Mathematical, Physical and Engineering Sciences, v. 366, p. 4581–4595, doi:10.1098/rsta.2008.0152.

Mikhail, S., and Heap, M.J., 2017, Hot climate inhibits volcanism on Venus: Constraints from rock deformation experiments and argon isotope geochemistry: Physics of the Earth and Planetary Interiors, v. 268, p. 18–34, doi:10.1016/j.pepi.2017.05.007.

Mocquet, A., Rosenblatt, P., Dehant, V., and Verhoeven, O., 2011, The deep interior of Venus, Mars, and the Earth: A brief review and the need for planetary surface-based measurements: Planetary and Space Science, v. 59, p. 1048–1061, doi:10.1016/j.pss.2010.02.002.

Moldrup, P., Olesen, T., Blendstrup, H., Komatsu, T., de Jonge, L.W., and Rolston, D.E., 2007, Predictive-descriptive models for gas and solute diffusion coefficients in variably saturated porous media coupled to pore-size distribution: Soil Science, v. 172, p. 741–750, doi:10.1097/SS.0b013e3180d0a423.

Moresi, L. -N., and Solomatov, V.S., 1995, Numerical investigation of 2D convection with extremely large viscosity variations: Physics of Fluids, v. 7, p. 2154–2162, doi:10.1063/1.868465.

Mungall, J.E., Dingwell, D.B., and Chaussidon, M., 1999, Chemical diffusivities of 18 trace elements in granitoid melts: Geochimica et Cosmochimica Acta, v. 63, p. 2599–2610, doi:10.1016/S0016-7037(99)00209-4.

Nakayama, G.S., and Shackelford, J.F., 1990, Solubility and diffusivity of argon in vitreous silica: Journal of Non-Crystalline Solids, v. 126, p. 249–254, doi:10.1016/0022-3093(90)90826-8.

Namiki, N., and Solomon, S.C., 1998, Volcanic degassing of argon and helium and the history of crustal production on Venus: Journal of Geophysical Research E: Planets, v. 103, p. 3655–3677, doi:10.1029/97JE03032.

Nowak, M., Schreen, D., and Spickenbom, K., 2004, Argon and CO 2 on the race track in silicate melts: A tool for the development of a CO 2 speciation and diffusion model: Geochimica et Cosmochimica Acta, v. 68, p. 5127–5138, doi:10.1016/j.gca.2004.06.002.

O'Rourke, J.G., Buz, J., Fu, R.R., and Lillis, R.J., 2019, Detectability of Remanent Magnetism in the Crust of Venus: Geophysical Research Letters, v. 46, p. 5768–5777, doi:10.1029/2019GL082725.

O'Rourke, J.G., and Smrekar, S.E., 2018, Signatures of Lithospheric Flexure and Elevated Heat Flow in Stereo Topography at Coronae on Venus: Journal of Geophysical Research: Planets, v. 123, p. 369–389, doi:10.1002/2017JE005358.

Ozima, M., and Podosek, F.A., 2009, Chapter 7 Noble Gases in the Earth: 217–252 p., doi:10.1029/JB089iS02p0B393.

Paonita, 2009, Noble gas solubility in silicate melts:a review of experimentation and theory, and implications regarding magma degassing processes: Annals of Geophysics, v. 48, doi:10.4401/ag-3225.

Peng, S., Hu, Q., and Hamamoto, S., 2012, Diffusivity of rocks: Gas diffusion measurements and correlation to porosity and pore size distribution: Water Resources Research, v. 48, p. 1–9, doi:10.1029/2011WR011098.

Penrose, R.A.F., 1914, Certain phases of superficial diffusion in ore deposits: Economic Geology, v. 9, p. 20–24, doi:10.2113/gsecongeo.9.1.20.

Perkins, W.G., and Begeal, D.R., 1971, Diffusion and permeation of He, Ne, Ar, Kr, and D2 through silicon oxide thin films: The Journal of Chemical Physics, v. 54, p. 1683–1694, doi:10.1063/1.1675072.

Pollack, J.B., Toon, O.B., Whitten, R.C., Boese, R., Ragent, B., Tomasko, M., Esposito, L., Travis, L., and Wiedman, D., 1980, Distribution and source of the UV absorption in Venus' atmosphere: Journal of Geophysical Research, v. 85, p. 8141, doi:10.1029/JA085iA13p08141.

Popov, D. V., Spikings, R.A., and Kouzmanov, K., 2020, Pathways for 39Ar loss during step-heating of alkali feldspar megacrysts from the Shap granite (UK): Combined evidence from diffusion experiments and characterisation of heating-induced texture modifications: Chemical Geology, v. 547, doi:10.1016/j.chemgeo.2020.119677.

Prousevitch, A.A., Sahagian, D.L., and Anderson, A.T., 1993, Dynamics of diffusive bubble growth in magmas: isothermal case: Journal of Geophysical Research, v. 98, doi:10.1029/93jb02027.

Pujol, M., Marty, B., Burgess, R., Turner, G., and Philippot, P., 2013, Argon isotopic composition of Archaean atmosphere probes early Earth geodynamics: Nature, v. 498, p. 87–90, doi:10.1038/nature12152.

Reynolds, M.B., 1957, Diffusion of Argon in a Potassium-Lime-Silica Glass: Journal of the American Ceramic Society, v. 40, p. 395–398, doi:10.1111/j.1151-2916.1957.tb12560.x.

Romeo, I., and Turcotte, D.L., 2008, Pulsating continents on Venus: An explanation for crustal plateaus and tessera terrains: Earth and Planetary Science Letters, v. 276, p. 85–97, doi:10.1016/j.epsl.2008.09.009.

Rourke, J.G.O., and Korenaga, J., 2015, Thermal evolution of Venus with argon degassing: Icarus, v. 260, p. 128–140, doi:10.1016/j.icarus.2015.07.009.

Schaeffer, N., and Manga, M., 2001, Interaction of rising and sinking mantle plumes: Geophysical Research Letters, v. 28, p. 455–458, doi:10.1029/2000GL012215.

Schwartzman, D.W., and Giletti, B.J., 1977, Argon diffusion and absorption studies of pyroxenes from the Stillwater complex, Montana: Contributions to Mineralogy and Petrology, v. 60, p. 143–159, doi:10.1007/BF00372279.

Shearer, C.K., 2006, Thermal and Magmatic Evolution of the Moon: Reviews in Mineralogy and Geochemistry, v. 60, p. 365–518, doi:10.2138/rmg.2006.60.4.

Shelby, J.E., 1976, Pressure dependence of helium and neon solubility in vitreous silica: Journal of Applied Physics, v. 47, p. 135–139, doi:10.1063/1.322359.

Shellnutt, J.G., 2013, Petrological modeling of basaltic rocks from Venus: A case for the presence of silicic rocks: Journal of Geophysical Research: Planets, v. 118, p. 1350–1364, doi:10.1002/jgre.20094.

Smrekar, S.E., Davaille, A., and Sotin, C., 2018, Venus Interior Structure and Dynamics: Springer Nature B.V., v. 214, doi:10.1007/s11214-018-0518-1.

Smrekar, S.E., Helbert, J., Treiman, A., Drossart, P., Piccioni, G., Stofan, E.R., Elkins-Tanton, L., and Mueller, N., 2010, Recent Hotspot Volcanism on Venus from VIRTIS Emissivity Data: Science, v. 328, p. 605–608, doi:10.1126/science.1186785.

Smrekar, S.E., and Stofan, E.R., 1997, Corona Formation and Heat Loss on Venus by Coupled Upwelling and Delamination: Science, v. 277, p. 1289–1294, doi:10.1126/science.277.5330.1289.

Spickenbom, K., Sierralta, M., and Nowak, M., 2010, Carbon dioxide and argon diffusion in silicate melts: Insights

into the CO 2 speciation in magmas: Geochimica et Cosmochimica Acta, v. 74, p. 6541–6564, doi:10.1016/j.gca.2010.08.022.

Stevenson, D.J., 1983, Planetary magnetic fields: Reports on Progress in Physics, v. 46, p. 555–620, doi:10.1088/0034-4885/46/5/001.

Stevenson, D.J., 2003, Planetary magnetic fields: Earth and Planetary Science Letters, v. 208, p. 1–11, doi:10.1016/S0012-821X(02)01126-3.

Studt, P.L., Shackelford, J.F., and Fulrath, R.M., 1970, Solubility of Gases in Glass—A Monatomic Model: Journal of Applied Physics, v. 41, p. 2777–2780, doi:10.1063/1.1659314.

Surkov, Y.A., Barsukov, V.L., Moskalyeva, L.P., Kharyukova, V.P., and Kemurdzhian, A.L., 1984, New data on the composition, structure, and properties of Venus rock obtained by Venera 13 and Venera 14: Journal of Geophysical Research, v. 89, p. B393, doi:10.1029/JB089iS02p0B393.

Thomas, J.B., Cherniak, D.J., and Watson, E.B., 2008, Lattice diffusion and solubility of argon in forsterite, enstatite, quartz and corundum: Chemical Geology, v. 253, p. 1–22, doi:10.1016/j.chemgeo.2008.03.007.

Treiman, A.H., 2007, Geochemistry of venus' surface: Current limitations as future opportunities: Geophysical Monograph Series, v. 176, p. 7–16, doi:10.1029/176GM03.

Van Orstrand, C.E., 1915, Preliminary report on the diffusion of solids. U.S. Geol Survey Professional Paper 95-G:83-96, doi: 10.3133/pp95G.

Watson, E.B., Thomas, J.B., and Cherniak, D.J., 2007, 40Ar retention in the terrestrial planets: Nature, v. 449, p. 299–304, doi:10.1038/nature06144.

Weller, M.B., Lenardic, A., and O'Neill, C., 2015, The effects of internal heating and large scale climate variations on tectonic bi-stability in terrestrial planets: Earth and Planetary Science Letters, v. 420, p. 85–94, doi:10.1016/j.epsl.2015.03.021.

Wessel, P., 2001, Global distribution of seamounts inferred from gridded Geosat/ERS-1 altimetry: Journal of Geophysical Research: Solid Earth, v. 106, p. 19431–19441, doi:10.1029/2000JB000083.

Wilson, L., 2009, Volcanism in the solar system: Nature Geoscience, v. 2, p. 389–397, doi:10.1038/ngeo529.

Zahnle, K., Schaefer, L., and Fegley, B., 2010, Earth's Earliest Atmospheres: Cold Spring Harbor Perspectives in Biology, v. 2, p. a004895–a004895, doi:10.1101/cshperspect.a004895.

Zhang, Y., 2010, Diffusion in Minerals and Melts: Theoretical Background: Reviews in Mineralogy and Geochemistry, v. 72, p. 5–59, doi:10.2138/rmg.2010.72.2.

Zhang, F., Hayes, R.E., and Kolaczkowski, S.T., 2004, A New Technique to Measure the Effective Diffusivity in a Catalytic Monolith Washcoat: Chemical Engineering Research and Design, v. 82, p. 481–489, doi:10.1205/026387604323050191.

Zhang, Y., and Liu, L., 2012, On diffusion in heterogeneous media: American Journal of Science, v. 312, p. 1028–1047, doi:10.2475/09.2012.03.

Zhang, Y., Ni, H., and Chen, Y., 2010, Diffusion Data in Silicate Melts: Reviews in Mineralogy and Geochemistry, v. 72, p. 311–408, doi:10.2138/rmg.2010.72.8.

Zharkov, V.N., 1992, Venus Geology, Geochemistry and Geophysics. Research Results from the USSR ed V. Barsukov et al: Tucson, University of Arizona Press, 233 p.

Appendix A – Chemical analyses (WDS) of samples IC09-MG and IC09-GL. mg# = 100 x [MgO/(MgO+FeO^T)].

SAMPLE IC09-MG (microgabbro)

Pyroxene crystals

WDS compositions (wt%)

	CPX1	CPX2	CPX3	CPX4	CPX5	CPX6	CPX7	CPX8	Mean
SiO$_2$	46.97	47.00	46.72	47.22	46.10	45.14	46.52	45.54	46.40
TiO$_2$	1.94	2.31	2.15	2.05	2.12	2.33	2.08	2.06	2.13
Al$_2$O$_3$	4.72	5.65	5.59	4.89	5.32	5.88	6.19	5.74	5.50
Cr$_2$O$_3$	0.00	0.00	0.00	0.04	0.00	0.10	0.01	0.13	0.04
FeO^T	6.82	8.36	7.41	6.28	6.84	7.42	7.19	7.56	7.24
MnO	0.31	0.29	0.27	0.38	0.28	0.29	0.26	0.31	0.30
MgO	15.04	14.29	14.89	14.66	14.63	14.04	14.14	14.56	14.53
CaO	20.68	20.36	20.83	19.91	20.87	20.95	20.84	20.44	20.61
Na$_2$O	0.48	0.57	0.52	0.77	0.47	0.54	0.61	0.50	0.56
K$_2$O	0.08	0.01	0.03	0.14	0.03	0.04	0.00	0.01	0.04
Total	**97.04**	**98.84**	**98.40**	**96.34**	**96.66**	**96.72**	**97.85**	**96.85**	**97.34**
mg#	0.80	0.75	0.78	0.81	0.79	0.77	0.78	0.77	0.78

Structural formulae (based on 4 cations and 6 O, according to Droop, 1987)

	CPX1	CPX2	CPX3	CPX4	CPX5	CPX6	CPX7	CPX8	Mean
Si	1.780	1.759	1.748	1.799	1.756	1.723	1.752	1.733	1.76
Al	0.211	0.249	0.246	0.220	0.239	0.264	0.275	0.257	0.25
Sum T	**1.991**	**2.009**	**1.994**	**2.019**	**1.994**	**1.987**	**2.027**	**1.990**	2.00
Ti	0.055	0.065	0.060	0.059	0.061	0.067	0.059	0.059	0.06
Cr	0.000	0.000	0.000	0.001	0.000	0.003	0.000	0.004	0.00
Fe^{3+}	0.158	0.144	0.176	0.127	0.165	0.195	0.147	0.193	0.16
Fe	0.058	0.118	0.056	0.073	0.053	0.042	0.079	0.048	0.07
Mn	0.010	0.009	0.009	0.012	0.009	0.009	0.008	0.010	0.01
Mg	0.849	0.797	0.831	0.833	0.830	0.799	0.794	0.826	0.82
Ca	0.840	0.817	0.835	0.813	0.852	0.857	0.841	0.833	0.84
Na	0.035	0.041	0.038	0.057	0.035	0.040	0.044	0.037	0.04
K	0.004	0.000	0.001	0.007	0.001	0.002	0.000	0.001	0.00
Sum M	**2.009**	**1.991**	**2.006**	**1.981**	**2.006**	**2.013**	**1.973**	**2.010**	2.00

Molecular components

	CPX1	CPX2	CPX3	CPX4	CPX5	CPX6	CPX7	CPX8	Mean
Wo	43.84	43.32	43.81	43.75	44.61	45.05	44.98	43.64	44.13
En	44.36	42.30	43.58	44.82	43.50	42.00	42.46	43.25	43.28
Fs	11.80	14.37	12.61	11.43	11.89	12.94	12.55	13.12	12.59

			SAMPLE IC09-MG (microgabbro)			
			Plagioclase crystals			

WDS compositions (wt%)

	PL1	PL2	PL3	PL4	PL5	Mean
SiO$_2$	52.09	53.03	53.08	52.29	52.20	52.54
TiO$_2$	0.21	0.28	0.18	0.11	0.22	0.20
Al$_2$O$_3$	26.90	26.50	27.20	27.00	27.33	26.99
Fe$_2$O$_3$^{T}	3.02	2.85	3.06	3.07	3.18	3.04
MnO	0.00	0.03	0.01	0.00	0.00	0.01
MgO	0.36	0.46	0.40	0.38	0.27	0.37
CaO	11.47	11.12	11.56	11.79	11.82	11.55
Na$_2$O	4.26	4.56	4.14	3.98	3.98	4.18
K$_2$O	0.21	0.20	0.22	0.23	0.21	0.21
Total	**98.50**	**99.00**	**99.85**	**98.85**	**99.20**	**99.08**

Structural formulae (based on 32 O, according to Gualda and Vlach, 2005)

Si	9.660	9.768	9.700	9.664	9.617	9.68
Ti	0.029	0.039	0.025	0.015	0.030	0.03
Al	5.880	5.753	5.858	5.881	5.934	5.86
FeIII	0.421	0.395	0.421	0.427	0.441	0.42
Sum T	**15.991**	**15.955**	**16.003**	**15.987**	**16.022**	**15.99**
Mn	0.000	0.005	0.002	0.000	0.000	0.00
Mg	0.100	0.126	0.109	0.105	0.074	0.10
Ca	2.279	2.195	2.263	2.335	2.333	2.28
Na	1.532	1.629	1.467	1.426	1.422	1.50
K	0.050	0.047	0.051	0.054	0.049	0.05
Sum M	**3.960**	**4.002**	**3.892**	**3.920**	**3.878**	**3.93**

Molecular components

An	59	57	60	61	61	60
Ab	40	42	39	37	37	39
Or	1	1	1	1	1	1

	SAMPLE IC09-MG (microgabbro)						
	Ti-magnetite crystals						

WDS compositions (wt%)

	OP1-MG	OP2-MG	OP3-MG	OP4-MG	OP5-MG	OP6-MG	mean
SiO_2	0.15	0.12	0.15	0.13	0.29	0.32	0.19
TiO_2	14.79	15.79	15.29	16.52	16.28	15.54	15.70
Al_2O_3	1.08	1.32	1.40	1.11	1.02	1.24	1.20
Cr_2O_3	0.03	0.02	0.03	0.03	0.03	0.01	0.02
FeO^T	67.36	67.06	66.59	65.85	65.34	65.54	66.29
MnO	0.59	0.73	0.68	0.79	0.81	0.75	0.73
MgO	5.53	5.97	6.05	6.47	6.76	6.30	6.18
ZnO	0.02	0.08	0.08	0.09	0.09	0.08	0.07
NiO	0.02	0.00	0.02	0.02	0.02	0.02	0.02
CaO	0.37	0.22	0.21	0.27	0.18	0.35	0.27
Na_2O	0.00	0.04	0.00	0.00	0.03	0.03	0.02
Nb_2O_5	0.03	0.00	0.00	0.00	0.06	0.00	0.02
Total	**89.97**	**91.36**	**90.50**	**91.29**	**90.91**	**90.18**	**90.70**

Cation proportions (on the basis of 4 O, as in Carmichael, 1967)

	OP1-MG	OP2-MG	OP3-MG	OP4-MG	OP5-MG	OP6-MG	mean
Si	0.006	0.005	0.006	0.005	0.011	0.012	0.01
Ti	0.427	0.448	0.437	0.468	0.462	0.445	0.45
Al	0.049	0.059	0.063	0.049	0.045	0.056	0.05
Fe^{3+}	1.083	1.034	1.050	1.003	1.006	1.028	1.03
Fe^{2+}	1.081	1.082	1.067	1.071	1.056	1.058	1.07
Mn	0.019	0.023	0.022	0.025	0.026	0.024	0.02
Mg	0.317	0.336	0.343	0.363	0.380	0.358	0.35
Ca	0.015	0.009	0.009	0.011	0.007	0.014	0.01
Na	0.000	0.003	0.000	0.000	0.002	0.002	0.00
Cr	0.001	0.001	0.001	0.001	0.001	0.000	0.00
Zn	0.000	0.002	0.002	0.003	0.003	0.002	0.00
Ni	0.000	0.000	0.001	0.001	0.001	0.001	0.00
Nb	0.001	0.000	0.000	0.000	0.001	0.000	0.00
Total	**3.000**	**3.002**	**3.000**	**3.000**	**3.001**	**3.002**	**3.00**

Glass

WDS compositions (wt%).

	GL1	GL2	GL3	GL4	GL5	GL6	GL7	GL8	GL9	GL10	GL11	GL12	GL13	GL14	GL15	Mean
SiO_2	51.00	51.65	50.78	52.03	51.84	51.36	51.75	51.39	51.16	51.38	51.57	52.29	51.64	51.73	51.73	51.55
TiO_2	3.11	2.83	2.84	3.06	2.95	2.80	3.11	3.11	3.19	2.80	2.87	2.89	2.87	3.01	2.97	2.96
ZrO_2	0.05	0.14	0.11	0.17	0.06	0.13	0.13	0.13	0.12	0.09	0.08	0.11	0.16	0.04	0.09	0.11
Al_2O_3	13.57	13.61	13.49	13.52	13.49	13.36	13.50	13.70	13.71	13.71	13.65	13.66	13.70	13.59	13.82	13.61
FeO	10.05	10.28	10.50	10.34	10.28	10.11	10.12	10.01	9.63	9.92	10.19	10.22	9.85	9.77	10.13	10.09
MnO	0.19	0.22	0.25	0.23	0.14	0.23	0.23	0.19	0.23	0.15	0.26	0.22	0.25	0.24	0.24	0.22
MgO	4.76	4.88	4.59	4.52	4.65	4.77	4.66	4.59	4.65	4.58	4.84	4.65	4.63	4.57	4.70	4.67
CaO	8.70	8.71	8.40	8.55	8.52	8.71	8.62	8.37	8.30	8.53	8.69	8.73	8.67	8.45	8.38	8.56
Na_2O	3.04	2.95	3.12	2.92	3.33	2.93	2.97	3.30	3.06	2.89	3.23	2.74	3.17	2.92	3.08	3.04
K_2O	1.15	1.15	1.09	1.22	1.07	1.07	1.12	1.09	1.12	1.05	1.18	1.14	1.10	1.05	1.09	1.11
P_2O_5	0.63	0.59	0.62	0.54	0.60	0.64	0.66	0.62	0.63	0.56	0.58	0.65	0.57	0.66	0.53	0.60
Total	**96.23**	**97.01**	**95.78**	**97.09**	**96.94**	**96.10**	**96.87**	**96.49**	**95.80**	**95.64**	**97.14**	**97.30**	**96.62**	**96.03**	**96.78**	**96.52**
mg#	45.78	45.84	43.80	43.80	44.64	45.69	45.08	44.98	46.26	45.15	45.85	44.79	45.59	45.47	45.27	45.20

CIPW norm based on the mean values calculated as in Kelsey (1965) considering FeO = 0.8 x FeO^T

Quartz (Q)	6.09
Orthoclase (Or)	6.56
Albite (Ab)	25.72
Anorthite (An)	20.21
Diopside (Di)	15.03
Hypersthene (Hy)	12.78
Magnetite (Mt)	3.22
Ilmenite (Il)	5.62
Apatite (Ap)	1.39
Total	**96.63**

Ti-magnetite crystals

WDS compositions (wt%)

	OP1-GL	OP2-GL	OP3-GL	mean
SiO_2	0.20	0.21	0.27	0.23
TiO_2	4.18	15.02	15.02	11.41
Al_2O_3	4.32	1.79	1.82	2.64
Cr_2O_3	2.95	0.04	0.43	1.14
FeO^T	71.72	69.89	70.19	70.60
MnO	0.40	0.16	0.15	0.23
MgO	7.33	3.08	2.98	4.46
ZnO	0.06	0.01	0.03	0.03
NiO	0.06	0.02	0.01	0.03
CaO	0.21	0.27	0.23	0.24
Na_2O	0.03	0.03	0.02	0.03
Nb_2O_5	0.00	0.00	0.03	0.01
Total	**91.47**	**90.52**	**91.17**	**91.05**

Cationic proportions (on the basis of 4 O as in Carmichael, 1967)

	OP1-GL	OP2-GL	OP3-GL	mean
Si	0.007	0.008	0.010	0.009
Ti	0.115	0.439	0.437	0.330
Al	0.185	0.082	0.083	0.117
Fe^{3+}	1.484	1.021	1.009	1.171
Fe^{2+}	0.701	1.252	1.260	1.071
Mn	0.012	0.005	0.005	0.007
Mg	0.398	0.179	0.172	0.249
Ca	0.008	0.011	0.009	0.010
Na	0.002	0.002	0.001	0.002
Cr	0.085	0.001	0.013	0.033
Zn	0.002	0.000	0.001	0.001
Ni	0.002	0.001	0.000	0.001
Nb	0.000	0.000	0.001	0.000
Total	**3.002**	**3.001**	**3.001**	**3.001**